National Library of Canada
Bibliothèque nationale du Canada

Canadian Theses Service
Service des thèses canadiennes

Ottawa, Canada
K1A 0N4

NOTICE

The quality of this microform is heavily dependent upon the quality of the original thesis submitted for microfilming. Every effort has been made to ensure the highest quality of reproduction possible.

If pages are missing, contact the university which granted the degree.

Some pages may have indistinct print especially if the original pages were typed with a poor typewriter ribbon or if the university sent us an inferior photocopy.

Reproduction in full or in part of this microform is governed by the Canadian Copyright Act, R.S.C. 1970, c. C-30, and subsequent amendments.

AVIS

La qualité de cette microforme dépend grandement de la qualité de la thèse soumise au microfilmage. Nous avons tout fait pour assurer une qualité supérieure de reproduction.

S'il manque des pages, veuillez communiquer avec l'université qui a conféré le grade.

La qualité d'impression de certaines pages peut laisser à désirer, surtout si les pages originales ont été dactylographiées à l'aide d'un ruban usé ou si l'université nous a fait parvenir une photocopie de qualité inférieure.

La reproduction, même partielle, de cette microforme est soumise à la Loi canadienne sur le droit d'auteur, SRC 1970, c. C-30, et ses amendements subséquents.

NL-339 (r. 88/04) c

Canada

UNIVERSITY OF ALBERTA

The Thermal Conductivity of Fluid ^{4}He and the Ratio of Thermal Conductivities of Solid and Fluid ^{4}He at the Melting Point

BY

Edgar Hilmer Nelson

A thesis submitted to the Faculty of Graduate Studies and Research in partial fulfillment of the requirements for the degree of Doctor of Philosophy.

in

LOW TEMPERATURE PHYSICS

DEPARTMENT of PHYSICS

Edmonton, Alberta
Fall 1991

National Library of Canada
Bibliothèque nationale du Canada

Canadian Theses Service
Service des thèses canadiennes

Ottawa, Canada
K1A 0N4

The author has granted an irrevocable non-exclusive licence allowing the National Library of Canada to reproduce, loan, distribute or sell copies of his/her thesis by any means and in any form or format, making this thesis available to interested persons.

L'auteur a accordé une licence irrévocable et non exclusive permettant à la Bibliothèque nationale du Canada de reproduire, prêter, distribuer ou vendre des copies de sa thèse de quelque manière et sous quelque forme que ce soit pour mettre des exemplaires de cette thèse à la disposition des personnes intéressées.

The author retains ownership of the copyright in his/her thesis. Neither the thesis nor substantial extracts from it may be printed or otherwise reproduced without his/her permission.

L'auteur conserve la propriété du droit d'auteur qui protège sa thèse. Ni la thèse ni des extraits substantiels de celle-ci ne doivent être imprimés ou autrement reproduits sans son autorisation.

ISBN 0-315-70002-5

Canada

UNIVERSITY OF ALBERTA

RELEASE FORM

NAME OF AUTHOR: Edgar Hilmer Nelson

TITLE OF THESIS: The Thermal Conductivity of Fluid ^{4}He and the Ratio of Thermal Conductivities of Solid and Fluid ^{4}He at the Melting Point

DEGREE: Doctor of Philosophy

YEAR THIS THESIS GRANTED: 1991

Permission is hereby granted to the University of Alberta Library to reproduce single copies of this thesis and to lend or sell such copies for private, scholarly, or scientific research purposes only.

The author reserves all other publication and other rights in association with the copyright in the thesis, and except as hereinbefore provided neither the thesis nor any substantial portion thereof may be printed or otherwise reproduced in any material form whatever without the author's prior written permission.

38 Wyecliff
22560 Wye Road
Sherwood Park, Alberta, CANADA.
T8A 4T6

October 10, 1991

UNIVERSITY OF ALBERTA

FACULTY OF GRADUATE STUDIES AND RESEARCH

The undersigned certify that they have read, and recommend to the Faculty of Graduate Studies and Research for acceptance, a thesis entitled **The Thermal Conductivity of Fluid ^{4}He and the Ratio of Thermal Conductivities of Solid and Fluid ^{4}He at the Melting Point**, submitted by Edgar H. Nelson in partial fulfillment of the requirements for the degree of Doctor of Philosophy.

Dr. J. P. Franck

Dr. M. J. Crooks

Dr. J. Stephenson

Dr. S. S. Sheinin

Dr. J. S. Rogers

Dr. J. E. Bertie

October 2, 1991

DEDICATED TO MY MOTHER
AND
IN MEMORY OF MY FATHER

Abstract

The ratio of thermal conductivities of solid and fluid at equilibrium is of considerable importance in the study and theory of dendritic solidification. The present work was undertaken in order to provide this information for ^{4}He at elevated pressures. The method of 'guarded concentric cylinders' was chosen since the anticipated experimental conditions included pressures up to 2 kbar and temperatures between 8 K and 80 K. This apparatus was used to obtain the absolute value of the thermal conductivity coefficient for fluid ^{4}He in the range $\{8\ \mathrm{K} < T < 80\mathrm{K},\ 450\ \mathrm{bar} < P < 2050\ \mathrm{bar}\}$, and for solid and fluid ^{4}He in the immediate vicinity of the melting curve for temperatures between 8 K and 20 K. As such, this project constitutes the first report of thermal conductivity values for fluid ^{4}He in these ranges of pressure and temperature, and the first determination of the thermal conductivity ratio for any material for a substantial range of melting temperatures. The overall accuracy of the results has been estimated at between 5% and 10%.

The results of this experiment show that the fluid thermal conductivity increases linearly in the temperature just above the melting point, and that the overall behaviour is dominated by the fluid specific heat for temperatures ranging from the melting point up to the maximum observed temperature (80 K), in accord with fluid structure and transport models due to Horrocks and McLaughlin. The results are numerically low by at least 30% compared with the Chapman-Enskog theory of heat transport for a dense hard sphere gas, although the shape of the curves is similiar. However, predictions based on a model Lennard-Jones fluid are in worse agreement.

The ratio of thermal conductivities at equilibrium (β) was found to be anomalously high, having a value near 4 at a melting pressure of 2 kbar and rising to $\beta \sim 10$ as $P \rightarrow 0$. The change in β for ^{4}He over the observed temperature range is in general agreement with the trend displayed by other quantum solids, suggesting that premature melting in ^{4}He is a quantum effect.

ACKNOWLEDGEMENT

I would like to express sincere gratitude to my supervisor, Prof. J. P. Franck, for his indispensible guidance, support and encouragement during all phases of this project. I am also indebted to Dr. J. Jung for numerous discussions and much helpful advice.

I would like to express my appreciation for the expert technical assistance of Mr. Alan O'Shea who constructed most of the apparatus and contributed many useful ideas, Mr. Pat Wong for the programmable power supply and help with the computer, Mr. Steve Rogers of the University Liquid Helium Facility, and Mr. Ray Pegington of the Physics Machine Shop for constuction of the cell and concentric cylinders. I am grateful to my fellow students Yu Ming-Kang, Ning Yeubin, Ken McGreer and George Tsoupros for many interesting discussions.

And to my wife Katherine for her generous support and many sacrifices:

THANK YOU!

Contents

1 Introduction **1**

1.1 The Goal of this Project 1

1.2 Outline 3

2 Theoretical Background in Review **4**

2.1 Thermal Conductivity of a Dielectric Solid 4

2.2 Dendritic Solidification 18

2.3 Thermal Conductivity of Fluids 28

2.3.1 Dense Gases 28

2.3.2 Liquids 32

3 Experimental Method **35**

3.1 Review of Established Techniques 35

3.2 Theory of Operation 41

3.3 Details of Apparatus 48

3.3.1 External High Pressure Cell 48

3.3.2 Electrical Feedthrough 54

3.3.3 Concentric Cylinders 61

3.3.4 Thermocouples 67

3.3.5 Cryostat and High Pressure System 70

3.4 Experimental Method 75

3.4.1 Details of Method 75

3.4.2 Review of Method 85

3.4.3 Details of the Calculations 87

4 Results **100**

4.1 System Testing 100

4.2 General Results 107

5 Discussion **131**

5.1 Uncertainties 131

5.2 Theory of Dendritic Solidification 133

5.3 Thermal Conductivity Peak in Transition Phase 141

5.4 Comparison with Theories of the Dense Gas and Fluids 142

5.5 Proposals 158

5.6 Conclusions 159

6 Bibliography **162**

A Graphs of the Raw Data **171**

B Comparison with MET **189**

C Thermal Conductivity of the Fluid **197**

List of Figures

2.1 Phonon-phonon scattering (p = 3). 11

2.2 Normal and Umklapp processes. 14

2.3 Formation of Solid 21

2.4 Pattern formation on a Solidification Front. 25

3.1 Heat Flux in a Fluid 43

3.2 Schematic Diagram of Experimental Arrangement. 49

3.3 Schematic Diagram of the Electrical Feedthrough 55

3.4 Schematic Diagram of the Concentric Cylinders 62

3.5 Manufacture of Thermocouples 68

3.6 High Pressure System 71

3.7 Schematic Diagram of Complete System 73

3.8 Pressure and Boil-off Control for the Cryostat 77

3.9 Wiring Circuit for Thermocouples 80

3.10 Wiring Circuit for Inner Cylinder Heater 81

3.11 Heat Pulse in Thermocouple Voltage 84

3.12 Thermopower of Au-Fe vs. Chromel 88

3.13 Temperature Profile between Cylinders 92

3.14 Phase Diagram and Equations of State 98

4.1 Linearity Test of the System 102

4.2 Thermal Conductivity as a function of heater power. 103

4.3 Comparison with Previous Work 106

4.4 Thermal Conductivity of solid and fluid helium at low pressure 111

4.5 Phase Diagram and the $13.00\frac{cm^3}{mole}$ isochore 115

4.6 Liquidus and Solidus lines in Helium 116

4.7 Thermal Conductivity versus Pressure (isochoric freezing) . . 119

4.8 Thermal Conductivity versus Pressure 122

4.9 Thermal Conductivity Ratio versus Melting Pressure 123

5.1 σ^* as a function of β according to equation (5.10) 139

5.2 Thermal Conductivity of Fluid ^{4}He along isobars 145

5.3 Specific Heat of ^{4}He along isochores 149

5.5 Specific Heat of ^{4}He along specified isobars (expanded view of Figure 5.4) 151

5.6 Graph of $Z = v \cdot \rho \cdot a$ as a function of pressure 157

A.1 Trial No. 1 173

A.2 Trial No. 1 174

A.3 Trial No. 2 175

A.4 Trial No. 2 176

A.5 Trial No. 3 177

A.6 Trial No. 3 178

A.7 Trial No. 4 179

A.8 Trial No. 4 180

A.9 Trial No. 5a 181

A.10 Trial No. 5a 182

A.11 Trial No. 5b 183

A.12 Trial No. 5b 184

A.13 Trial No. 6 185

A.14 Trial No. 6 186

A.15 Trial No. 7 187

A.16 Trial No. 7 188

C.1 Trial No. 1 198

C.2 Trial No. 2 199

C.3 Trial No. 3 200

C.4 Trial No. 4 201

C.5 Trial No. 5a 202

C.6 Trial No. 5b 203

C.7 Trial No. 6 204

C.8 Trial No. 7 205

List of Tables

2.1 Thermal Conductivity Behaviour in a Dielectric Solid 6

4.1 Constants in the Simon melting equation 108

4.2 Summary of Trials. The first two digits in λ_f and λ_s are considered significant. 110

4.3 Speculated Transition Widths and Thermal Conductivity . . . 121

4.4 Quantum Parameter and β for various Elements 128

A.1 Raw data graph Locator 172

Chapter 1

Introduction

1.1 The Goal of this Project

The analytic study of dendritic solidification in helium [1] [2] has shown that this system principally follows the predictions of models [3] [4] [9] and has characteristics in common with succinonitrile [13]. Experimental data for reduced tip radius, growth velocity and Peclet number can be well fitted to theoretical power law relationships over two orders of dimensionless supercooling. The observed growth velocities and stability parameter σ for helium are, however, much smaller than predicted. The reasons for these disparities are presently unknown.

The dendrite problem simultaneously involves properties of the solid and fluid phases. Attempts to associate dendrite models with observation reveal the deficiency of data on the fluid phase [15]. In the case of helium, obligatory low temperatures and high pressures have historically conspired against measurement of thermophysical and transport properties. The study of dendrites revealed the need for new experiments to determine the thermal conductivity of solid and fluid helium, both near and away from the melting line. As shall subsequentially be shown, the ratio of thermal conductivities of solid and fluid at equilibrium at the melting point is a critical factor in dendritic growth. For helium, it is entirely unknown. Measurement of this ratio became the object of this project, motivated by the desire to understand the unique features of dendrites in helium. Progress towards this goal has shown that the ratio *per se* is also of considerable interest.

The method of the "steady state guarded concentric cylinders" was selected for this experiment since it best satisfied the experimental requirements. The need for high pressures and the comparative ease of manufacture suggested a cell and measuring device of cylindrical symmetry. This method has a long history of development to which is added the present adaptations and refinements.

1.2 Outline

The structure of this thesis consists of the following major chapters:

- Chapter 2. A review of the theoretical background underlying thermal conductivity of solid dielectrics; an overview of the theory of dendritic pattern formation in crystals; a review of models of thermal conductivity in fluids.
- Chapter 3. A description of the experimental apparatus used in this project and the method employed to obtain results.
- Chapter 4. Presentation of the primary and derived experimental results with interpretation.
- Chapter 5. Conclusions and proposals for anticipated experiments.

Chapter 2

Theoretical Background in Review

2.1 Thermal Conductivity of a Dielectric Solid

The intent of this section is to identify and account for the salient features of thermal conductivity of a dielectric solid as a function of temperature, or density. The subject of heat transport in this regime has been under investigation for many decades, beginning with the theory of Debye [5] and

the work of Peierls [6]. Today, with a few notable exceptions (e.g., the effect of dislocations, the case of amorphous solids, and the high temperature limit), it may be said that there are no outstanding mysteries concerning this problem. Formulations of thermal conductivity on the basis of quantum theory generally encounter intractable mathematical difficulties; nevertheless, a clear temperature dependence of thermal conductivity can be identified, which has been well confirmed by experiment.

With a little hindsight, the behaviour of heat transport with declining temperature may be classified into four regions (Θ_D is the Debye temperature, and λ is the thermal conductivity). Refer to Table 2.1.

While these temperature ranges have been generalised from the case of pure materials, the observed behaviour has these 'universal' features. Deviations are found, naturally, for impure or polycrystalline samples; the usual effect is to reduce λ(max.). The relevant regions in this project are I and II, since a dielectric solid is expected to display this behaviour near the melting point. Poiseuille flow refers to the hydrodynamic flow of fluid in pipes or channels where the velocity profile has a parabolic shape; the fluid layer at the wall sheilds the central volume of fluid from scattering mechanisms which dissipate energy. Since there is less friction in the central volume there

Region	Temp. (K)	λ $Wm^{-1}K^{-1}$	Dominant Feature
I	$T \lesssim T_m$	$\propto T^{-1}$	
	$\frac{\Theta_D}{20} < T \ll T_m$	$\propto exp(\frac{\Theta_D}{2T})$	Umklapp
II	$\sim \frac{\Theta_D}{20}$	(maximum)	Umklapp maximum
III	$T \lesssim \frac{\Theta_D}{20}$	$\propto T^{6-8}$	Poiseuille flow
IV	$0 < T \ll \frac{\Theta_D}{20}$	$\propto T^3$	specific heat

Table 2.1: Thermal Conductivity Behaviour in a Dielectric Solid

is an increase in flow, or, in the case of heat transport, an increase in the coefficient of thermal conductivity. Poiseuille flow in the phonon system, expected to enhance heat transport below the Umklapp maximum according to a T^6 to T^8 law, has been found to decrease with pressure in helium [37]. An interesting symptom of Poiseuille flow is that the effective mean free path of phonons, calculated on the basis of the kinetic model (see equation (2.1) below), can exceed the diameter of the sample [70].

The theoretical explanation for these features may be separated into two approaches: (a) the rigorous development of a heat current quantum mechanically, and (b) the intuitive picture. The former carries and offers the weight of rigor but suffers from unavoidable approximations and reductions; the latter, though simple and lacking precision, is straightforward.

The intuitive picture [16] begins by drawing an analogy between an ideal gas and an inferred 'gas' of phonons, which is able to pass through a crystal subject to identifiable scattering processes. The usual understanding of a phonon as an unlocalised wave disturbance permeating the entire crystal is unsuitable in this analogy; instead, the appropriate construct is the wave packet, i. e., the superposition of normal modes in a neighbourhood $\Delta\vec{k}$ about some $\vec{k}$ which produces a well-defined, localised particle (or, 'quasiparticle').

The thermal conductivity of an ideal gas:

$$\lambda = \frac{1}{3} c_v v l \tag{2.1}$$

traceable to simple kinetic theory and applicable to a broad range of densities (except when the mean free path, l, is of the order of dimensions of the container), becomes the key to this informal picture of lattice heat transport. c_v is the isochoric specific heat per unit volume, v is the particle velocity, and l is the mean free path between particle-particle collisions. Phonon scattering processes in a crystal include a variety of temperature-dependent ones (and -independent, such as dislocations and impurity atoms) which strongly affect l and, in turn, the thermal conductivity. In the analogy to a phonon gas, c_v corresponds to the isochoric lattice specific heat (per unit volume), v is the speed of sound, and l is an estimate of the mean free path between phonon 'collisions' (i.e., collisions with lattice defects, or other phonons), the rigorous calculation of which for a phonon gas has proven to be difficult.

Several important points must be made in connection with phonon scattering in a lattice. First of all, the harmonic approximation in either the classical or quantum picture completely fails the heat transport problem. By 'harmonic' is meant the incorporation of terms up to only second order in the

lattice potential energy, which is usually written as a 3-D Taylor's expansion about $\vec{u}(\vec{R})$, the deviation of an atom from its *average* lattice site. Since normal modes are stationary states of the harmonic Hamiltonian, any distribution of phonons which carries a heat current would not change throughout time, which implies for a perfect crystal the possibility of vanishing thermal resistance. With the exception of superfluid helium, such a property is not found in nature, –certainly not in any solid. Secondly, the harmonic approximation is invalid in the particular case of helium, since here we have the unique combination of weak Van der Waals interaction, a relatively light atom, and very large zero-point motion. (These are responsible for the high isothermal compressibility of helium, and the existence of the liquid phase near $0K$.)

Ignoring for the moment phonon scattering due to granularity, crystal imperfections (dislocations and other defects), and impurities, the other scattering mechanisms must lie in the neglected 'anharmonic' terms, or terms of order three and higher, which exist in the true crystal potential. Cubic and quartic anharmonic terms are included in the total Hamiltonian as a perturbation and treated by that well known method. The essential outcome of these calculations is the possiblity of transitions between eigenstates of the

harmonic Hamiltonian, which are interpreted as phonon-phonon interactions or 'collisions'. It turns out that the order of the anharmonic term, p, introduces interactions involving just p phonons. As an example, given here without proof, consider all possible interactions wherein $p = 3$ (i.e., cubic anharmonicity):

1. creation of $p = 3$ phonons $(n_1(\vec{k_1}) \rightarrow n_1(\vec{k_1}) + 1; n_2(\vec{k_2}) \rightarrow n_2(\vec{k_2}) + 1; n_3(\vec{k_3}) \rightarrow n_3(\vec{k_3}) + 1)$

2. annihilation of $p = 3$ phonons $(n_1(\vec{k_1}) \rightarrow n_1(\vec{k_1}) - 1; n_2(\vec{k_2}) \rightarrow n_2(\vec{k_2}) - 1; n_3(\vec{k_3}) \rightarrow n_3(\vec{k_3}) - 1)$

3. creation of 2 phonons, annihilation of 1 $(n_1(\vec{k_1}) \rightarrow n_1(\vec{k_1}) - 1; n_2(\vec{k_2}) \rightarrow n_2(\vec{k_2}) + 1; n_3(\vec{k_3}) \rightarrow n_3(\vec{k_3}) + 1)$

4. creation of 1 phonon, annihilation of 2 $(n_1(\vec{k_1}) \rightarrow n_1(\vec{k_1}) - 1; n_2(\vec{k_2}) \rightarrow n_2(\vec{k_2}) - 1; n_3(\vec{k_3}) \rightarrow n_3(\vec{k_3}) + 1)$

where $n(\vec{k})$ refers to the occupation number of the mode with wavevector $\vec{k}$ (polarisation ignored). Pictorially, these processes are represented in reciprocal space by Figure 2.1. Conservation of energy clearly must prohibit

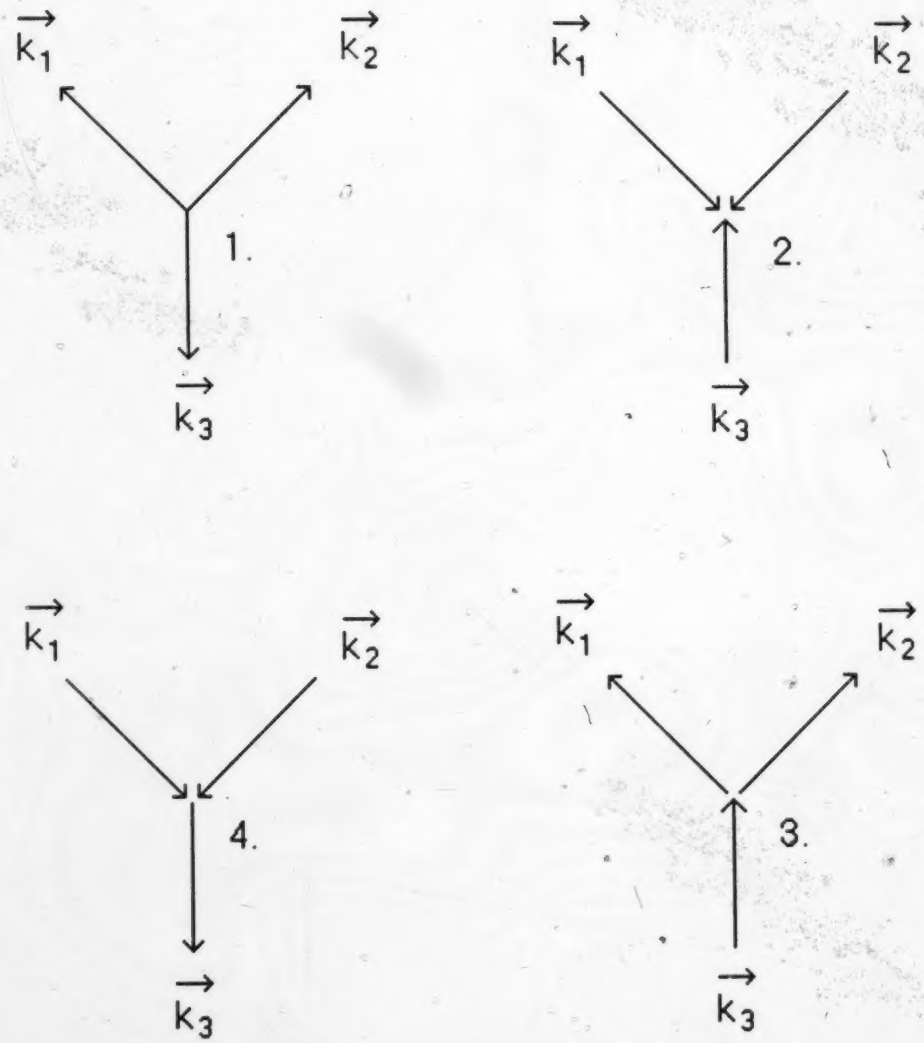

Figure 2.1: Phonon-phonon scattering (p = 3).

processes (1.) and (2.), since the energy of each normal mode is given by:

$$E_{\vec{k}} = (n(\vec{k}) + \frac{1}{2})\hbar\omega(\vec{k}) \tag{2.2}$$

where $\omega(\vec{k})$ is the angular frequency associated with the $\vec{k}$-th mode. The conservation laws for energy and momentum impose restrictions on the participants of processes (3.) and (4.). The net effect of the cubic perturbation terms is to introduce phonon-phonon scattering processes which can be understood to degrade the heat current consistent with experimental findings.

Process (4.) implies a property unique to discontinuous, periodic media: the law of momentum conservation for phonons always includes a reciprocal lattice vector, $\vec{K}$, such that 'momentum conservation' is modulo $\vec{K}$:

$$\vec{k_1} + \vec{k_2} = \vec{k_3} + \vec{K}. \tag{2.3}$$

It is possible for $\vec{K}$ to be zero or non-vanishing; the former case is termed 'normal', whereas the latter is 'umklapp' from the German 'Umklapprozesse' ('flop over' process). The existence of U-processes only in discontinuous (i.e., periodic, as opposed to continuous) media is critical to the understanding of lattice thermal conductivity. Momentum conservation in this context may better be referred to as an 'interference condition', since the momentum $\hbar\vec{k}$, associated with a particular phonon is not *transferred* by that phonon. To

establish the distinction between this context and that of an ordinary free particle, the term 'crystal momentum' has been coined for the quantity $\hbar\vec{k}$, and it is this which is subject to the interference condition.

An umklapp process is understood to simply be the 'folding' (or, 'flopping') back of a phonon wavevector, $\vec{k_3}$, by an amount $\vec{K}$ which is one of the principle reciprocal lattice vectors. This occurs if the resultant phonon $\vec{k_3}$ extends beyond the border of the first Brillouin zone, since any such wave is equivalent to a disturbance having smaller wavenumber $\vec{k_3}'$ (or, larger wavelength) moving in a different direction (see Figure 2.2). This is consistent with the general rule that all wavevectors which represent phonons must lie within the boundaries of the first Brillouin zone.

With the machinery of phonon-phonon interactions and the umklapp process, a qualitative description of the underlying behviour may be given. At high temperatures ($T \geq \Theta_D$) phonon occupation numbers are expected to be relatively high, and, using the Bose-Einstein distribution, they can be estimated:

$$n(\vec{k}) = \frac{1}{e^{\left(\frac{\hbar\omega(\vec{k})}{k_B T}\right)} - 1} \sim \frac{k_B T}{\hbar\omega(\vec{k})}. \tag{2.4}$$

Since the number of phonons increases with temperature, it may be in-

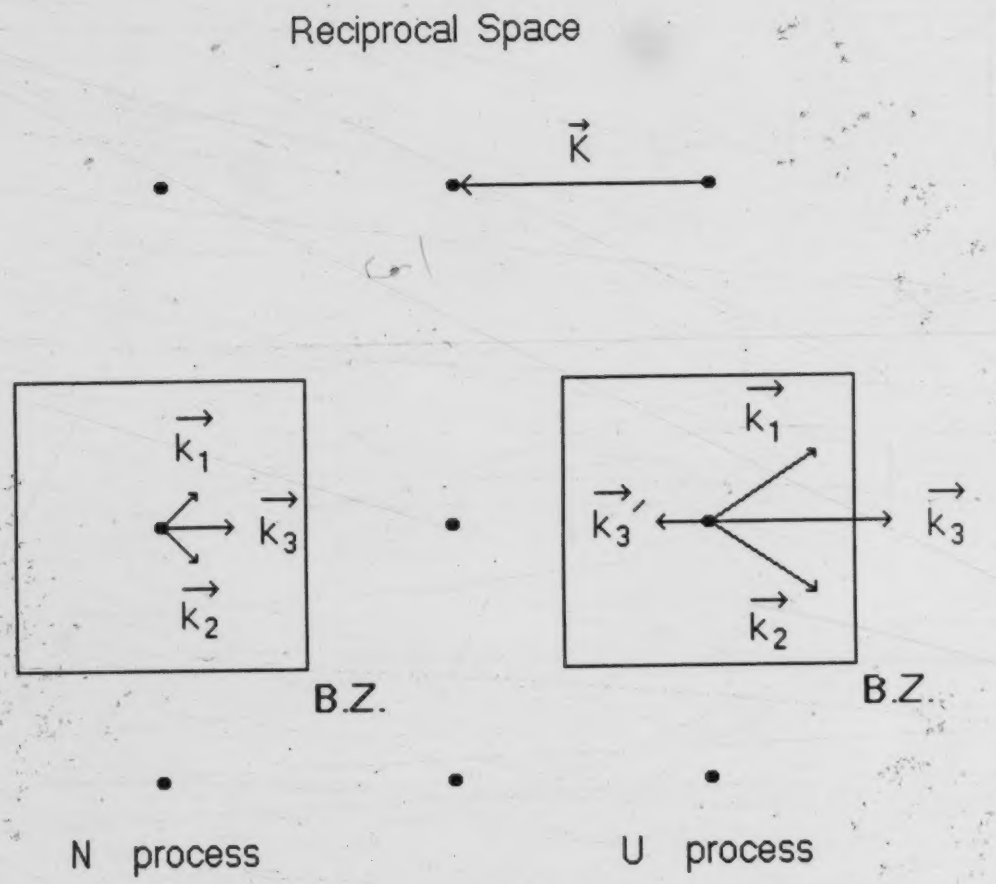

Figure 2.2: Normal and Umklapp processes.

ferred that the collision frequency would also increase, or, alternatively, that mean free path between collisions would decrease. Recalling equation 2.1, and remembering that the specific heat is approximately a constant function of temperature (except at low temperatures), it is clear that $\lambda \sim T^{-1}$, which has been confirmed by experiment [17].

A further comparison with the kinetic theory of an ideal gas can be made at this point. It will be recalled that the mean free path of a particle is given by [18]:

$$l = \frac{1}{\sigma \rho} \tag{2.5}$$

where σ is the atomic cross section and ρ is the number density. If, for the case of a gas of phonons, ρ is identified with the occupation number $n(\vec{k})$, and σ with phonon-phonon coupling (assumed constant), then the same temperature dependence of l and λ is suggested.

At slightly lower temperatures, the effect of the umklapp process as the singularly dominant form of phonon scattering becomes quite apparent. Clearly, for this process, phonons of a certain minimum wavenumber are required. This critical size may be generalised as one-half of a reciprocal lattice vector: i.e., either one, or both of the interacting phonons must have a

wavevector of $\vec{k} \geq \frac{1}{2}\vec{K}$. This requirement is needed in order to push the size of the resultant third phonon beyond the Brillouin zone. This limitation is realised only at temperatures above which the population of required short-wavelength, higher energy phonons is significant. Setting $\hbar\omega(\vec{k}) \sim \frac{1}{2}\hbar\omega_D$ since one of the interaction phonons should have an energy comparable to one-half the Debye limit, then:

$$n(\vec{k}) = \frac{1}{e^{\frac{\hbar\omega(\vec{k})}{k_B T}} - 1} \sim \frac{1}{e^{\frac{\Theta_D}{2T}} - 1} \tag{2.6}$$

which, for $T < \Theta_D$, reduces to:

$$n \propto e^{\frac{-\Theta_D}{2T}}. \tag{2.7}$$

Evidently, the probability of an umklapp process decreases exponentially with falling temperature, which may be translated into the statement that the thermal resistance exponentially decreases; such exponential behaviour is confirmed by experiment. An alternative terminology for these events would have a 'freezing' out of the umklapp process as the temperature was reduced, with the concomitant increase in thermal conductivity.

It can be shown that a normal process (i.e., one in which crystal momentum is conserved exactly) cannot degrade the thermal current [19]. Suppose

that a crystal was prepared with a non-zero total crystal momentum $\vec{P}$ corresponding to a net heat current:

$$\vec{P} = \Sigma_{\vec{k}} n(\vec{k}) \hbar \vec{k} \tag{2.8}$$

Since $\vec{K} = 0$ for Normal processes, this sum would not be altered by these processes alone and the heat current would also remain unaltered. The net energy flux would be distributed amongst a different set of phonon modes rather than being modulated.

As umklapp processes are frozen out to greater degree at lower temperatures, this would imply a thermal conductivity rising to infinity as $T \rightarrow 0$ since the mean free path could grow unhindered. Even the inevitable lattice imperfections and impurities could not completely eliminate this inexorable theoretical increase, but the finite size of any real specimen *could* by imposing a strict upper limit on l. Some studies have even shown that polishing the sample, which enhances specular surface scattering (reflection) of phonons, has the effect of increasing the net conductivity [7] [8].

At some point (often $T \sim \frac{\Theta_D}{50}, \lambda = \lambda(max.)$) the mean free path is limited by either the size of the specimen (single crystal) or the size of grains, and the conductivity behaviour below this peak is becomes dominated by the

specific heat. This is obvious from equation (2.1) for fixed l. As $C_v \propto T^3$ for $T \ll \Theta_D$ it would be expected that $\lambda \propto T^3$ as well, and there is ample evidence to confirm this [20].

2.2 Dendritic Solidification

The ancient Greek "dendron" (Gk. 'tree') is the root of the modern word "dendrite", which describes metallurgical, geological, zoological, and anatomical structures having tree-like shapes, i.e., a central projected 'trunk' possibly with side branches. In respect of the present study, it refers to crystallisation of solid helium from the undercooled melt (i.e., liquid below the 'normal' freezing point temperature at a given pressure). Such non-equilibrium conditions can be created in the laboratory either by rapid or very careful cooling. The technical importance of the study of dendritic crystallisation stems from the strength and corrosion resistance properties of metallic alloys which have this structure, but dendrites are actually widespread in nature (consider the common snowflake), and are of general theoretical interest as an example of crystal growth that is remarkably sensitive to growth conditions and material parameters. Dendritic solidification has also been examined in the context of

nonlinear dynamical theory [12]; a moving boundary (solidification front) between solid and fluid displays bifurcations and chaotic behaviour at increasing translation velocity, appearing much like viscous fingering in Hele-Shaw cell experiments.

Interest in dendrites is focussed on several questions: do 'univeral' relationships between growth parameters (tip radius, growth velocity, and degree of undercooling) exist? and, how are the complex shapes of dendrites 'selected' by nature (or, why *are* complex shapes selected at all, instead of simple or purely disordered ones)? If precise answers to these questions are, at present, lacking, some general aspects of the problem are evident. The controlling factor appears to be the relative magnitude of thermal diffusion of both solid and fluid, favoring configurations having the largest surface areas; simple shapes such as rods, spheres, or plates, etc., are unstable and quickly give rise to complex 3-dimensional structures which rapidly amplify the surface area and the ability to transfer heat.

To clarify this point, consider, after Langer [9], two disparate solidification regimes (Figure 2.3). In both cases, we have a container filled with a pure fluid. In (a), the container itself is below the melting point (T_M) and solidification has occured first on the walls. The solid grows slowly and

uniformly from the stable fluid phase under conditions of thermodynamic equilibrium. The latent heat of fusion released at the interface is, by necessity, conducted through the solid to the surroundings at $T \leq T_M$. In (b), the fluid has somehow been cooled below its normal freezing point and solidification has been initiated in the interior away from the walls, possibly through homogeneous nucleation or introduction of a 'seed' crystal. Now the latent heat must be conducted through a surrounding layer of undercooled fluid, and the crystal expands into this metastable phase. This is growth governed by non-equilibrium dynamics, and complicated underlying pattern formation rules come into play which can lead to dendritic shapes.

To found these ideas mathematically, a model has been developed [9] based on the Mullins-Sekerka stability criterion [3] [4]. The framework of the model consists of three principle equations which, it is believed, contain information on any possible crystallisation pattern. This set of coupled non-linear differential equations do not directly offer ready solutions, but much insight can be gained through their application first to simple systems and then to progressively more realistic examples. In the interest of clarity, the hidden algebraic steps and required approximations will be ignored, with only the relevant conclusions offered in this presentation.

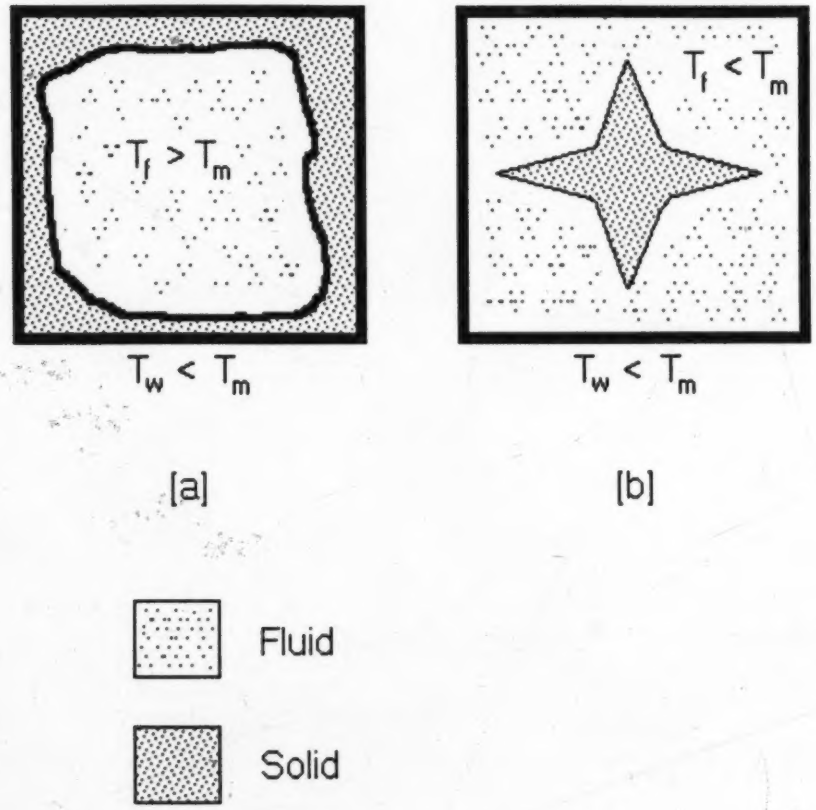

Figure 2.3: Formation of Solid

The set of equations include the temperature diffusion equation, an equation of heat conservation at the solid-fluid interface, and the Gibbs-Thompson equation for the decrease (or increase) of the melting temperature as a function of the curvature of the interface:

$$D\nabla^2 T - \frac{\partial T}{\partial t} = 0, \tag{2.9}$$

$$Lv_n = (D'c_p'(\nabla T)_s - Dc_p(\nabla T)_f)) \cdot \hat{n}, \tag{2.10}$$

$$T_{interface} = T_M \left[1 - \frac{\gamma\kappa}{L}\right]. \tag{2.11}$$

In the second of these equations, L is the latent heat of fusion per unit volume, giving on the right hand side the heat released per unit area of the interface. Primed terms refer to the solid phase, unprimed to the fluid phase.

By introducing a reduced temperature 'u' and a frame of reference which moves with velocity v_n of the growing interface, these equations may be recast into a slightly more useful form (where $z' = z - v_n t$):

$$\nabla^2_{z'} u + \frac{2}{l}\frac{\partial u}{\partial z'} = 0, \tag{2.12}$$

$$v_n = D\left[\beta(\nabla u)_s - (\nabla u)_f\right] \cdot \hat{n} \tag{2.13}$$

$$u_{interface} = -d_o\kappa, \tag{2.14}$$

where various terms have the following definitions:

1. $v_n = \frac{\partial z}{\partial t}$, interface growth velocity,

2. $u = \frac{T - T_M}{\frac{L}{c_p}}$, reduced undercooling,

3. $\beta = \frac{\lambda'}{\lambda}$, ratio of thermal conductivities of solid and fluid,

4. $d_o = \frac{\gamma T_M c_p}{L^2}$, the "capillary length",

5. $l_t = \frac{2D}{v}$, the "thermal diffusion length",

6. $D = \frac{\lambda}{c_p}$, thermal diffusivity,

7. T_M: equilibrium melting temperature,

8. c_p: specific heat per unit volume,

9. γ: fluid-solid surface tension,

10. κ: surface curvature ($\kappa = \frac{1}{r}$).

To demonstrate the model, consider first a planar interface $\theta(\hat{x}, t) = z$, with $\hat{x}$ the 2-dimensional vector in the plane of the growing solidification front (Figure 2.4(a)). The solution to the steady state diffusion equation is given by:

$$u = \begin{cases} exp\left[\frac{-2z'}{l_t}\right] - 1 & \text{liquid, } z' \geq 0 \\ 0 & \text{solid, } z' < 0, \end{cases} \tag{2.15}$$

which gives a unit undercooling at infinity, but does not relate the growth velocity to degree of undercooling.

A sinusoidal perturbation is now imposed onto the interface and the model attempts to predict how this perturbation will behave in the future (Figure 2.4(b)). The form of the perturbation is given by:

$$\hat{\theta}_k = exp(i\vec{k} \cdot \vec{x} + \omega_k t). \tag{2.16}$$

$\vec{k}$ is some 2-dimensional wavevector perpendicular to $\vec{v}$ which represents the physical size of the perturbation, and ω_k is a corresponding "growth parameter" (one for every 'k'). Formally, one must solve the time independent diffusion equation (2.12) subject to the boundary condition (2.14), and insert the result into the continuity expression (2.13) to obtain an explicit expression for $\theta(\hat{x}, t)$. Following these steps, Langer derives an approximate expression for the growth parameter, ω_k, subject to the condition that $kl_t \ll 1$:

$$\omega_k \sim \left[kv - (1+\beta)d_o k^3 D\right] \tag{2.17}$$

This expression represents the competition between two countervailing effects: a positive destabilising term proportional to the velocity and a negative, stabilising term containing the surface tension. In the vicinity of one

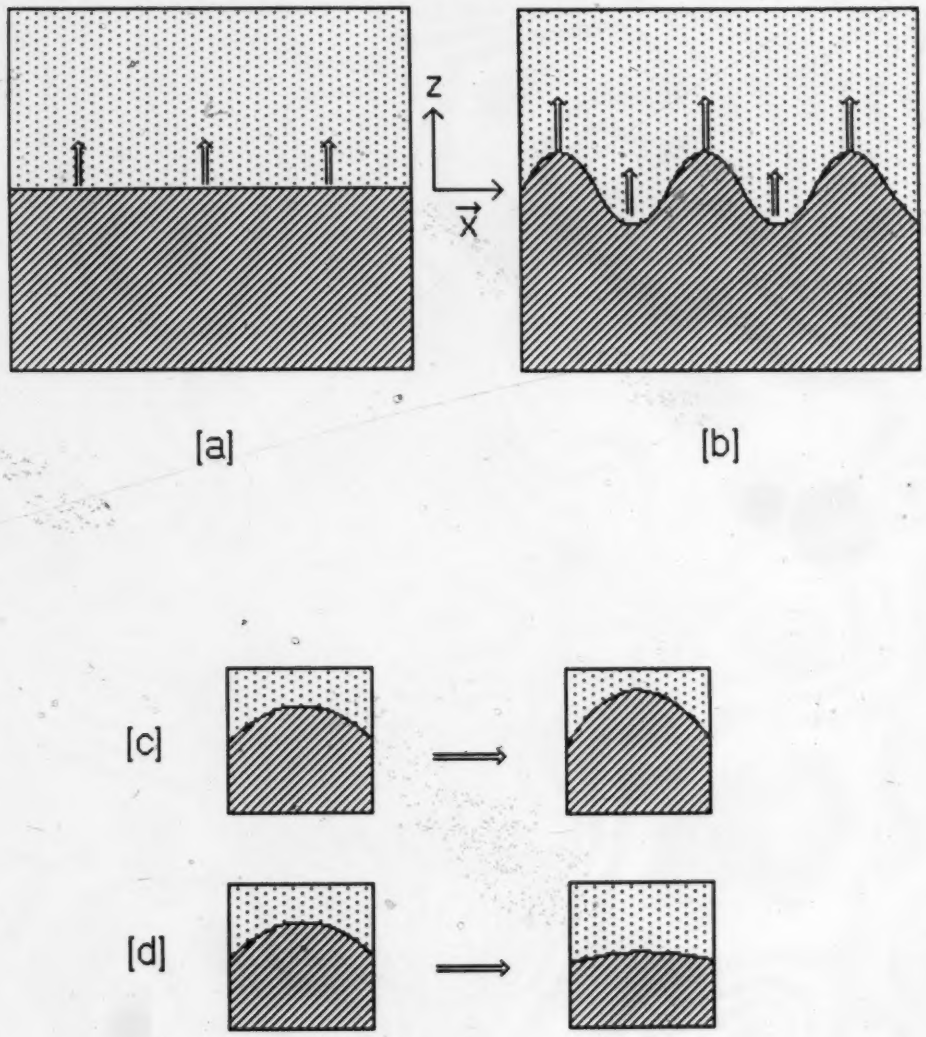

Figure 2.4: Pattern formation on a Solidification Front.

of the sinusoidal 'bulges' projecting into the undercooled melt, the temperature gradient in the fluid will be steeper, which accelerates the growth of the bulge. But the Gibbs-Thompson equation (capillary effect) reduces the temperature of the forward bulge and, likewise, increases the temperature of adjacent depressions. The relative strength of these two mechanisms determines the ultimate shape of the deformed interface.

According to the original definition, the perturbation will continue to grow if $\omega_k > 0$ (destabilising, Figure 2.4(c)), or will diminish in size if $\omega_k < 0$ (stabilising, Figure 2.4(d)). For a growth parameter that is identically zero there is a critical wavelength associated with the sinusoidal perturbation:

$$\omega_k = 0, \tag{2.18}$$

$$k_{stab} = \left[\frac{2}{(1+\beta)(d_o l_t)}\right]^{\frac{1}{2}}, \tag{2.19}$$

$$\lambda_{stab} = \frac{2\pi}{k_s} = 2\pi\alpha\sqrt{d_o l_t}, \tag{2.20}$$

where the 'stab' subscript refers to 'stability', and $\alpha = \sqrt{\frac{1+\beta}{2}}$. Evidently, critical stability exists when $\omega_k = 0$ leading to enhanced growth of perturbations having characteristic wavelength λ_{stab}, and the deformed interface should exhibit dendritic spacing or side-branch spacing of order λ_{stab}. Furthermore, the fastest growing dendrite should have wavenumber $k_{stab}/\sqrt{3}$,

which can be seen if ω_k is maximised with respect to the wavevector k. The dependence of this critical wavelength on the thermal conductivity ratio β is evident. For helium (to be shown) $\beta > 1$, whereas, for most substances, the ratio is ~ 1 [66], and in the model under consideration it is sometimes assumed that $\beta \ll 1$ since this corresponds to the metallurgically interesting case.

The model has been developed beyond the relatively simple case of the directional solidification front examined by Mullins and Sekerka; cases including the growing sphere and a needle dendrite (a paraboloid of revolution with circular cross-section) have also been critically analysed. Perhaps the most important experimental observation is that the degree of undercooling always seems to fix the growth velocity of dendrites and, in turn, the tip radius,–i. e., there evidently is some underlying relationship linking these factors. It is expected that the model will provide numerical values of the growth velocity, etc., but this has yet to be achieved conclusively [10] [11].

Observations have shown that the product vr_t^2 = constant (material dependent), and that the Peclet number, $p = vr_t/2D$ is in good agreement with theoretical predictions [1]. What remains is to be shown is that unique values of v and r_t are selected by the growing dendrite for a given undercooling.

Langer has proposed that the dendrite selects a growth velocity such that the tip is marginally stable against splitting (i.e., side branching behaviour *at* the tip). This marginal stability hypothesis is expressed quantitatively in the term $\sigma = 2Dd_o/vr_t^2$, such that for $\sigma < \sigma^*$ (the critical point), the tip is unstable; the dendrite then grows with $\sigma \sim \sigma^*$. Numerical simulations of dendritic solidification and the extended model of the growth of spheres and needles have indicated that σ^* probably has a value in the neighbourhood of 0.019 to 0.025. This matter will be further discussed in Chapter 5.

2.3 Thermal Conductivity of Fluids

2.3.1 Dense Gases

Distinctions between and amongst the terms 'gas', 'vapour', 'fluid', and 'liquid' do not seem generally accepted, so in the etymological view perhaps a 'dense gas' and 'fluid' are one and the same. However, in the realm of statistical mechanical theories a clear distinction exists and the two cases are examined from divergent standpoints.

There are three principle intermolecular transport mechanisms in fluids:

transport of mass (defined by the coefficient of diffusion or self-diffusion), the transport of momentum (defined by the coefficient of viscosity), and the transport of energy (defined by the coefficient of thermal conductivity). Each of these may be described by a similiar flux equation of the following form, with the particular coefficient uniquely dependent on the substance and its physical state (pressure, density, temperature):

$$\vec{Q} = -K\nabla\Phi \tag{2.21}$$

where $\vec{Q}$ is the flux vector, K is the coefficient, and $\nabla\Phi$ is the gradient of a system parameter (diffusion: species concentration; viscosity: velocity of adjacent fluid layers; thermal conductivity: temperature). These coefficients may be calculated on the basis of certain sets of assumptions regarding the form of intermolecular interactions (e. g., hard sphere, Lennard-Jones-Devonshire potential, etc.), and, when the magnitudes are compared with experimental values, conclusions may be drawn as to the validity of the assumptions. In other words, the transport coefficients are the only 'windows' that we have on real situations and the only means at our disposal to test statistical theories.

In the dilute gas limit it is assumed that the particles have vanishing size,

or have dimensions very much smaller than their average spacing. The results of calculations of the thermal conductivity coefficient from the Boltzmann Equation in the dilute gas limit [47] are given as follows:

$$\lambda_1 = (8.3224 \times 10^{-3}) \frac{\sqrt{T/M}}{\sigma^2 \Omega^{(2,2)*}(T^*)}, \tag{2.22}$$

$$\Omega^{(2,2)*}(T^*) = \sqrt{\frac{kT}{2\pi\mu}} \int_0^\infty e^{-\gamma^2} \gamma^7 Q^2(g) d\gamma, \tag{2.23}$$

$$Q^2(g) = 2\pi \int_0^\infty (1 - \cos^2 \chi) b db, \tag{2.24}$$

where $\gamma = \sqrt{\mu g / 2kT}$, μ is the reduced mass, χ is the angle of deflection, b is the impact parameter, and g is the initial relative velocity of the colliding particles. The prefactor constant in equation (2.22) leaves λ_1 in units of $\mathrm{Wm^{-1}K^{-1}}$. σ is the radial separation of particles at contact and T^* is the reduced temperature, given by $T^* = kT/\epsilon$, where ϵ is the minimum of the Lennard-Jones-Devonshire potential:

$$\Psi(r) = 4\epsilon \left[(\frac{\sigma}{r})^{12} - (\frac{\sigma}{r})^6 \right]. \tag{2.25}$$

For helium(4), $\sigma = 2.576\mathring{A}$, $\epsilon/k = 10.22\mathrm{K}$ [47]. In general, the $\Omega^{(2,2)*}(T^*)$ integrals cannot be solved analytically and for practical purposes numerical calculations are required (however, for the rigid sphere case, $\Omega^{(2,2)*}(T^*)$ reduces to 1). Higher approximations (i. e., λ_3) may be made, and are given

by Hirschfelder [47].

The above development is preliminary to the required theory, namely, that for the thermal conductivity of a dense gas (i.e., under high pressure, or at high temperature). Enskog was the first to derive a transport theory based on a model of rigid spheres of diameter σ. Binary collisions only are considered, but, unlike the dilute gas, molecules are assumed to have a non-vanishing size. As the density of a gas is increased, the collision frequency increases because σ is not negligibly small compared to the mean free path, but also decreases because nearest neighbours shield a given molecule from incoming molecules.

The thermal conductivity for a dense gas of rigid spheres in the modified Enskog theory (MET) is given by:

$$\lambda = \frac{\lambda^0 b_o}{\bar{V}} \left[y^{-1} + 1.2 + 0.755y \right], \tag{2.26}$$

where λ^0 is the dilute gas limit value (λ_1), and:

$$y = \frac{b_o Y}{\bar{V}}. \tag{2.27}$$

Y is given by the virial expansion, which is:

$$Y = 1 + 0.625(\frac{b_o}{\bar{V}}) + 0.2869(\frac{b_o}{\bar{V}})^2 + 0.115(\frac{b_o}{\bar{V}})^3, \tag{2.28}$$

where $b_o = \frac{2}{3}\pi N\sigma^3$. b_o is an approximation to the second virial coefficient in the virial equation of state for a real gas of interacting particles:

$$\frac{P\tilde{V}}{RT} = 1 + \frac{B(T)}{\tilde{V}} + \frac{C(T)}{\tilde{V}^2} + \frac{D(T)}{\tilde{V}^3} + \cdots. \tag{2.29}$$

$\tilde{V}$ is the molar volume of the gas.

It has been shown that this expression for the single case of helium gives an excellent representation of the thermal conductivity data at high pressures near room temperature [48] using the experimental values of LeNeindre [49], and that sophisticated modern improvements to the Enskog theory [53] do not seem useful for helium.

2.3.2 Liquids

The approach to thermal conduction in liquids has differed from the case of dense gases. The structural arrangement has been assumed to consist of unimolecular cells with intracellular vibrations and possible intercellular displacements. In fact, the picture is much like that of a solid but with relaxed restrictions on mobility.

However, the most simple model consists of an extension of classical ki-

netic gas theory, which, as noted in section 2.1, gives the following:

$$\lambda = \frac{1}{3} c_v v l. \tag{2.30}$$

For liquids, the most difficult term to evaluate is l, the mean free path between collisions, which for the liquid state, must be quite small and at least not larger than several molecular diameters. The dependence on the isochoric specific heat per unit volume c_v is anticipated if v and l are relatively constant with respect to molar volume or temperature at constant pressure (a reasonable description of the conditions of this experiment).

More advanced theories include the work of Horrocks and McLaughlin [54], who examined thermal conduction under the assumption that the liquid state has a close-packed lattice structure made up of unimolecular cells. Energy transport between layers of the liquid is mediated via two mechanisms: convective motion of molecules from cell to cell, and vibrational transfer of energy by molecules between cells. The magnitude of the convective term was shown to be only about 1% of the vibrational term, leading to a value of the thermal conductivity dependent on the specific heat:

$$\lambda_l = \frac{\sqrt{2}\nu C_v}{a} \tag{2.31}$$

where ν is the intracellular lattice frequency, a is the nearest neighbour dis-

tance, $a = (\sqrt{2}V/N)^{\frac{1}{3}}$, and C_v is the isochoric specific heat per molecule. In the harmonic oscillator approximation [55], the lattice frequency is replaced by:

$$\nu = \frac{1}{2\pi\sqrt{m}}\left[\frac{2Z\epsilon}{a^2}(Lv^{*4} - Mv^{*2})\right]^{\frac{1}{2}}, \tag{2.32}$$

where m is the mass, $Z = 12$ is the co-ordination number, $v^* = \sigma^3/v$, $v = V/N$, and L and M are summation constants having values 22.11 and 10.56, respectively. ϵ and σ are defined in terms of the Lennard-Jones-Devonshire potential, given above.

Chapter 3

Experimental Method

3.1 Review of Established Techniques

Historically, a variety of experimental techniques have been developed to measure the thermal conductivity of fluids (liquids and gases) [21]. These methods fall, generally speaking, into two categories: 'steady state' or 'dynamic'. In recent years, the 'transient hot wire' technique has become the pre-eminent dynamic method owing to high precision and rapid data acquisition by computer [22]. Unfortunately, this method is unsuitable at low temperatures for reasons to be presented later.

The object of the *steady state method* is to set up isothermal surfaces at

known temperatures with a known quantity of heat flowing between them. The sample is confined within the space bounded by these surfaces, and λ is calculated with Fourier's equation. The isothermal surfaces often are just the structural components of the cell, such as external walls. In the pursuit of mathematical simplicity and ease of manufacture, designs are restricted to symmetrical geometries such as planes, cylinders, or spheres. This method requires sensitive appraisal and minimisation of secondary heat flows. The complete heat balance equation (referring to all paths of heat flow into and from thermometer locations) must be examined carefully, all terms identified and either calculated or estimated. As heat flow is a strictly three-dimensional phenomena (there being no examples of perfect or near-perfect thermal insulators), this calculation can become very complicated and tedious. This is a serious problem for the steady state method, and gives rise to a series of correction terms.

A typical steady state experiment uses concentric cylinders; an example is the extensive work of Zeibland and Burton [23] with heavy water as the sample fluid. More recent developments include the work of Tufeu et. al.[24] on rare gases at high pressure. A variation of the concentric cylinder design is that developed by Liedenfrost [25] in which the cylinders were capped by

concentric hemispheres. Each of these methods uses an electrically heated metal cylinder within another cylinder of slightly larger bore; the annular gap that separates them is filled with the sample fluid. By measuring $\dot{Q}$ (heat delivered to inner cylinder and transported across the fluid) and ΔT (temperature difference between cylinders), λ of the fluid may be determined using modified form of Fourier's equation. *This method has been selected for the present project.*

Other steady state experimental designs include horizontal parallel plates, concentric spheres, and the hot wire cell. In the first design, two parallel, circular metal plates are separated by a gap which contains the sample fluid. The upper plate is heated electrically ($\dot{Q}$) and the temperature difference ΔT between plates is monitored. The thermal conductivity of the fluid layer is found to first order through the following equation:

$$\lambda = \frac{\dot{Q}l}{A\Delta T} \tag{3.1}$$

where l is the layer thickness and A is the plate area.

A series of corrections must be made to account for extraneous heat pathways. Usually the upper plate is surrounded by an independently heated guard ring. This design has been used at low pressure and room tempera-

ture [27], as well as for high pressures [28]. The need for a large diameter containment cell (since the plate diameter : gap thickness ratio should be as large as practical), and the presence of large secondary heat flow render this design less desirable than the concentric cylinder method for the present experiment. The horizontal parallel plate geometry is particularly suited to measurements near the critical point of fluids since gravitational convection due to the divergent compressibility of fluids near the critical point is minimised by using a small gap (the fluid is situated in a constant gravitational field).

The concentric sphere design is an extension of the steady state method to spherical geometry [26]. An inner solid sphere is heated; energy flows radially across a fluid-filled space to an outer sphere and, as before, the temperature difference between the spheres is recorded. Practical difficulties inherent in this design,–namely, the problem of precise concentric alignment of the spheres, and the need for a large external pressure cell,–have made the relative simplicity of construction of the concentric cylinder design more attractive. The hot wire cell (steady state), has a single, serious deficiency. A single platinum wire, suspended longitudinally inside a hollow cylindrical cell, is heated electrically and its' temperature history is recorded. The volume

of surrounding fluid is much larger than that in the concentric cylinder case, and undesireable convective flow is more likely (except for the lowest heating rates, at which level the temperature differences would be subject to large uncertainties).

In non-steady state, or *dynamic*, experiments, the objective is to set up conditions corresponding to equation (3.10). In these situations it has been prudent to seek conditions which simplify both the theory and design. It has been shown [21, page 72] that one of the most simple configurations is that of an infinite, continuous line source of heat in a infinite volume of isotropic, homogeneous fluid. An alternative dynamic method also employs coaxial cylinders [40].

The theory of the transient hot-wire experiment assumes a continuous line source of heat immersed in an infinite volume of fluid [29]. In practise, a fine wire is suspended along the longitudinal axis of a hollow cylindrical vessel; the ratio of wire diameter to vessel diameter is typically $\sim 10^{-3}$. The wire is heated by passing a current through it, and the temperature of the wire is recorded as a function of time. Data is recorded with millisecond precision up to the onset of convection. Generally speaking, the rate at which the wire temperature increases is directly dependent on the thermal conductivity of

the surrounding fluid (i.e., the ability to carry away heat).

Since the heating wire is also its' own temperature sensor, a material with good thermal sensitivity ($\frac{dR}{dT}$; R = electrical resistance) is required, and the material of first choice has always been platinum; however, at temperatures below $\sim 20K$, $\frac{dR}{dT}$ for platinum is too small for accurate temperature determination. *The lack of a suitable and convenient replacement for platinum therefore makes the transient hot wire technique unsuitable for the present project.*

The coaxial cylinder (cooling) method developed by Golubev [40] uses concentric, coaxial cylinders which confine the sample fluid in the relatively small annular gap. The inner cylinder is heated briefly and then the heater is switched off. Cooling of the inner cylinder proceeds by conduction of heat across the gap. By monitoring the cooling rate of the inner cylinder as a function of time, λ of the sample may be determined. The key to this method is that the temperature decay is found to be exponential over some time domain called the regular regime, which can conveniently be analysed. However, this method requires a relatively large volume of fluid, a relatively large gap ($\sim 1mm$), and a large temperature difference ($\sim 5K$) between the cylinders in order to be effective. As well, accurate knowledge of the heat

capacity of the heater and its' constituent parts is needed. This method was not selected for the present project.

3.2 Theory of Operation

Although the two elementary equations which form the mathematical foundation of this experiment,– namely, the Fourier Equation and the Equation of Continuity,– are well known, their derivation is straightforward. We begin by considering an isotropic, homogeneous, quiescent fluid medium without sources or sinks of heat.

The Fourier transport equation (1811) is simply an empirical statement: the flux of heat across a given boundary was found to be proportional to the temperature gradient at the boundary:

$$\dot{Q} \propto -\nabla T \tag{3.2}$$

where the constant of proportionality is just the thermal conductivity of the medium.

$$\dot{Q} = -\lambda \nabla T \tag{3.3}$$

The minus sign appears because heat always flows from the hotter to the colder region. The assumptions of isotropicity and homogeneity apply to

fluid properties such as λ, C (specific heat), and ρ (density). Furthermore, is necessary to assume that these same properties are independent of temperature over small temperature intervals, otherwise non-linear differential equations will result and numerical solution will be necessary. Conversely, we can restrict the experimental conditions at the moment of measurement to be 'isothermal' (or, nearly so).

The fluid in question is assumed to be quiescent (convection free); that is, we are interested only in thermal conductivity through the mechanism of intermolecular interactions, without bulk movement of fluid. Convective transport of heat in a fluid, driven by density variations due to temperature gradients, is a complex phenomena beyond the scope or intent of this project. Special consideration was given to ensuring that convective transport could not take place, or would be insignificant (see section 3.3.3).

At some point 'P' in the fluid, we form the usual Cartesian coordinate system (x,y,z) and enclose 'P' at the centre of a small cube of dimensions $(2dx, 2dy, 2dz)$. Refer to Figure 3.1. We assume that there exist continuously variable heat fluxes along the coordinate axes throughout the fluid. However, we assume that the differential cube is uniform in temperature. In the x-direction, we then have a heat flow into the cube at surface ABCD given by

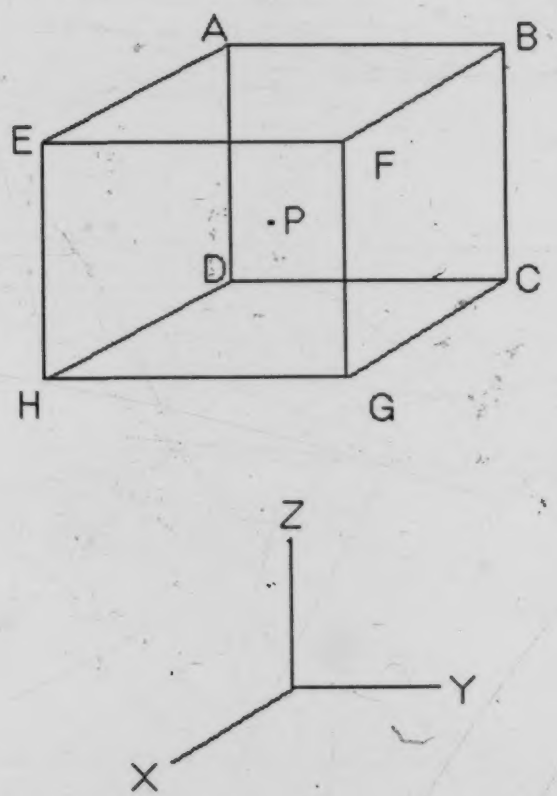

Figure 3.1: Heat Flux in a Fluid

(3.4), and one out of the cube at surface EFGH (3.5):

$$[heat(in)]_x = (\dot{Q}_x - \frac{\partial \dot{Q}_x}{\partial x} dx) 4 dy dz \delta t \tag{3.4}$$

$$[heat(out)]_x = (\dot{Q}_x + \frac{\partial \dot{Q}_x}{\partial x} dx) 4 dy dz \delta t \tag{3.5}$$

where $\dot{Q}_x$ $(\frac{W}{m^2})$ is the time-independent heat flow at point 'P' in the x-direction, and δt is a small time interval. Consequently, the net heat gain by the cube is the difference between (3.4) and (3.5):

$$[net(in)]_x = -8 \frac{\partial \dot{Q}_x}{\partial x} dx dy dz \delta t. \tag{3.6}$$

More generally, in 3 dimensions, this becomes:

$$[net(in)] = -8 dx dy dz \delta t \nabla \cdot \dot{Q}. \tag{3.7}$$

But we can also express the heat gain thermodynamically in terms of the temperature rise since the Net Heat(in) = (Mass) x (Sp. Heat)$_p$ x δT:

$$[net(in)] = \rho 8 dx dy dz C_p \delta T. \tag{3.8}$$

By equating (3.7) and (3.8) we arrive at the Equation of (thermal) Continuity,

$$\nabla \cdot \dot{Q} + \rho C_p \frac{\partial T}{\partial t} = 0 \tag{3.9}$$

and, by substituting (3.3) into (3.9) and taking a differentially small time interval δt, we arrive at the thermal diffusion equation:

$$\nabla^2 T - \frac{\rho C_p}{\lambda}\frac{\partial T}{\partial t} = 0. \tag{3.10}$$

Assuming elimination of intrinsic heat sources and sinks in the fluid, the question can be examined via two distinct routes. The first would be to set up 'steady-state' experimental conditions, such that:

$$\frac{\partial T}{\partial t} = 0. \tag{3.11}$$

We would then be left with Laplace's equation for the temperature field:

$$\nabla^2 T = 0. \tag{3.12}$$

Alternatively, a 'dynamic' experiment could be performed, allowing spatiotemporal variation of the fluid temperature. A thorough theoretical treatment of both cases for many geometries is to be found in Carslaw and Jaeger [29].

Since we have a steady state experiment, we consider equation (3.12), expressed in cylindrical coordinates:

$$\frac{\partial^2 T}{\partial r^2} + \frac{1}{r}\frac{\partial T}{\partial r} + \frac{1}{r^2}\frac{\partial^2 T}{\partial \theta^2} + \frac{\partial^2 T}{\partial z^2} = 0 \tag{3.13}$$

We assume that the design will allow the following simplifying conditions:

$$\frac{\partial T}{\partial z} = \frac{\partial T}{\partial \theta} = 0 \tag{3.14}$$

i.e., longitudinal and angular temperature dependence are zero. This would be the case only for infinitely long cylinders; this unrealisable requirement can be simulated in the apparatus. Laplace's equation thus reduces to:

$$\frac{\partial^2 T}{\partial r^2} + \frac{1}{r}\frac{\partial T}{\partial r} = 0, \tag{3.15}$$

and applies to the sample medium confined within the gap, with the 'inner' and 'outer' cylinders as the isothermal boundaries to the sample. During the experiment, the inner cylinder is heated, and heat flow is from 'inner' to 'outer' across the gap.

Then, with additional boundary conditions: (1) $T = T_1$ at $r = r_1$ isothermal surface of inner cylinder, and (2) $T = T_2$ at $r = r_2$ isothermal surface of outer cylinder, the general solution of (3.15):

$$T(r) = C_1 \ln r + C_2 \tag{3.16}$$

gives rise to the particular solution:

$$T(r) = \frac{(T_1 - T_2)\ln r}{\ln \frac{r_1}{r_2}} + \frac{T_2 \ln r_1 - T_1 \ln r_2}{\ln \frac{r_1}{r_2}}. \tag{3.17}$$

Applying boundary conditions (3.14) in the case of the Fourier equation (3.3) in cylindrical coordinates, we have:

$$\dot{Q}(r) = -\lambda \frac{\partial T(r)}{\partial r} \tag{3.18}$$

and, making the substitution (3.18) into (3.19), have:

$$\dot{Q}(r) = \lambda \left(\frac{T_1 - T_2}{\ln \frac{r_2}{r_1}}\right) \frac{1}{r}. \tag{3.19}$$

This expresses the heat flux, $\dot{Q}$ $(\frac{W}{m^2})$, as a function of radial distance from the central axis. The total heat (power), $Q(W)$, transmitted radially from the inner cylinder of length l is simply the area of the inner cylinder times the flux at that radius $(\dot{Q}(r_1))$:

$$Q = 2\pi l r_1 \dot{Q}(r_1) = 2\pi l \lambda \left(\frac{T_1 - T_2}{\ln \frac{r_2}{r_1}}\right). \tag{3.20}$$

Equation (3.20) is the basic defining equation for the steady state experiment (applying to concentric, coaxial cylinders). It relates the power $(Q(W))$ delivered by the (heated) inner cylinder to the temperature difference between the cylinders $(T_1 > T_2)$.

Rewritten, (3.20) becomes a formula for the thermal conductivity:

$$\lambda = Q\left(\frac{\ln(\frac{r_2}{r_1})}{2\pi l}\right) \frac{1}{(T_1 - T_2)}. \tag{3.21}$$

Geometric quantities can be regrouped into a single constant term, giving rise to the simplified form:

$$\lambda = \frac{QK_1}{\Delta T}. \tag{3.22}$$

In summary, the steady state type of experiment involves just the measurement of Q (heater power) and temperature difference (ΔT). Corrections terms added in the final analysis will be discussed in section 3.4.2.

3.3 Details of Apparatus

3.3.1 External High Pressure Cell

The requirements of the cell body were: (a) high strength, (b) good thermal conductivity, (c) cylindrical symmetry, (d) large thermal mass (acts as a heat sink), and (e) sufficient internal working volume. Beryllium copper alloy was selected as the material for the cell owing to its relatively high tensile strength and thermal conductivity compared to stainless steel [30]. A schematic diagram of the cell is shown in Figure 3.2.

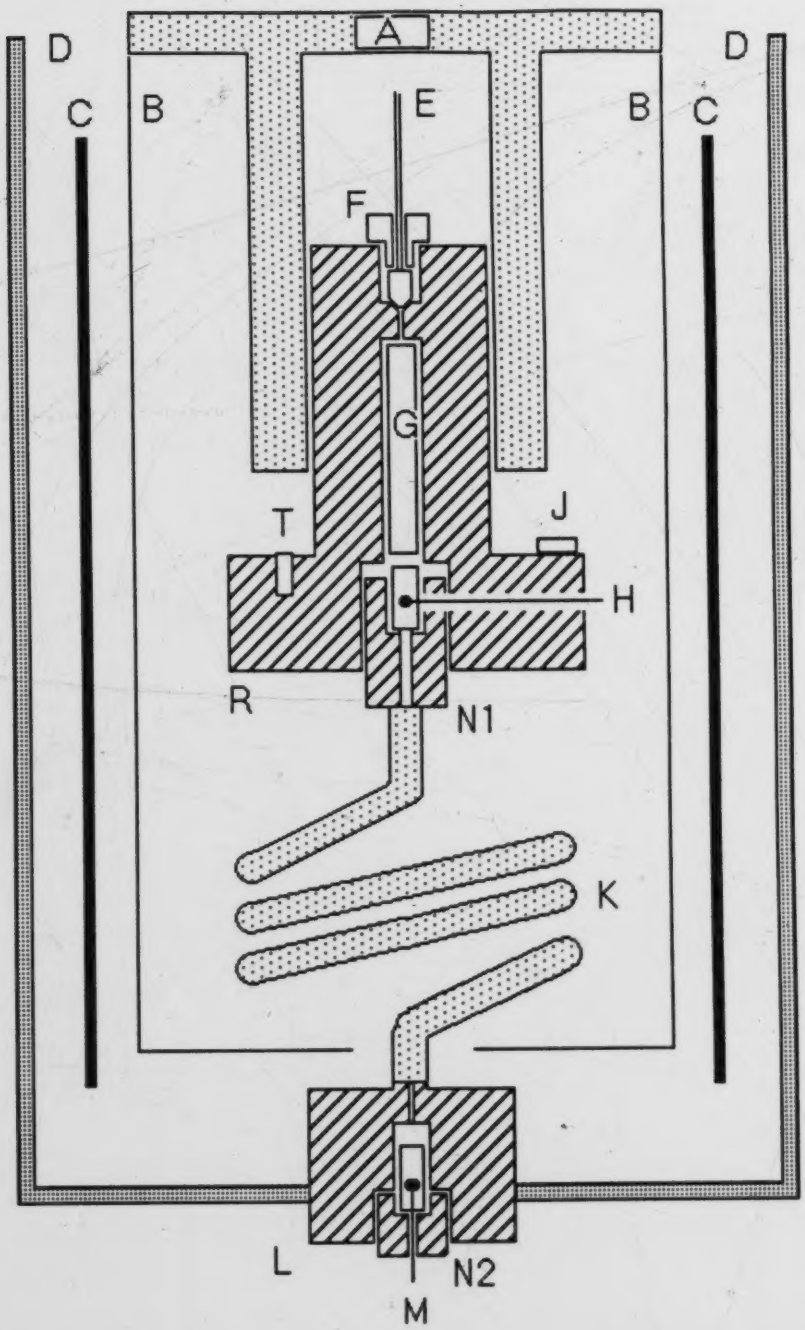

Figure 3.2: Schematic Diagram of Experimental Arrangement.

A OFC cold finger attachment on liquid helium dewar (clamps cell)

B Radiation shield near cell temperature

C Radiation shield at liquid nitrogen temperature (77 K)

D External vacuum can arrangement

E High pressure capillary

F Compression nut

G Concentric cylinder arrangement

H BeCu plug (seals to cell body, **R**)

J Auxiliary thermometer

K Harwood 3M high pressure conduit containing lead-in wires

L Feedthrough block (at room temperature)

M Electrical feedthrough

N1, N2 Compression nut

R BeCu cell body

T Calibrated germanium thermometer

The cell (R) was machined from a single piece of Beryllium Copper ('Be-Cu 25') supplied by Brush Wellman Inc. (Brush Wellman Inc., 3516 Cadieux Rd., Detroit, 48224). After heat treatment at 325°C for 4 hours (followed by air-cooling), the cell was found to have a hardness of 42 on the Rockwell 'C' scale, and, according to the supplier's literature, should have an ultimate tensile strength of $\sim 1.3 \times 10^4 \frac{kg}{cm^2}$. The tensile strengths of most materials used in high pressure research increase with a decrease in temperature [31]. The approximate rupture pressure of tubes of given material of known ultimate tensile strength, is provided by [31]:

$$P_{rup} = \sigma \ln \alpha \tag{3.23}$$

where σ = ultimate tensile strength, $\alpha = \frac{R}{r_0}$, R = outer radius, r_0 = inner radius. This equation is based on the assumption that the entire thickness of the tube wall has gone over into the plastic state. Insertion of the appropriate numbers for the cell gave a burst pressure of $\sim$ 16.6 kbar,–a safety factor of at least eight (however, other components such as the capillary had an ultimate burst pressure of $\sim$ 6 kbar).

The cell maintained the cylindrical symmetry dictated by its internal components. The larger end of the cell provided reserve strength for the

threading of the compression nut (N1), as well as a thermal sink and a place on which to mount thermometers (T) and (J). The high pressure gas capillary (E) and the high pressure wiring conduit (K) were introduced to the cell along the central, longitudinal axis. The conduit was a stainless steel tube (Harwood 3M, 0.375" o.d. x 0.025" i.d. x 2 meter long), which conveyed the necessary wiring from the cell (at operating temperature) to the feedthrough block (L) at room temperature. The length of tubing contributed to greater thermal isolation of the cell.

The high pressure conduit to the electrical feedthrough block was hard soldered into a BeCu plug (H) which sealed to the cell body through an Indium coated soft BeCu ring. The high pressure gas capillary (E) entered at the opposite end of the cell; a standard conical fitting, into which the capillary (1/32" o.d. x 0.008" i.d.) was hard soldered, was forced into a conical seat by an external nut (F).

Also shown in Figure 3.2 are: (A) cold finger attachment (OFC) on the dewar; (B) radiation shield near cell temperature; (C) radiation shield at N_2(l) temperature; (D) external vacuum can(s); (G) concentric cylinder arrangement; (M) high pressure electrical feedthrough plug; (N2) compression nut for (M).

3.3.2 Electrical Feedthrough

To construct a satisfactory high pressure electrical feedthrough connecting the internal heater and thermometers to external instruments was a primary engineering goal of this project. The measuring system required a minimum of 6-8 wires: 2 for the differential thermocouple, up to 4 current lead-in wires for the internal heater, and 2 voltage lead-in wires for the internal heater.

Several feedthrough types were tried but were found to be wholly or partially deficient. A new type had to be developed for this project to provide a high pressure seal for helium to 2 kbar with repeated cycling. The requirement for thermal cycling between 300 K and 4 K was found to be the most challenging criterion. A schematic diagram of the final design is shown in Figure 3.3.

Feedthrough designs which failed included the "pressed pyrophillite cone" and the "epoxy-filled well". Rather than enter a detailed discussion of these methods, only a brief description of each and their failure mode will be presented. In the former, wires were embedded in a conical layer of pyrophillite powder which, when subjected to 200 bar pressure, became transformed into a ceramic-like seal.

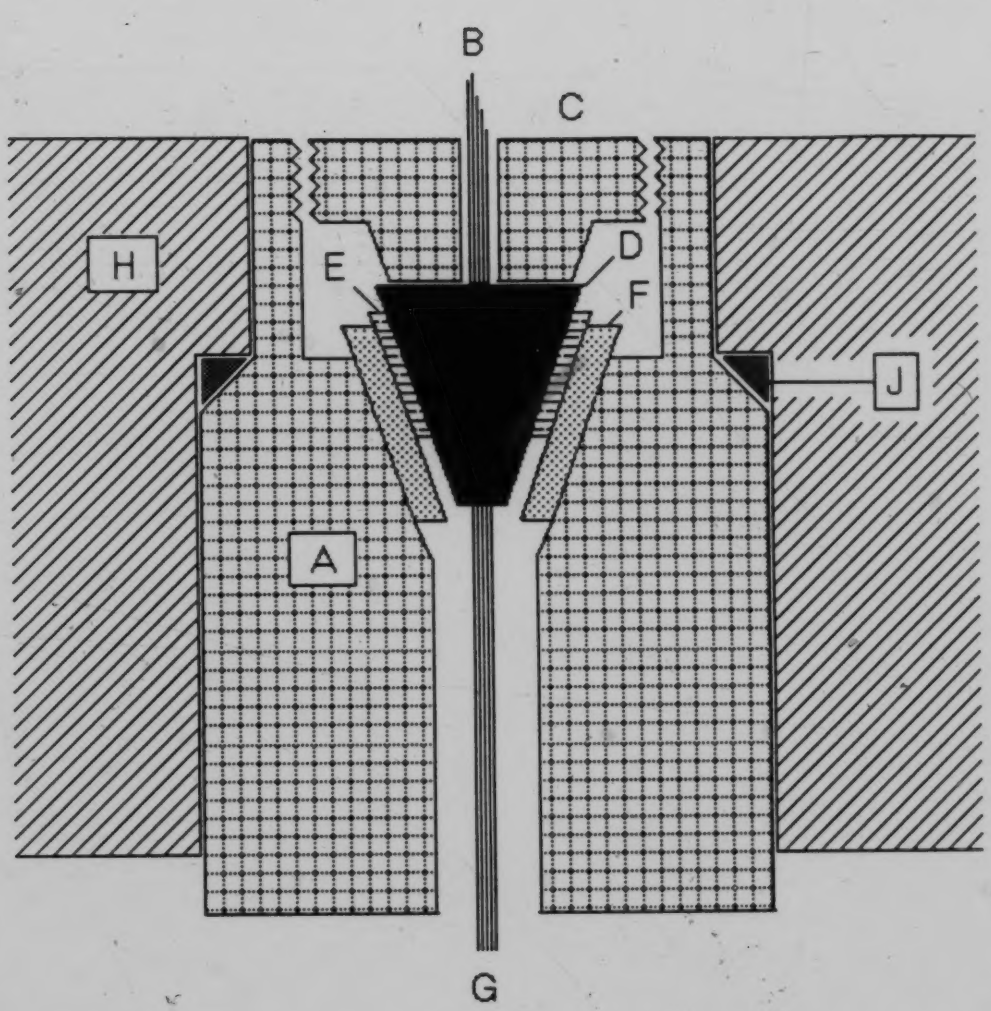

Figure 3.3: Schematic Diagram of the Electrical Feedthrough

A Feedthrough plug (hardened BeCu)

B Wire bundle (internal)

C Energising compression nut

D Molded epoxy cone containing wire bundle

E Teflon Tape layer

F Vespel conical shell

G Wire bundle (external)

H Body of feedthrough block

J BeCu sealing ring (coated with Indium)

Extreme care had to be taken either (a) to avoid pinching off the wires while pressing the layer, or (b) to insufficiently press the layer, leading to leaks. The other design consisted of a metal plug with a central hole containing the wire bundle and epoxy. Both designs worked well at room temperature but would begin to leak as the cell temperature was lowered, owing to differential elastic deformations of the various components or to formation of fine cracks in the epoxy. Since the cell was maintained in high vacuum, such leaks were intolerable.

In view of these deficiencies, a new approach had to be taken. This involved two parts: (a) a multi-wire feedthrough to withstand repeated pressurisation, and (b) removal of the feedthrough from the region of low temperature. It became apparent that leaks due to deformation of feedthrough components through differential thermal contractions (or crack formation) could not be easily overcome; placing the feedthrough outside of the cryostat and maintaining it at room temperature, with a high pressure tube (conduit) connecting to the cell, could entirely avoid this problem. The only drawback introduced by this design was a heat leak to the cell. The feedthrough plug (Figure 3.2, (M)) was held by compression nut (N2) in a hardened BeCu block (L); the plug seal consisted of an Indium coated soft BeCu ring.

After several stages of evolution, the following design was developed (Figure 3.3). The feedthrough consisted of five components: wire bundle (up to 16 #42 AWG Copper wires) (B)-(G), molded Stycast 2850 epoxy cone (D), Teflon Tape layer (E), Vespel (SP - 1) conical shell (F), and hardened BeCu plug (housing the above components) (A). The conical aperture in the plug, Vespel shell, and the molded epoxy cone all have the same half-angle of 7.5^0. Vespel is an extremely durable polyamide plastic material that is easily machined to a fine tolerance; being highly elastic compared to the hardened BeCu components, the Vespel shell and Teflon Tape layer provided the essential compliance to pressure variations during the course of the experiment.

The feedthrough was constructed as follows. First, the wires were strung individually on a simple wooden frame and a short portion ($\sim$ 2 mm) of the varnish chemically removed near one end. These exposed portions were cleaned with methanol, then coated with a thin layer of degassed Stycast 2850. The epoxy was permitted to harden for 24 hours. Individual coating of wires insured a better epoxy-metal bond and eliminated leakage underneath the varnish.

Next, the wires were cut to length and soldered together at each end so that the coated sections were located side by side. The bundle was passed

through a brass mold (not shown, but similiar in size and shape to (A), the plug) having a conical aperture of half-angle of 7.5^0 and of the same depth as the Vespel shell. The aperture had been polished using wooden tools and commercial polishing compounds (alumina, United States Products Co.), then coated with mold-release. The wire bundle was pulled through the mold until the coated sections were about half-way through the aperture. A fresh mixture of degassed Stycast 2850 was prepared and injected into the mold by hypodermic needle, insuring that no air bubbles were trapped and that the epoxy completely wetted all surfaces in the bundle. After centering the bundle in the mold, the epoxy was permitted to harden at room temperature for at least 24 hours.

By briefly warming the brass mold with a hot-air gun (to 150^0 C.) and pulling gently on the wires, the bundle imbedded in a Stycast cone was extracted. Cleaning and inspection for defects were then performed.

The Teflon Tape layer was prepared by winding a strip of ordinary sealant tape (1 mm x 10 cm) tightly with 50% overlap onto the end of a tapered steel rod (half-angle = 7.5^0) that had been coated with mold-release. The wrapped rod was then hand-forced with rotation into the brass mold until the Teflon layer had become uniformly mashed into a single semi-transparent

piece. This intact layer was removed from the steel rod and carefully placed over the Stycast cone.

The aperture in the plug (A) was polished and tinned with Indium. The Vespel conical shell was inserted loosely into this aperture, followed by threading of the wire bundle through it until the Stycast cone came into contact with the Vespel. The compression nut (C) was carefully installed, and, with a special tool, screwed down until the Stycast cone was firmly seated.

The BeCu feedthrough block (Figure 3.2, (L)) which always remained at room temperature during the experiment, had been hard soldered to a 2 meter length of straight Harwood 3M tubing, at the other end of which a special BeCu (H) plug had been hard soldered which eventually sealed at the cell. The wire bundle was fed into the block and pulled through the 3M tube, using a length of piano wire. The feedthrough plug (Figure 3.2, (M)) at the same time was installed in the block and seated with closure nut (N2). The measuring unit, consisting of the concentric cylinders, was mounted onto the BeCu plug, the necessary wiring connections made, and the plug was inserted into the cell and seated firmly by the external closure nut (N1). The 3M tube was wound into a 5 cm. dia. coil (about 30 cm in

length overall) in order to fit within the vacuum can.

3.3.3 Concentric Cylinders

The measuring system consisted of a pair of cylinders: cylinder No. 1 (Figure 3.4, (J)), the 'emitting' or inner cylinder (5.994 mm dia. x 17.526 mm long), made of solid BeCu except for a central longitudinal hole which carried an electric heater; cylinder No. 2 (M), the 'receiving' or outer cylinder (6.198 mm bore x 31.013 mm long), also made of BeCu, was hollow and accepted cylinder No. 1 within the bore with a fixed gap of 102μm (L). The dimensions of the various BeCu cylinder components were measured at room temperature with an electronic vernier caliper accurate to within $\pm$ 0.0001 inch, or $\pm$ 0.002 mm; the dimensions reported here are therefore precise to within 2 μm. The opposing faces of the inner and outer cylinders were polished to a mirror finish using a commercial lapping compound (partical size: 1 micron). The unusually small gap, enclosing a small volume of fluid, had several advantages. The system reached a quasi-steady state rapidly, facilitating measurements. The temperature differences were always very small ($\sim$ 100mK or less) which meant that the value of thermal conductivity was

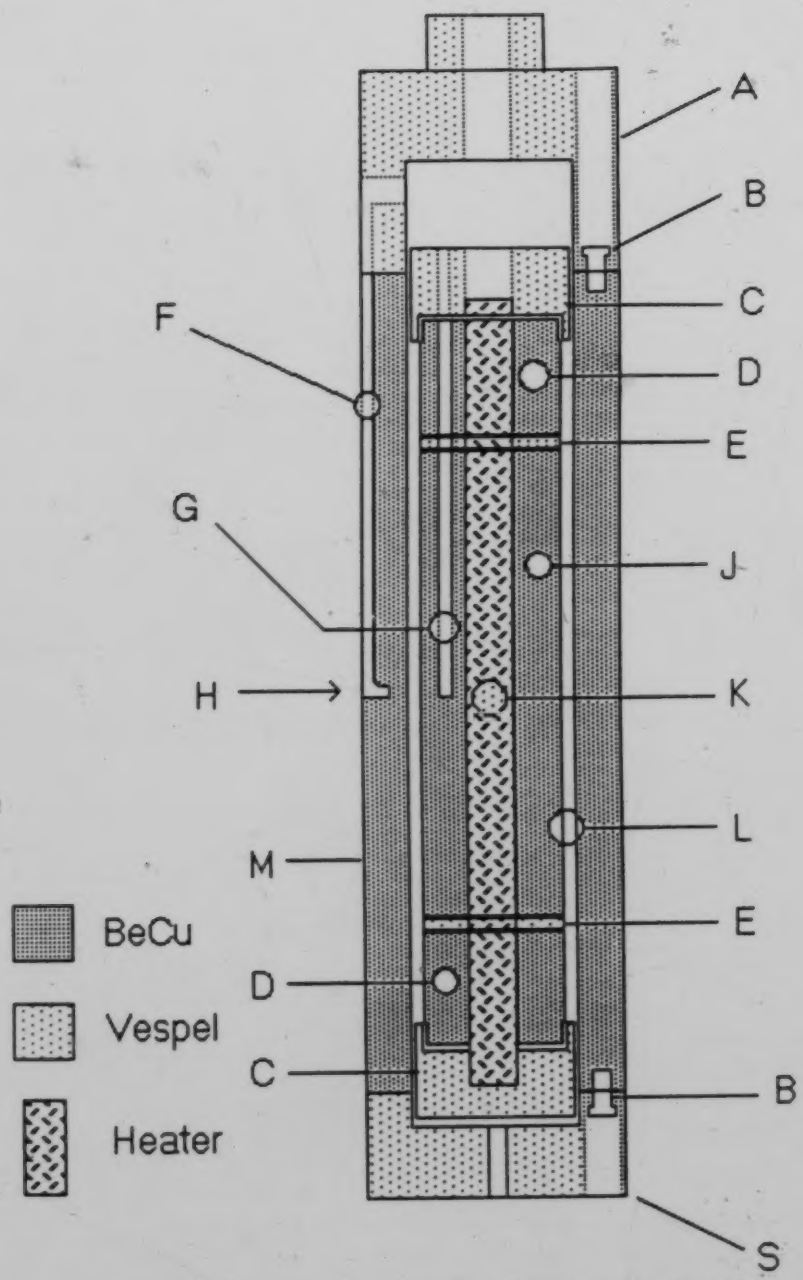

Figure 3.4: Schematic Diagram of the Concentric Cylinders

A Vespel end cap

B Screw

C Vespel alignment piece

D Guard cylinder

E Vespel spacer

F Thermocouple channel (T_2)

G Thermocouple well (T_1)

H Thermocouple location

J Inner cylinder

K Internal heater

L Annular gap

M Outer cylinder

S Vespel end cap

well defined, and lower heater power could be used at lower temperatures. The purpose of the small gap was to ensure that convection was strongly inhibited in the apparatus. According to fluid mechanics theory, the onset of convection in a fluid is likely if the dimensionless Rayleigh Number, R_a, exceeds some critical value, R_c.

R_a has the following form, being itself the product of two hydrodynamic parameters, the Grashof Number and the Prandtl Number:

$$R_a = GrPr = \left[\frac{d^3\rho^2\alpha_p\Delta Tg}{\eta^2}\right]\left[\frac{\eta c_p}{\lambda}\right] \tag{3.24}$$

$$= \left[\frac{\rho^2\alpha_p g d^3\Delta T}{\eta D}\right] \tag{3.25}$$

where η is the shear viscosity, c_p is the specific heat, λ is the thermal conductivity, d is a relevant cell dimension (for concentric cylinders, it is the gap), ρ is the fluid density, D is the thermal diffusivity, α_p is the coefficient of thermal expansion, ΔT is the temperature difference between layers, g is the gravitational acceleration.

Substitution of the appropriate term values from numerous published sources [56][60], gives $R_a \simeq 0.04$ at T = 20.5 K, P = 1.841 kbar, ΔT = 0.1 K, and d = 0.01 cm. The critical Rayleigh number for helium confined within a horizontal parallel plate Rayleigh-Bénard cell has recently been calculated

[58], giving $R_c = 1708$, which is five orders of magnitude larger than R_a, indicating that convection was extremely unlikely in the annular gap.

The heater (K), contained within a stainless steel tube, was substantially longer than the inner cylinder; the additional length of the heater carried a pair of 'guard cylinders' (D),- one at either end of the inner cylinder (J) and separated from it by a Vespel spacer (E). The entire arrangement was capped at each end by a Vespel 'alignment piece' (C) which fit snugly into the hollow bore of the outer cylinder, ensuring concentric alignment and uniform gap. Each end of the outer cylinder was fitted with a Vespel 'end cap' (A) and (S), and held together with screws (B).

There were two channels machined into the inner and outer cylinders in which the separate differential thermocouple sensors were located. A groove (F), terminating in a small well (H) which penetrated halfway into the thickness of the outer cylinder, carried one sensor at T_2; a small hole drilled into the inner cylinder (G) provided the location for the other sensor at T_1 ($T_1 \geq T_2$). The holes were filled with a mixture of Apiezon N grease and copper powder to improve thermal contact between thermocouples and the cylinders.

The heater consisted of a $\frac{1}{32}$" steel drill rod former which was covered with an equivalent length of heat shrinkable rubber tubing. A 175 Ω Manganin wire was wound in bifilar fashion over the rubber tubing and sealed with G.E. 7031 varnish, then coated with a layer of vacuum grease mixed with copper powder. The heater was installed inside the stainless steel tube, which then provided a linear structural mount for the inner cylinder, guard cylinders, spacers and alignment pieces.

During experimental trials, a current was passed through the Manganin wire and the resulting heat flowed radially outward through the stainless steel tube to the inner cylinder and guard cylinders. The basis of this method is that a substantive portion of heat generated in the inner cylinder should flow radially across the fluid-filled gap to outer cylinder. Heat may 'escape' from the ends of the inner cylinder, but this is reduced significantly by presence of the Vespel spacers, which have a relatively low thermal conductivity; furthermore, heat which does cross the Vespel spacers is replaced by heat from the heated guard cylinders flowing in the opposite direction. Only that portion of the total heat generated by the heater which flows into the inner cylinder is counted in the calculation of the thermal conductivity; since the inner cylinder covers 56.48% of the total length of the heater, this is the fraction

of total power which was used in the calculation of λ (refer to section 3.5.3 for further discussion on this point).

3.3.4 Thermocouples

It has been shown [32] that the combination of Au + 0.07% Fe vs. Chromel has the highest thermoelectric power over the temperature range of interest in this project. Wires of these types were obtained from the Sigmund Cohn Co. (distributor: Leico Industries Inc., 250 W. 57 St., N.Y., N.Y. 10107) and thermocouples were made according to the following procedure. Refer to Figure 3.5.

A thermocouple is formed where two different metals are chemically joined, or fused. In this case, the wires (0.003" dia.) were melted together by passing an electric current through them. First, the dissimiliar wires were each cut to the necessary length and stripped of their Teflon insulation at the ends (a stereo microscope was indispensible for this and other tasks). The exposed segments of the wires were held together side by side between two copper alligator clips separated by 5mm. The alligator clips were electrically insulated from each other and connected through an open switch to a Variac

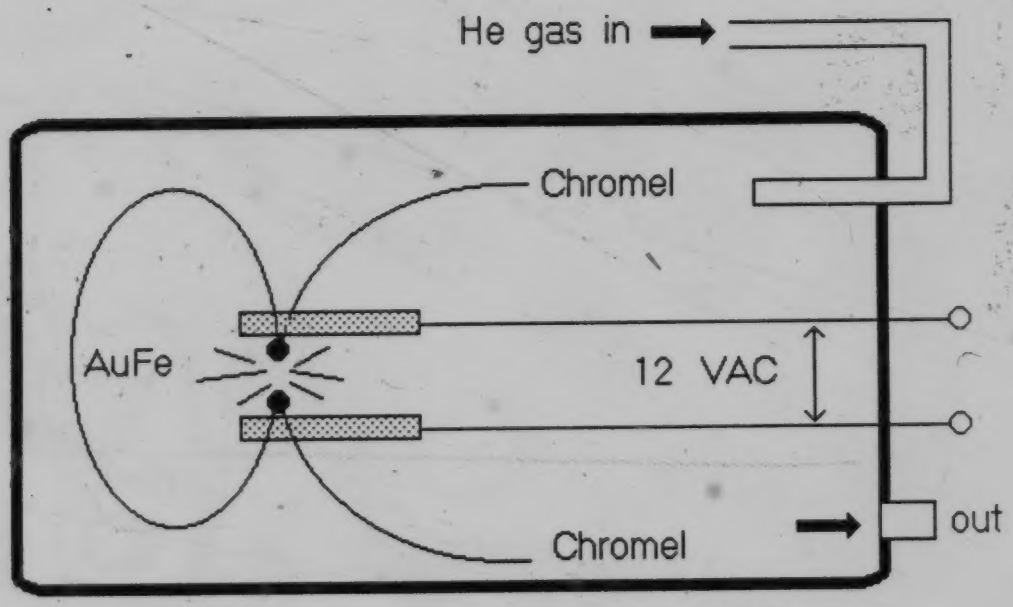

Figure 3.5: Manufacture of Thermocouples

set at 12 VAC. The alligator clip arrangement was then installed inside a glass tube and helium gas passed through it for several minutes in order to reduce oxidation contamination. When the switch was closed, current flowed through the circuit which included a path across the parallel Chromel and AuFe wires. This voltage was sufficient to suddenly melt the wires and fuse them. The reproducibility of these trials was not very high, so it was found necessary to include extra length in case the wires failed to fuse together, or did so poorly. Since a temperature difference was measured, a differential pair of thermocouples was made having a common central element of AuFe; the voltage between the outer elements (Chromel) was proportional to ΔT.

Calibration of the thermocouples was not deemed necessary, since the added effort would not be rewarded with any substantial improvement in the overall precision of the experiment (other factors, such as Q, being subject to relatively large uncertainty). The thermoelectric power of the Chromel vs. AuFe pair was derived from published sources [32], which provide a 14-order polynomial equation in temperature for a generic thermocouple of this type. The effect of pressure on thermoelectric power [33] is probably very small in the range of pressures in use in this experiment, and could safely be ignored. For example, Bartholin [34] has shown that the thermoelectric

power of a copper-constantan thermocouple decreased linearly by only 0.25% when subjected to pressures up to 3 kbar.

3.3.5 Cryostat and High Pressure System

A controlled temperature dewar (International Cryogenics Inc., model 31-4000) with 'optical tail' was modified for this experiment. The high pressure cell was attached to the Swenson temperature-control block with the conduit to the feedthrough block suspended vertically down; a pair of radiation shields at liquid nitrogen and helium temperatures enclosed the cell, and the whole arrangement was encased in a vacuum can. A backing pump and oil diffusion pump maintained a vacuum pressure at or below 10^{-7} Torr during experiments.

Helium gas was conveyed to the cell via a stainless steel capillary ($\frac{1}{32}$" o.d. x 0.008" i.d.) from the high pressure section. Purified helium gas ("Matheson purity" 99.9999% He, containing less than 1 ppm in total of N_2, O_2, Ar, CO, CO_2, THC as CH_4, and H_2O) from the supply bottle (Figure 3.6, (E)) passed through a filtre (Messer Griesheim, HD absorber) (G) and cold trap (F) before entering the low-pressure side of a two-stage diaphragm

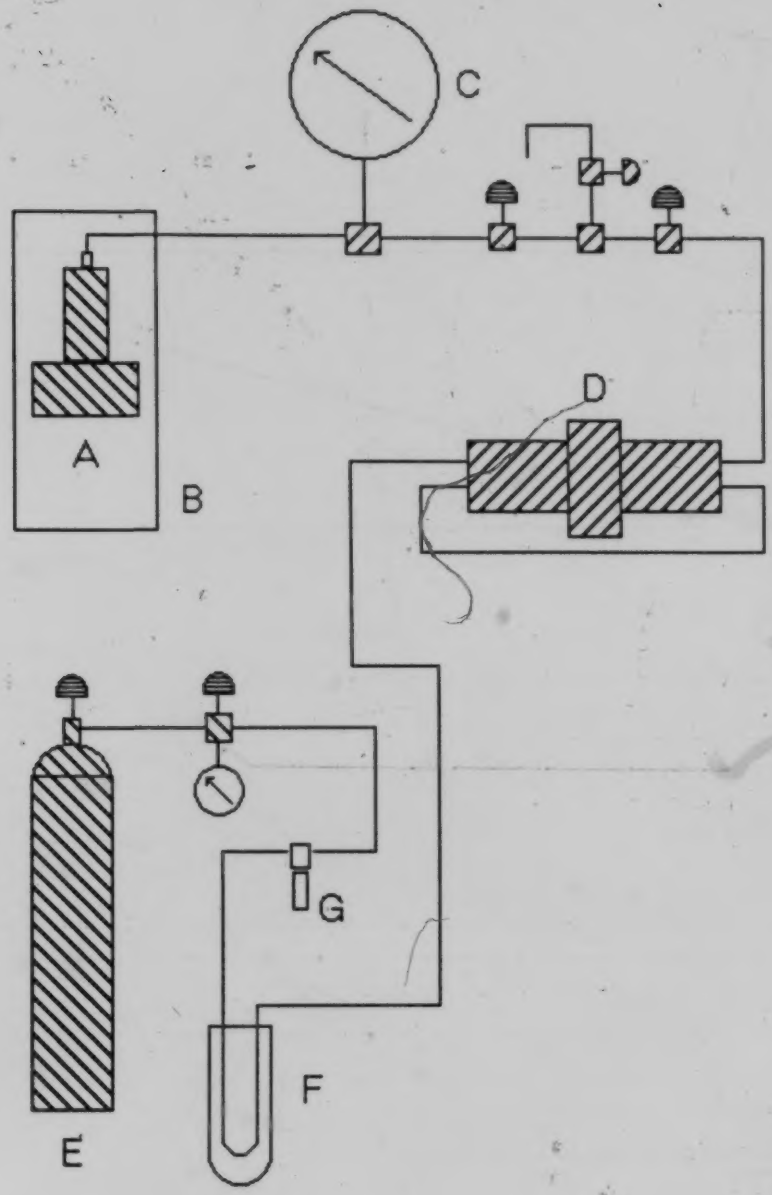

Figure 3.6: High Pressure System

compressor (American Instrument Co., catalog 46-14021, 2 kbar max.) (D); the high pressure side led to a Heise 100,000 psi Bourdon gauge (C) before leading to the capillary and cell (A). Use of small diameter capillary reduced the heat leak to the cell.

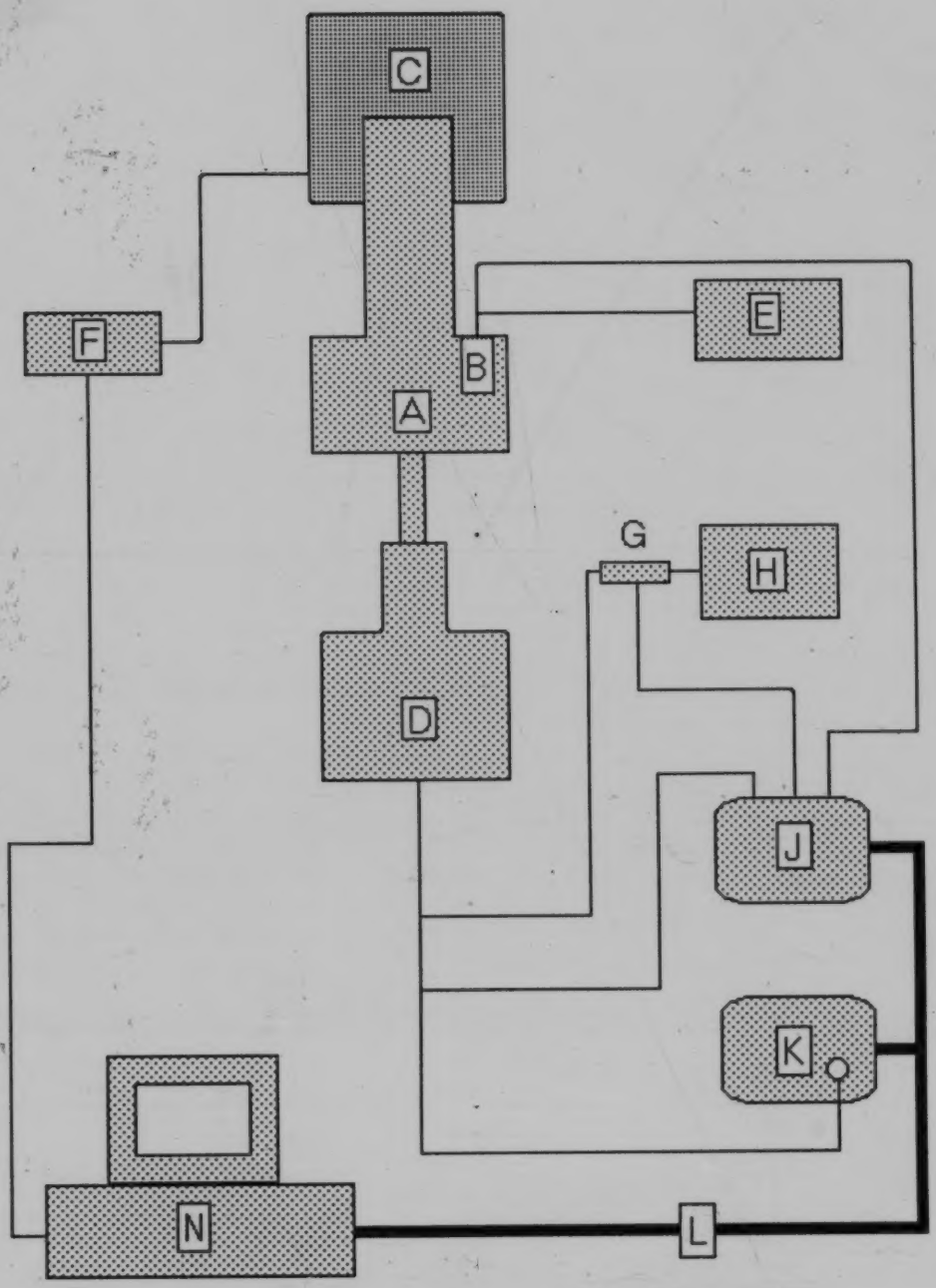

Figure 3.7: Schematic Diagram of Complete System

A High pressure cell containing concentric cylinders measuring system

B Calibrated Germanium thermometer

C Cryostat equipped with Swenson cooler (liquid helium evapourator) and electric heater

D High pressure electical feedthrough block connected to cell A by 2 meter length of Harwood 3M conduit containing lead-in wires

E Lakeshore Model 120 constant current source for the thermometer

F Computer controlled power supply for the cell heater

G Stable resistor (9.978 Ω)

H 24 VDC power supply for inner cylinder heater

J Keithley Model 199 DMM with 8 channel Scanner

K Keithley Model 181 Nanovoltmeter

L IEEE 488 GPIB

N Zenith Data Systems microcomputer

3.4 Experimental Method

3.4.1 Details of Method

At the beginning of a trial, the cell was flushed with Helium four times to $\geq$4000 psi, thereby diluting entrapped contamination (water vapour, air, etc.) by a factor of about 10^9. The maximum desired working pressure was then developed in the cell, using the diaphragm compressor to 2 kbar. Next, the cryostat was evacuated and filled with cryogenic liquids to commence cell cool-down. Between 300 K and approximately 30 K, no attempt was made to regulate the cell temperature other than merely allowing it to drift steadily down in accordance with the evapouration rate of cryogenic liquids in the Swenson block. Below about 30 K, a combination of the evapouration rate and a controlled heating rate, using a custom-built computer controlled power supply, was used to hold the cell at fixed temperatures (within $\pm$ 10 mK). Primary readings of cell temperature were obtained from a Germanium resistance sensor (Lakeshore Cryotronics Inc., model GR-200B-2500) (Figure 3.2, (T)), calibrated by the supplier against maintained standards (0.5 to 30 K, EPT-76; $\geq$30 K, IPTS-68). A Lakeshore Cryotronics stable current supply (model 120 Current Source) delivered a regulated current through the

sensor, and the IR drop was measured with a Keithley Model 199 DMM. The resulting temperature was calculated using Chebychev polynomial coefficients supplied by the manufacturer, and could be read to within ±1 mK. However, ever present cell thermal fluctuations and noise in the DMM led to apparent fluctuations of about ± 40 mK near 77 K, and about ±5 mK near 10 K.

At a fixed cell pressure, readings were obtained during cool down for the fluid phase starting at about 80 K. The cooling rate was determined by controlling the evapouration of liquid helium through the Swenson block. This was accomplished with a network of vernier needle valves (E) (Figure 3.8) and flow gauges (F) located between the Swenson block and the laboratory helium gas recovery system (G). An adjustable pressure regulator (D) maintained constant boil-off of the liquid helium. Interest was focussed on the region below 77 K (LN_2), since an uninterrupted run to 7 K could be made using liquid helium as the cryogen. The high sensitivity of the thermocouples made temperature regulation extremely problematic, slow, and expensive (high consumption of liquid helium cryogen). The inherent thermal lag of the massive cell, and automatic heater current fluctuations, resulted in erratic swings in the thermocouple voltage with long settling times. There-

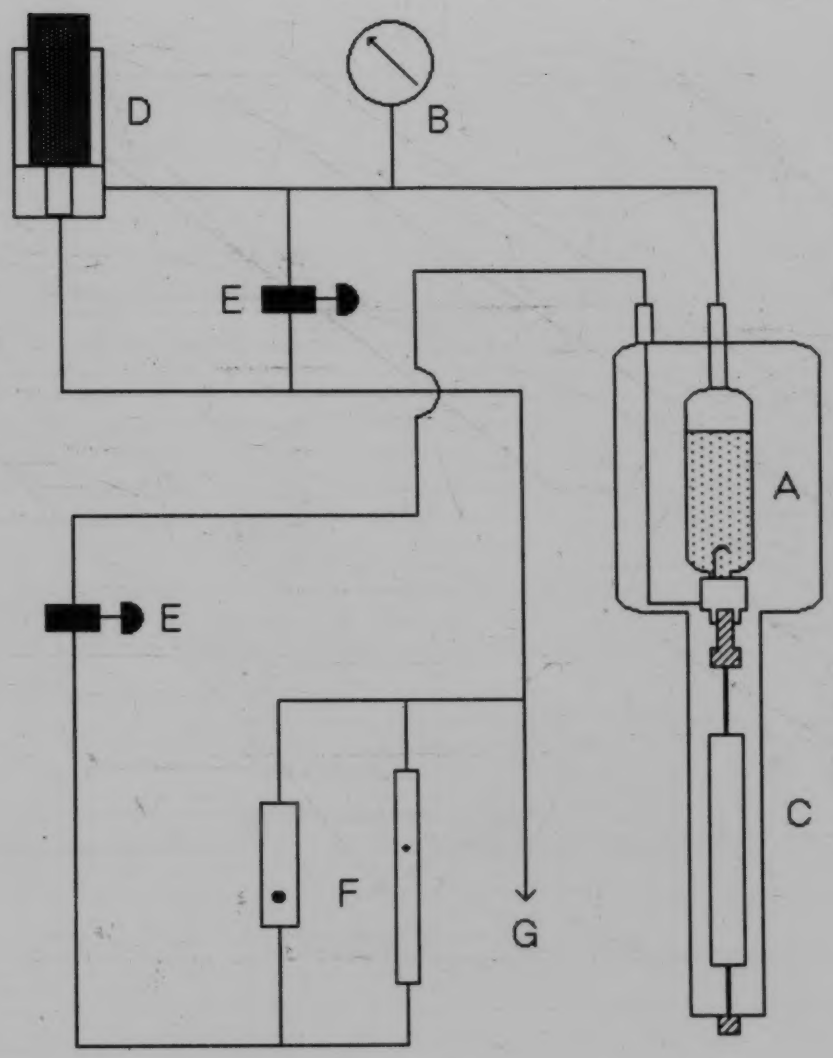

Figure 3.8: Pressure and Boil-off Control for the Cryostat

fore, attempts to deliberately control cell temperature using a commercial controller were abandoned, and data were obtained as the cell slowly cooled. By keeping the cooling rate low, and making the reading time short, temperature drift during individual data collection was kept quite small, typically ± 50 mK or less.

Although the aim of the method was to establish steady state conditons, this was virtually impossible for the fluid phase measurements for reasons just given. It was necessary to take advantage of the opportunities which the given situation offered, even if these were less than 'ideal'. The measuring system never reached a true steady state in terms of temperature, but a constant rate of change of temperature of the cell was easily managed. As the cell cooled, the thermocouple voltage signal always registered a non-zero value, reflecting the fact that the inner cylinder was a little warmer than the outer cylinder, since it was insulated from the outer cylinder by the fluid helium layer. (The outer cylinder was assumed to be in good thermal contact with the pressure cell body, whose absolute temperature was recorded.) As long as the cooling rate was constant, the thermocouple voltage signal remained constant, and was in fact used as an indicator in a manual feedback effort to maintain a stable cooling rate. This voltage was recorded as the initial 'zero'

reading prior to each datum. The thermocouple voltage also included some small thermoelectic signals (typically, $\leq$ 200 nV $\pm$ 30 nV), likely generated in two pairs of soldered connections (Cu-Chromel, and Cu-Cu) leading from the cell to the digital nanovoltmeter (Figure 3.9). Such values were treated as a subractable "bias" and zeroed out mathematically in each trial.

A custom QuickBasic program was written by the author to collect, collate and analyse all data. This ensured that human subjectivity was eliminated from the acquisition routine. Voltages read by the Keithley nanovoltmeter and the DMM Scanner were input to a Zenith personal microcomputer (equivalent to IBM PS/2) via an IEEE 488 GBIP cable. The system enabled three readings per second of cell temperature, thermocouple voltage, and heater power. The program also automatically controlled the heater at the lower tempertures.

Each data point was collected in a three-phase routine:

Initial zero The equilibrium thermocouple voltage (heater off) was recorded for 2 minutes (150 readings).

Reading The thermocouple voltage was recorded (heater on) for a predetermined length of time (minimum of 1 minute, or 50 -300 readings).

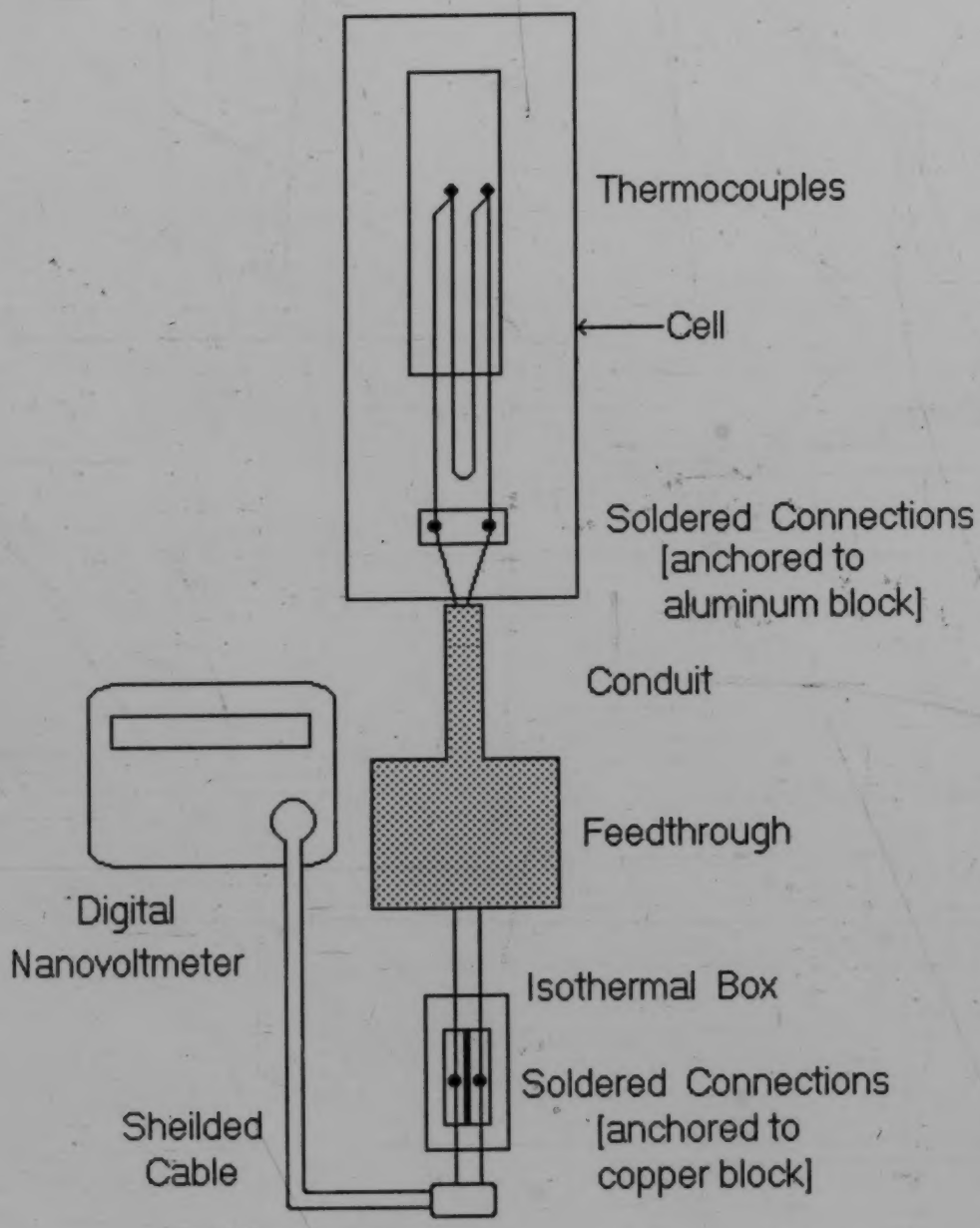

Figure 3.9: Wiring Circuit for Thermocouples

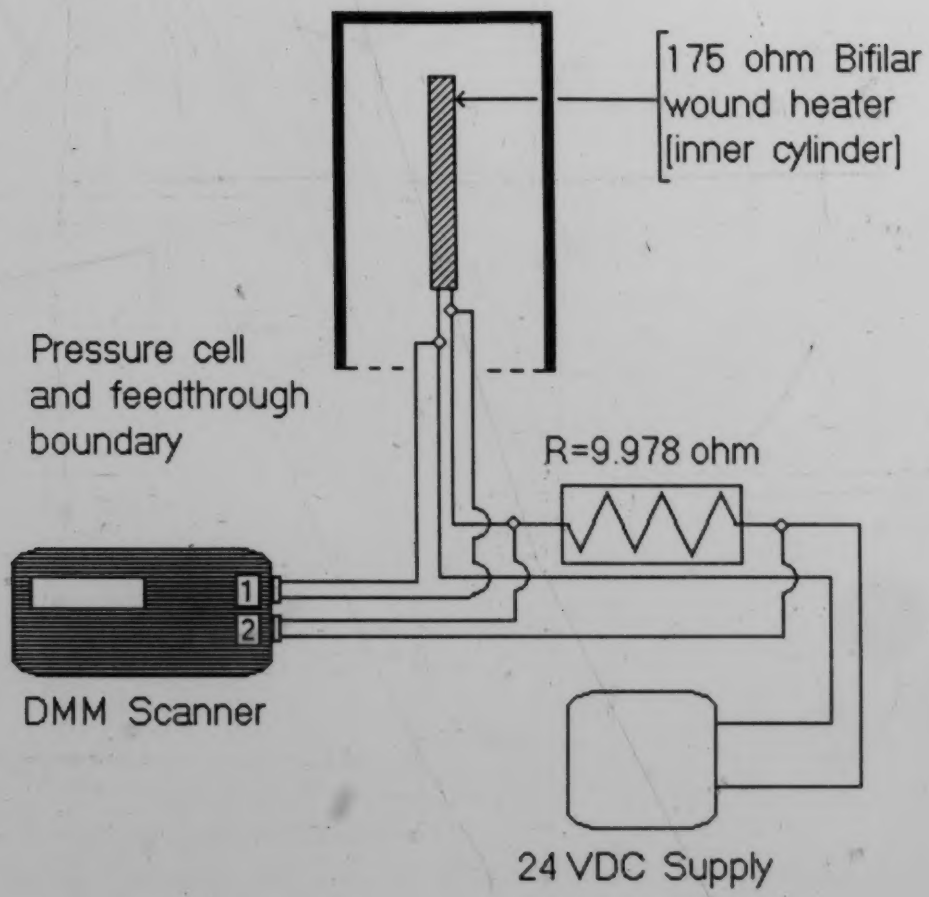

Figure 3.10: Wiring Circuit for Inner Cylinder Heater

Final zero The equilibrium thermocouple voltage (heater off) was recorded for 3 minutes (250 readings).

When the heater was switched on, there followed an immediate jump in the thermocouple voltage readings, since the inner cylinder became relatively 'hot' (ΔT = 50-100 mK, typically). Owing to the small sample mass (e.g., 0.0103 g at P = 1500 bar and T = 17.9 K), thermal equilibrium was achieved rapidly, on the order of 30 seconds (or less at lower temperatures). The set of heater-on readings were recorded (about 200 in total) and then the heater switched off. The voltage returned to nearly its previous 'zero' value, and the final 'zero' readings were recorded.

The readings in each phase were assumed to conform to a simple linear relationship with the time, and the program assumed that the overall readings would fit a step-like shape (Figure 3.11). Best-fit linear regression calculations were performed on the two "zero" sets, and the resulting lines were joined to the best-fit line which represented the heater-on readings. The average height of the vertical lines (lines 'A' and 'B' in Figure 3.11) corresponded to the probable average thermocouple voltage (and the temperature difference). During the entire procedure the cell continuted to cool at a more-

or-less constant rate; any deviation from constant cooling was compensated by averaging lines 'A' and 'B'.

Below about 30 K, temperature regulation was improved, due in part to the lower heat capacity of the cell. By using a computer-controlled cell heater in combination with constant effective cooling via the Swenson block, effective stabilisation was obtained; furthermore, the cell temperature was controlled in this range by varying the heater power. Data were obtained until evidence of solidification was obvious (e.g., sharp increase in thermal conductivity), then further collected as the temperature drifted to a minimum determined by the balance of heat fluxes into and out of the cell. The lowest temperature achieved was 7.50 K. The cell was cooled to this point, then the software-controlled heater brought the temperature back up to desired levels. Taking advantage of the superior thermal stability in this temperature range, the sample was tested at closer intervals and data in the vicinity of the melting line was obtained. The sample was melted and frozen in order to scan the transition region. Upon completion of the investigation of the low temperature region, the sample was warmed to 77 K, the cell pressure was reduced to a new fixed point, and the above procedure repeated.

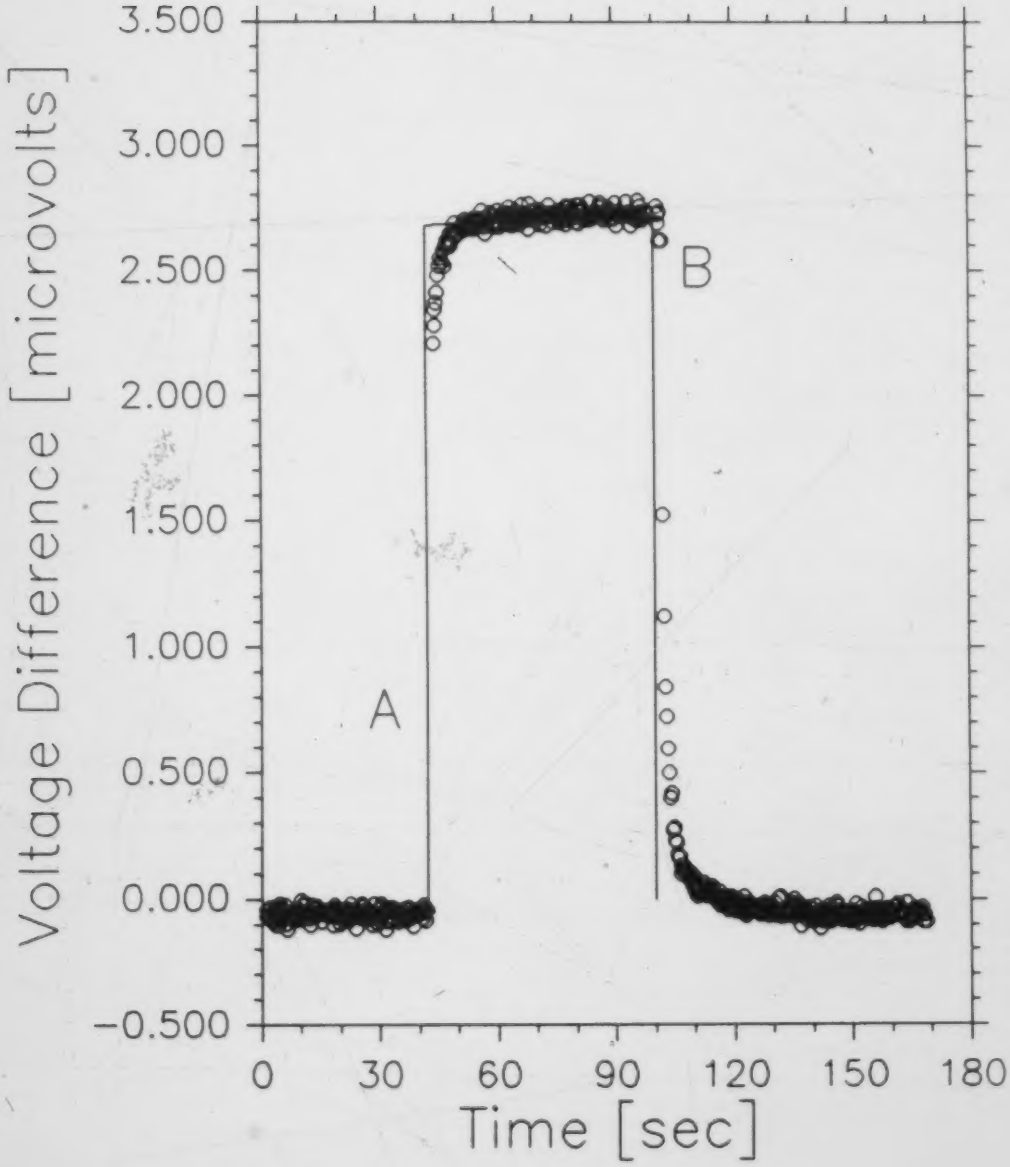

Figure 3.11: Heat Pulse in Thermocouple Voltage

3.4.2 Review of Method

The inner cylinder was heated by passing a current through the Manganin resistance winding. A regulated, variable 0-24 VDC source provided this current which was determined by measuring the voltage drop across a reference resistor (9.978 ± 0.001 Ω). This voltage and that of the DC supply (manally set) were measured with ±1 μvolt accuracy using a Keithley Model 199 DMM with scanner option. The DC supply was stable to a minimum of 1 ppm. The differential thermocouple voltage was measured with a Keithley Model 181 nanovoltmeter (accuracy: ± 10 nanovolt). Each data point was obtained in the following way:

1. The initial 'zero' readings of the nanovoltmeter were recorded.
2. The Manganin (inner cylinder) heater was energised.
3. If the cell was below 30 K, heater power was automatically reduced by an amount equal to the power delivered to the Manganin heater.
4. The thermocouple voltage was recorded for 50-300 readings.
5. The Manganin heater was switched off.

6. After the thermocouple voltage settled (about 1 minute), the final 'zero' readings were taken.

Step (3.) was included in the procedure to eliminate acute temperature drift during data collection at temperatures below about 15 K; even at power levels as low as 20 mW, the heat energy released by the inner cylinder during a data run was sufficient to drive the entire cell temperature upwards. By reducing the cell heater power by identically the amount delivered to the inner cylinder, the net electric heating power delivered to the cell remained fixed. Furthermore, since the temperature difference between inner and outer cylinders was directly related to the power level, the relative uncertainty in the thermocouple voltage (and the final result) was reduced by using higher power levels. Higher power levels were also useful during trials in the solid phase, which had a much higher thermal conductivity than the fluid phase. The cell temperature was recorded frequently during the entire run (about 3 times per second); total drift was always below 100 mK, and frequently less than 50 mK, during individual trials. For $T \leq 15$ K, drift was about 10 mK.

3.4.3 Details of the Calculations

The thermal conductivity was determined for each temperature/pressure pair in two stages. The initial value was obtained from a direct application of equation (3.23), in which the cell geometric constant K_1 was (0.2978 $\pm$ 0.0001) m^{-1}. The final value was found by applying several correction factors.

The temperature difference between concentric cylinders was found by dividing the differential thermocouple voltage by the thermopower:

$$\Delta T = \frac{\Delta V_0}{S(T)}, \tag{3.26}$$

where S(T) was obtained by differentiation of a standard expression for the thermoelectric voltage of a AuFe-Chromel pair as a function of temperature [32].

$$E(T) = \sum_{1}^{14} b_i T^i, \tag{3.27}$$

$$S(T) = \frac{dE(T)}{dT}. \tag{3.28}$$

The behaviour of S(T) is shown in Figure 3.12.

As mentioned in section 3.3.3, the heater power term $\dot{Q}$ was subjected to a proportionality factor 'f' equal to the fraction of the internal heater length

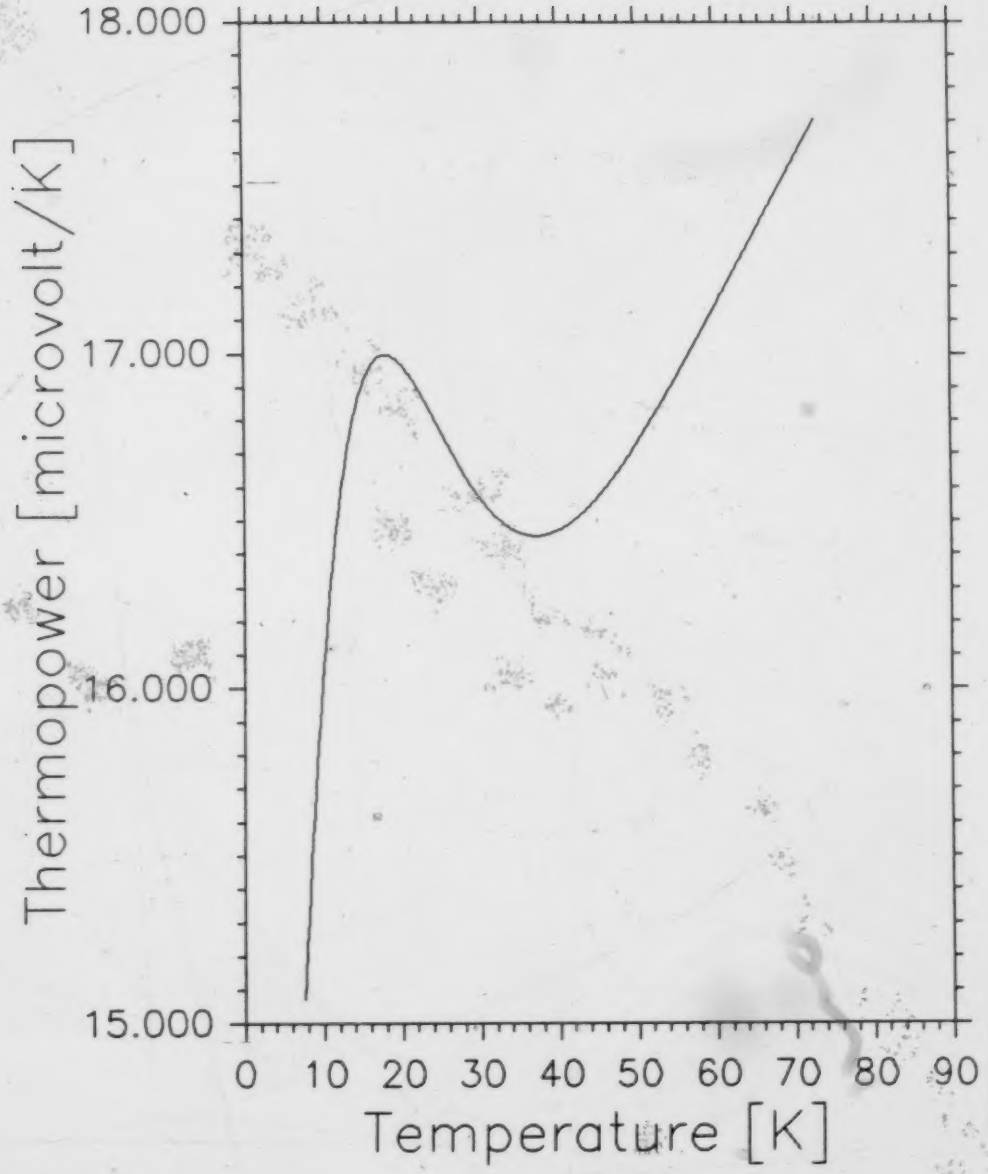

Figure 3.12: Thermopower of Au-Fe vs. Chromel

in direct contact with the inner cylinder. From a purely geometric standpoint, $f = 0.56487$. A series of simple tests showed that for typical ranges of heater power, the inner cylinder probably *gained* a small quantity of heat from the guard cylinders, rather than losing heat (anticipated) or being in thermal equilibrium (ideal case). These tests were performed on the concentric cylinder arrangement installed in the cell, at ambient temperature, and with an air/helium mixture at 1 atmosphere as the sample fluid. The heat gain was estimated by placing the inner cylinder thermocouple first in the guard cylinder and running a set of trials, followed by a set at the same power levels with the thermocouple located in the inner cylinder. By using the known value of the room temperature thermal conductivity of the Vespel spacers [35] separating the inner and guard cylinders, the known thermal conductivity of the stainless steel heater sheath, and the temperature difference between the inner and guard cylinders, an estimate of the longitudinal heat flux in or out of the inner cylinder was found. The direction of the heat flux was *from* the guard *to* the inner cylinder, and the magnitude was approximately 6% of the heater power. The final values of the thermal conductivity coefficient reported, however, do not include this factor because the tests which led up to it were not carried out under typical experimental con-

ditions. Unfortunately, a subsequent set of trials under realistic experimental conditions could not be obtained since the measuring system was damaged when removed from the cell. *The lack of precise knowledge of the longitudinal heat flux in/out of the inner cylinder was the main source of uncertainty in the results.*

The first estimate of λ thus consisted of the following expression:

$$\lambda = K_1 K' \frac{S(T)}{\Delta V_0} \frac{V_1 V_2}{R}, \tag{3.29}$$

where V_1 is the voltage across the inner heater, and V_2 is the voltage across the constant resistor ($R = 9.978 \pm 0.001\Omega$). The constant terms can be grouped into one, giving:

$$\lambda = 0.01686232 \times \left[\frac{S(T)}{\Delta V_0} V_1 V_2 \right]. \tag{3.30}$$

A set of correction terms were found for λ. This included a term to account for the thermal contraction of the BeCu inner cylinder during cool down from room temperature (where the dimensions were measured), a term to accomodate the placement of the thermocouples *not* at the surfaces of the inner and outer cylinders, a term to account for a heat path along the AuFe common element of the differential thermcouple, and a radiation loss term.

Since the geometric constant involved the radii r_1 and r_2 in a logarithmic ratio, the thermal contraction correction of these terms was very small and only that of the inner cylinder length, l, was relevant. The $\frac{\delta l}{l}$ % vs. temperature relationship for BeCu is known for between 82 K and 300 K [41], and was extrapolated down to 10K. The resulting values amounted to a correction of less than 0.1%.

The thermcouples were located in small wells machined in the inner and outer cylinders and hence recorded a temperature difference somewhat larger than the true difference at the opposing lateral surfaces of the cylinders. The equation for this correction term can be derived by consideration of the most probable temperature distribution (see Figure 3.13) and Fourier's equation. It should be noted that the version of this equation given in "Thermal Conductivity" (Vol. 2), Tye, R.P., pg. 104, is in error. The proper form is:

$$\Delta T_{true} = \Delta T_{obs} - \frac{\dot{Q}}{\lambda_m 2\pi l}\left[ln\frac{r_1}{r_1^*} + ln\frac{r_2^*}{r_2}\right], \tag{3.31}$$

where the various terms are defined in the figure. λ_m is the thermal conductivity of BeCu which is known [42] to 5 K. The magnitude of this correction became increasingly large as $T \rightarrow 0$.

The next correction term was the secondary heat pathway along the AuFe

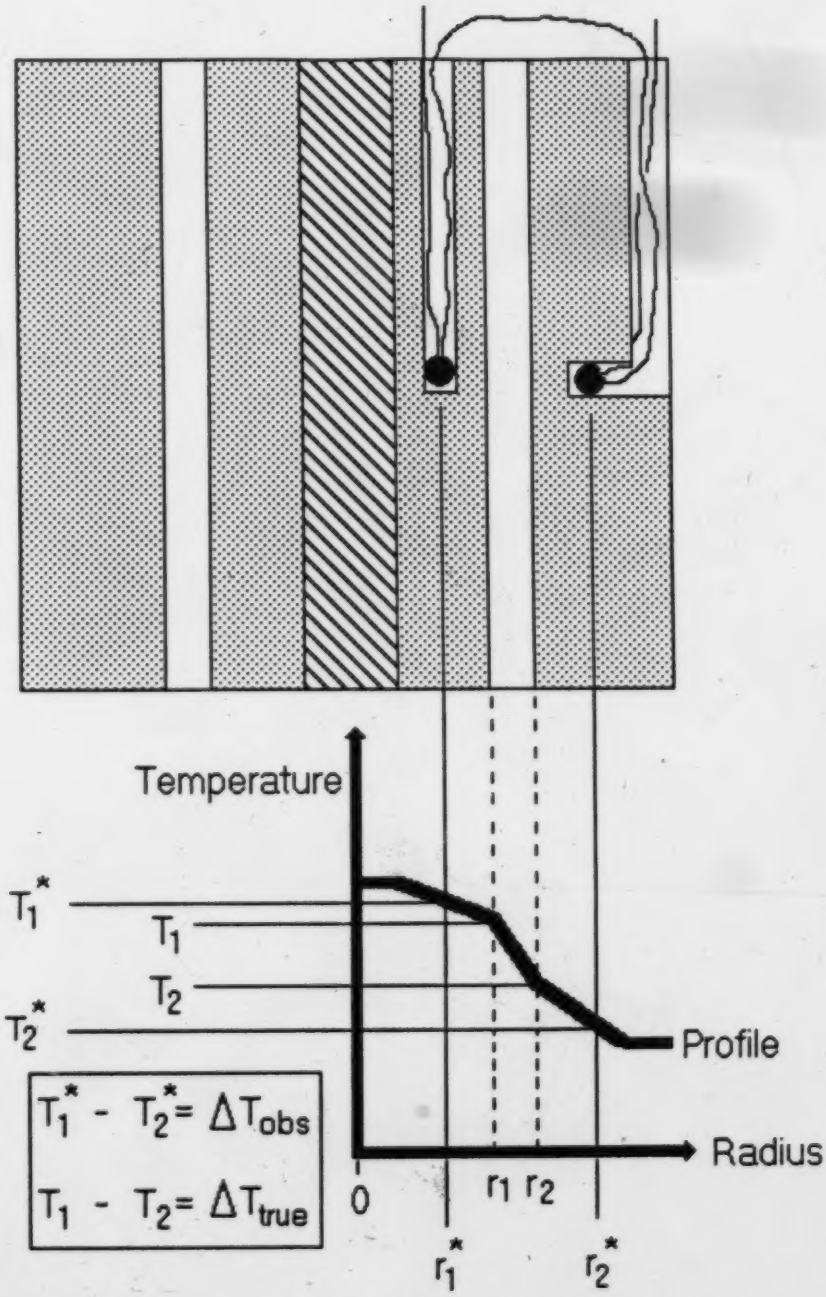

Figure 3.13: Temperature Profile between Cylinders

component of the thermocouples which linked the inner and outer cylinders directly. The AuFe wire had a diameter of 80 μm, was about 10 cm in length and had a thermal conductivity on the order of 200 $Wm^{-1}K^{-1}$, leading to a heat transfer of about 10 μW (or, $\sim$ 0.01%), which was ignored.

The final correction term, namely, that for radiative transfer of heat ($\dot{Q}_R$), was evaluated with the Stefan-Boltzman equation (3.32). Heat transfer near 10 K between the cylinders with a temperature difference of 1 degree, assuming a transparent fluid and perfect black body emission ($\epsilon_{1,2} = 1$, worst case), amounted to only 87 ηW. At 77 K, it was 34 μW. The actual temperature difference was about 100 mK, so the value of the radiative loss was even less. This quantity could be safely ignored.

$$\dot{Q}_R = 2\pi r_1 l \sigma_R \epsilon_{1,2} \left[T_1^4 - T_2^4\right], \tag{3.32}$$

where $\sigma_R = 5.6697 \times 10^{-8} Wm^{-2}K^{-4}$, the Stefan-Boltzman constant.

The cell pressure was read on a standard 100,000 psi Heise Bourdon gauge. Owing to a large excess volume of high pressure gas outside the cell (in the length of connecting capillaries, various valve bodies, the gauge, etc.) the cell pressure dropped only slightly during the entire cool down segment (i.e., $\Delta p \leq -3\%$). Thus, the experimental conditions during the fluid phase

measurements could almost be termed "isobaric". Nevertheless, the small pressure drop was incorporated into the equation of state which generated a corresponding molar volume.

It can easily be appreciated that during experimental trials, neither the pressure or temperature, nor even the density, were constant; this left the results in form which could not easily be used for comparison or further calculation, and suggested that the raw data should be recast in the form of thermal conductivity as a function of fluid density, rather than as a function of temperature over (almost) isobars. This implied the necessity of determining the molar volume ($\frac{cm^3}{mole}$) for each pressure and temperature pair by utilising an Equation of State (EOS) for fluid helium over the existence range in this experiment.

A major project carried out at the NIST in Boulder, Colorado (formerly, NBS) in 1972 [15] was the determination of a precise EOS for fluid helium over a broad range of pressure and temperature, from which many thermodynamic functions and properties could be found. The result was a mixed polynomial equation (McCarty EOS), giving the pressure (in standard atmospheres) as a function of the density (moles/litre) and the absolute temperature, which well represented all the then known P-V-T data at low temperatures.

$$P(\rho,T) = \rho RT[1 + B(T)\rho] + \sum_{i=1}^{8} n_{1i}\rho^3 T^{1.5-i/2} + \sum_{i=1}^{4} n_{2i}\rho^4 T^{1.5-i} + \sum_{i=1}^{6} n_{3i}\rho^5 T^{0.75-i/4} + \sum_{i=1}^{3} n_{4i}\rho^3 e^{\gamma\rho^2} T^{1-i} + \sum_{i=1}^{3} n_{5i}\rho^5 e^{\gamma\rho^2} T^{1-i} + \sum_{i=1}^{2} n_{6i}\rho^6 T^{1-i}, \quad (3.33)$$

where B(T) is the second virial coefficient, γ is a constant and the n_{ji} are constants. Rather than produce a single EOS, the range of applicability was divided up into three regions, to each of which there corresponded a different set of constants. The range of applicability was limited to $0 < P < 1000$ bar and $2 < T < 1500$ K (fluid phase only).

To calculate the molar density of the fluid, an iterative procedure was used since direct inversion to solve for the density would have involved intractable mathematical problems. This procedure consisted of first generating a 'seed' value for the density, then substitution along with the temperature to solve for the pressure. If this estimate of the pressure differed by more than 0.01 bar from the known pressure, a correction term was found for the density by differentiation of equation 3.33:

$$\frac{dP}{d\rho} = P'(\rho,T), \quad (3.34)$$

$$\Delta\rho \sim \frac{\Delta P}{P'(\rho, T)}. \tag{3.35}$$

The correction term ($\Delta\rho$) was subtracted from the density estimate and the new value entered into the EOS to again find the pressure. This procedure was repeated until the density correction was $< 10^{-4}$ mole/litre and the pressure difference (between real and calculated values) was < 0.01 bar.

Other research [57] carried out at much higher pressures by Mills, Liebenberg and Bronson led to the development of an EOS modelled on the Benedict equation for nitrogen [59]. Here, the range of applicability extended from 2 kbar to 20 kbar and from 75 K to 300 K. This equation directly related molar volume to pressure in kbar and temperature in Kelvin.

$$V = \sum_{m=1}^{3} \sum_{-n=2}^{2} A_{nm} T^{n/2} P^{-m/3} \tag{3.36}$$

The authors of this equation (MLB EOS) have stated that, although their experimental data were obtained at 77 K and 2 kbar and higher, their EOS could be extrapolated down to 50 K and 1 kbar while maintaining reasonable agreement (i.e., within an average error of 1.3%) with values calculated using the McCarty EOS. Thus, these two regimes meet in the P-T plane, but they do not overlap; furthermore, even in combination they leave a very large gap for which no EOS has been reported (i.e., coefficients have not been

calculated), due perhaps to a lack of P-V-T data here. This gap extends upwards in pressure from 1 kbar, and from near the melting line up to about 50 K, where the MLB EOS can be subsumed. Unfortunately, most of the data in this experiment were obtained from points in the gap for which we have no explicit EOS. These regions are shown in Figure 3.14; the gap has designation A'.

The problem of determining the molar volumes in an existence range without an explicit EOS was temporarily solved by extrapolating the two EOS predictions and then taking a linearly weighted average, where the weighting factor for each prediction was determined by the distance from the respective limits of applicability. This led to smoothed linking of the values when switching from one EOS to the other, which was necessary for region A (P > 1 kbar and T > 50 K). The explicit weighting factors were as follows:

1. For the McCarty EOS:

$$W_1 = \frac{75 - T}{25} \tag{3.37}$$

2. For the MLB EOS:

$$W_2 = 1 - W_1 \tag{3.38}$$

The MLB EOS alone was used in region B (P > 2 kbar and T > 75 K),

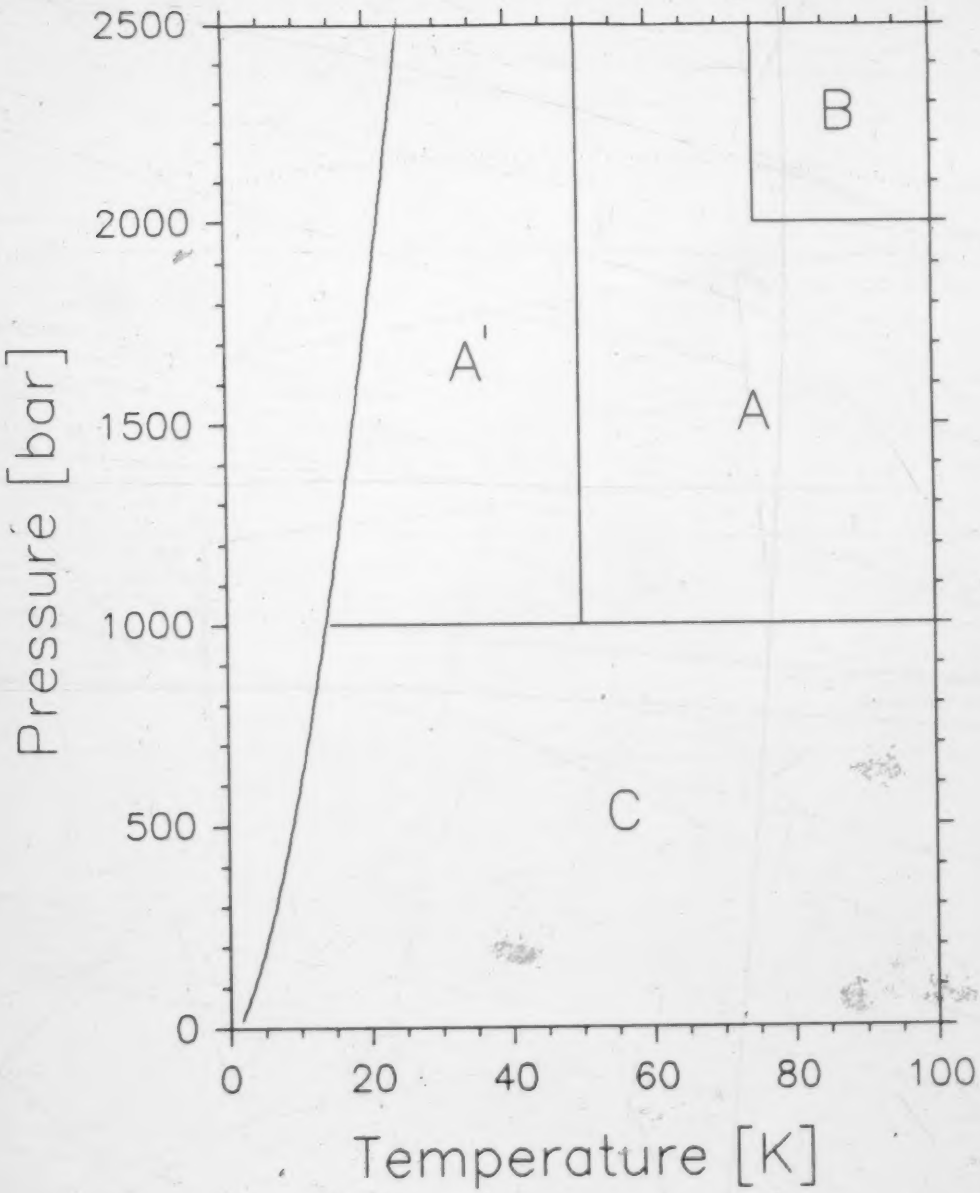

Figure 3.14: Phase Diagram and Equations of State

while the McCarty EOS was used exclusively for region C ($P < 1$ kbar). In the 'gap' region A' ($P > 1$ kbar and $T > 15$ K) the McCarty EOS was extrapolated upwards for all pressures since the MLB EOS exhibited unreliable behaviour (fluctuations) below 50K.

Chapter 4

Results

4.1 System Testing

To determine if convection were present in the trapped fluid, a series of trials were performed at a single pressure and temperature (700 bar, 78K). Convective effects, if present, would lead to a non-linear thermocouple differential temperature as a function of applied heater power and a pseudo-increase in the thermal conductivity values. The test consisted of varying the supply power from 5 mW to 600 mW (to the Manganin inner cylinder heater) and recording the thermocouple voltage. The results are shown in Figure 4.1 as the resultant thermocouple differential temperature vs. heater power. The

test revealed a very linear response over this range (i.e., correlation coefficient = 0.99991), signifying that convection was absent. Furthermore, the best-fit line passed through the origin, which indicated that the measuring system was probably free of systematic errors.

However, a separate series of trials at 1000 bar and 78 K did reveal that the final values of thermal conductivity were weakly dependent on the heater power, as can be seen in Figure 4.2. This graph shows the effect for a range of values from 1 mW to 400 mW, but most experimental trials were run near 40 mW. The line in the figure is a third order polynomial best fit to the open circles, and when extrapolated to the limit of zero power shows that recorded thermal conductivity values were possibly about 1.4% high. The figure also shows that the measuring system became unstable at very low power levels (filled circles).

Since the steady state method employed here leads to an absolute determination of the thermal conductivity of helium, the only means of verifying the results is by comparison with other work. For the range of temperatures and pressures in this experiment, comparison can only be made with the work of Golubev et. al. [36]. A total of 9 trials at an average temperature of 78.03 ± 0.04 K over a region of overlapping pressures were performed;

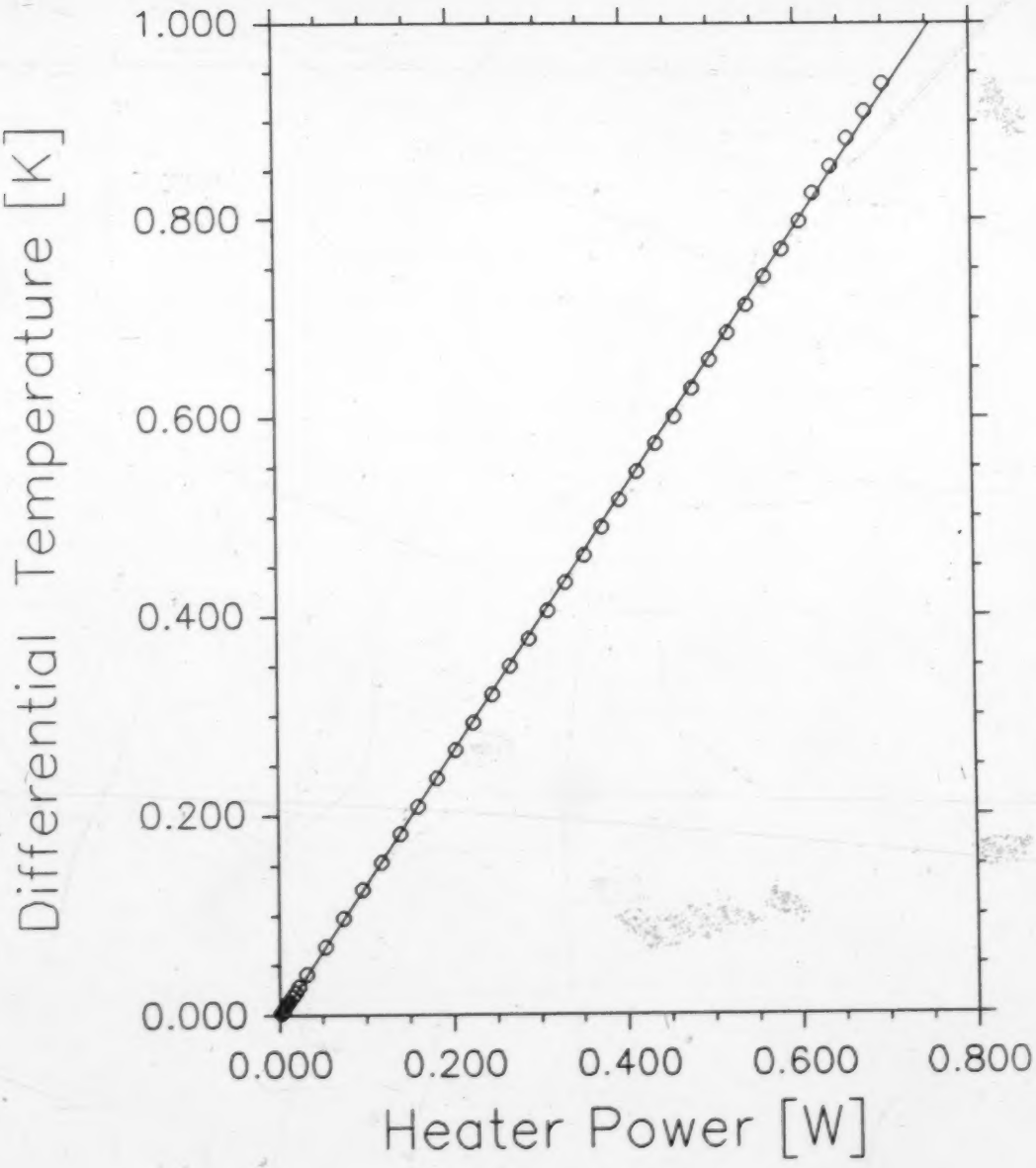

Figure 4.1: Linearity Test of the System

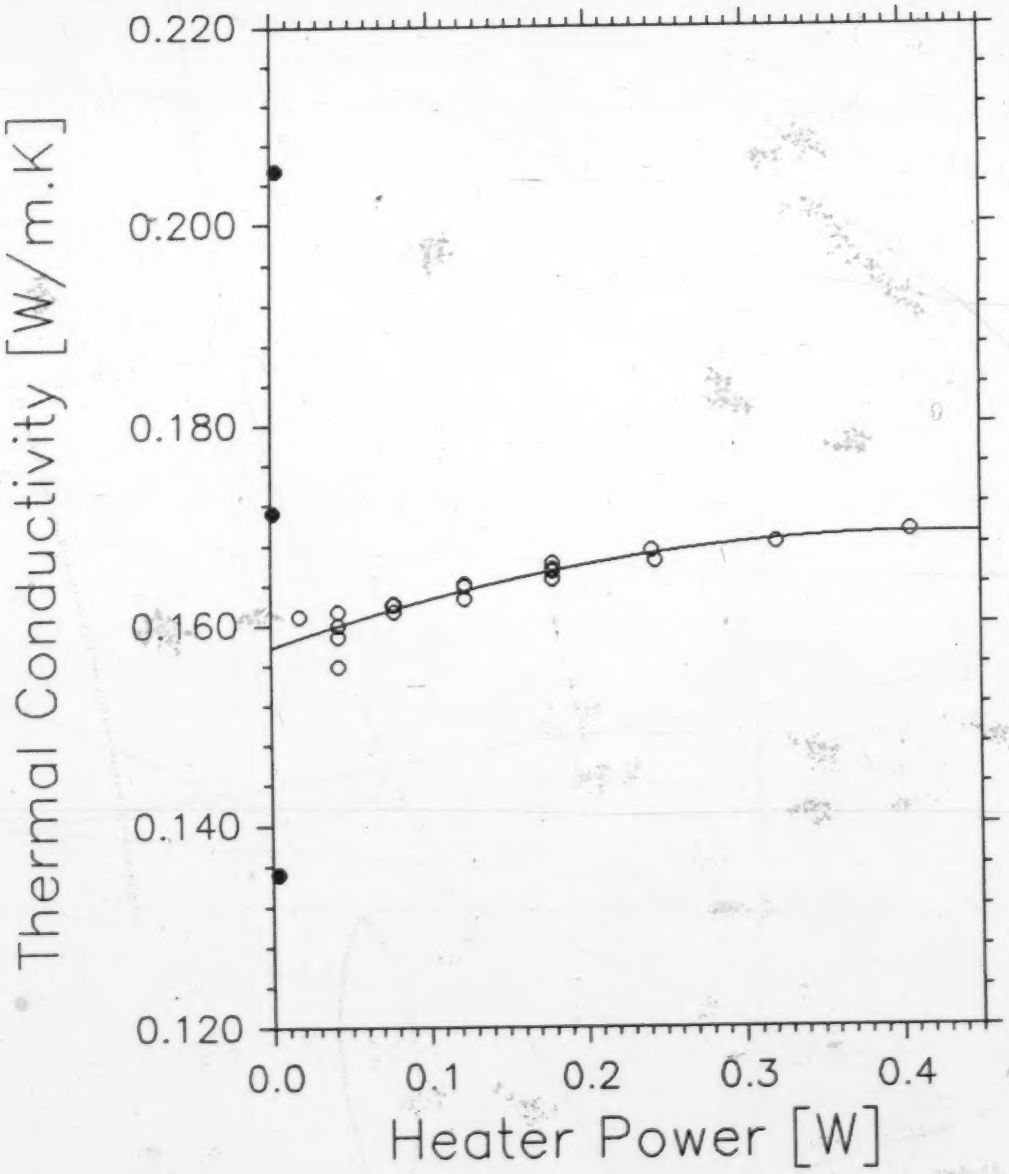

Figure 4.2: Thermal Conductivity as a function of heater power.

these (filled circles) are shown along with the 77 K isotherm extracted from Golubev (open circles) in Figure 4.3. Although the two experiments are in excellent agreement this may be a fortuitous coincidence. Genuine agreement would imply that end-loss corrections are negligible for the measuring instrument developed for this project! It is interesting to note that a "transient" method,–in contrast with the steady state method here,–was used by Golubev; this consisted of a concentric cylinder arrangement in which the cooling history of the inner cylinder was monitored (previously referred to as the concentric cylinder (cooling) method in Section 3.1).

Results have been reported for existence ranges outside the parameters of the present project. LeNeindre et. al. [49] obtained the thermal conductivity of helium, neon, argon, krypton, and xenon at room temperature at high pressures (up to the melting line in some cases), and it was shown by Abdelazim [48] that modified Enskog theory (MET) very accurately modelled the results for helium. Acton [50] measured the thermal conductivity of the dilute gas, dense gas and liquid helium at low pressures ($\leq$25.5 atm). Studies of the thermal conductivity of solid helium have concentrated on U-process behaviour; the results can be extrapolated toward the melting line assuming an exponential dependence in temperature (equation (4.2)). Perhaps the

most sensitive examination of thermal conductivity in solid helium is due to Seward et. al. [37], who obtained results at pressures up to 1 kbar. Experimental data were also obtained by Bertman et. al. [63], and much earlier at low pressures by Webb et. al. [39]. An overall assesment of thermodynamic and transport properties of helium was completed by McCarty [15] at NBS (now, NIST) in 1972 which incorporated all the then known experimental data.

Some preliminary results of this project were reported earlier [51], covering a narrower range of pressures but using the same apparatus described in Chapter 3. The technique to obtain these earlier results was essentially the same but without the automatic, independent recording by computer of the thermocouple voltages and temperature. Owing to the mistake in the correction formula for placement of thermocouples (see Section 3.5.3), the values of the thermal conductivity for the solid were all significantly *low*, nevertheless, a similiar trend in the ratio of thermal conductivities can be deduced. The mistake in this formula was discovered as the data for this thesis were being prepared.

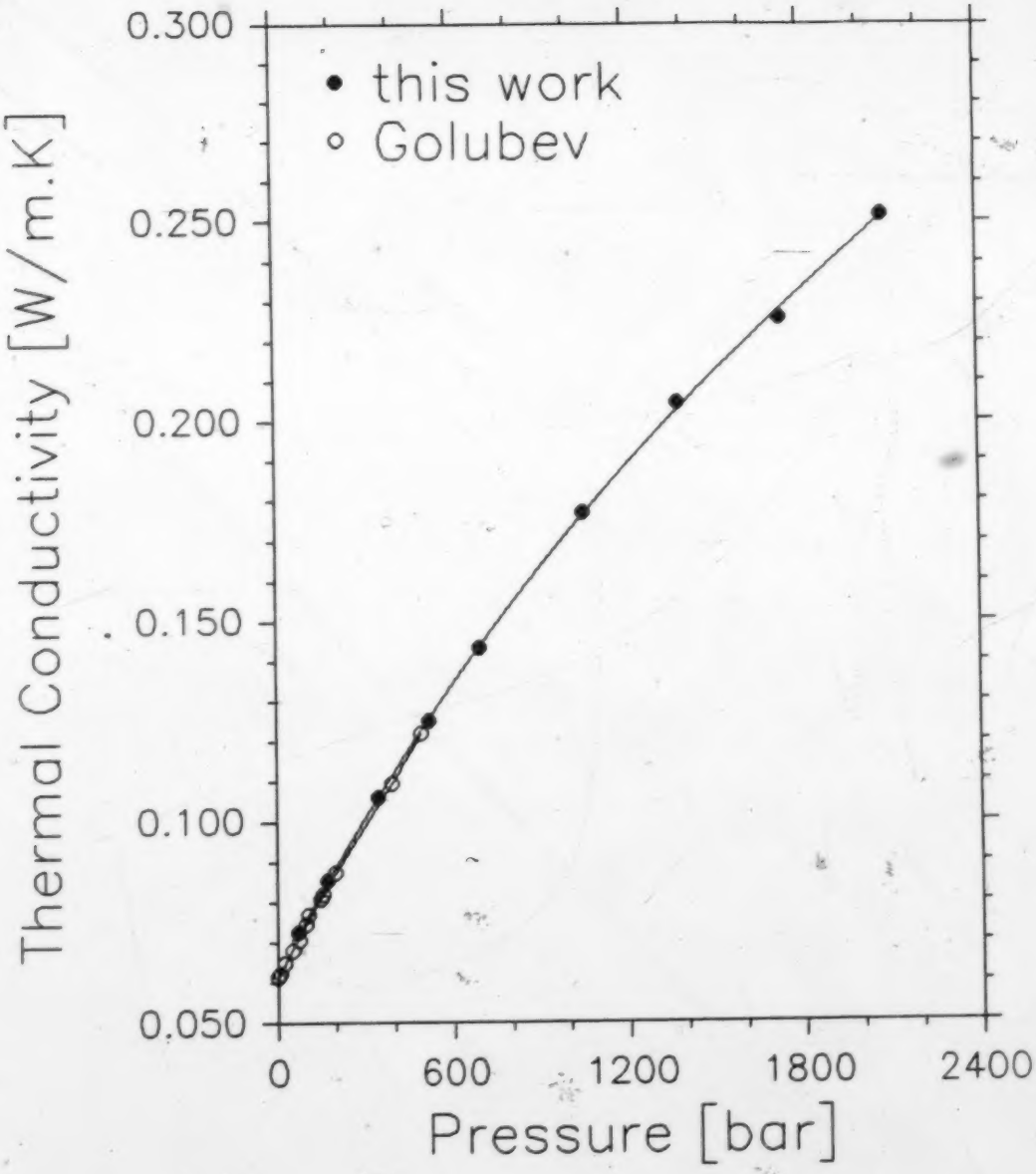

Figure 4.3: Comparison with Previous Work

4.2 General Results

A total of 11 trials were performed at 7 different values of pressure ranging from 450 bar to 2050 bar, and over temperatures ranging from 7.50 K (minimum) to 80 K. The results were amalgamated into 8 separate trials with the results shown in Table 4.2. P_{init} is the cell pressure at the start of each trial; the cell pressure was nearly constant during the cool-down from 80K to the melting point. The value of P_{init} for trial 5b. is unknown due to an error in data aquisition; in this trial, a valve located between the cell and Heise gauge (Figure 3.6, (C)) was accidentally closed for the entire run. This meant that the pressure loss during cool down was larger than in all other trials; the melting pressure for trial 5b. was determined from the observed melting temperature. Values of thermal conductivity for the solid λ_s in trials 2 and 3 are unknown due to insufficient number of data points at the lowest temperatures. T_{mf} is the melting point observed from the graphs (Appendix A), where it has been assumed that the temperature associated with the abrupt change in the thermal conductivity curve coincides with onset of solidification. P_{mf} is the corresponding melting pressure, calculated with a Simon-type melting equation and using empirical constants as quoted

	$T_m \leq 14K$	$T_m > 14K$
a	-20.6	-8.112
b	17.452	16.91
c	1.54681	1.555

Table 4.1: Constants in the Simon melting equation

in Driessen [60] for the overlapping regions $4K < T_m < 25K$ [61] [62] and $14K < T_m < 100K$ [57].

$$P_m = a + bT_m^c \tag{4.1}$$

The constants a, b, c are given in Table 4.1.

ΔP_{calc} is the pressure drop in the cell during the fluid-solid transition, where it has been assumed that this occurs under isochoric (constant volume) conditions; values of this quantity were also obtained from Driessen, and ΔT_{calc} is the expected value of the temperature width of the transition [60]. The final two columns contain values of thermal conductivity of the two phases at, or in the vicinity of, the transition; these were read visually from graphs of the raw data given in Appendix A. λ_f was read from that point on

each graph where the thermal conductivity made an abrupt "jump", which was also the marker for the onset of solidification, T_{mf} . The value of λ_s was taken from that point on the thermal conductivity curve situated ΔT_{calc} below T_{mf} .

Since it is impossible to know exact details of solidification within the cell, it has been assumed as a first approximation that solidification *within the concentric cylinders* was an isochoric process; this means that there was a finite thermal and pressure width to the transition, and the pressure in the solid was less (by ΔP_{calc}) than the fluid from which it formed. Thus, the values of thermal conductivity of fluid and solid helium were taken at different pressures.

The individual trials shown in Appendix A reveal behaviour reminiscent of that previously observed for the thermal conductivity of solid [63] and of liquid [64] helium at low pressures near a melting point of 1.9 K. These disparate sources of data have been combined [66] in order to examine the behaviour of the thermal conductivity at melting, and the representative graph is shown in Figure 4.4. The values in the solid regime were calculated using a semi-empirical relation based on the theory of Peierls [6] for the effect of the Umklapp process (equation (4.2)), while the values in the fluid

Trial	P_{init}	T_{mf}	P_{mf}	ΔP_{calc}	ΔT_{calc}	λ_f	λ_s
No.	(bar)	(K)	(bar)	(bar)	(K)	($Wm^{-1}K^{-1}$)	
1.	486.1	8.0	415	113	1.40	0.066_5	0.26_6
2.	906.6	10.30	623	159	1.70	0.087_3	(?)
3.	954.9	12.00	794	196	1.94	0.10_2	(?)
4.	1291.0	14.00	1016	242	2.20	0.11_3	0.55_8
5a.	1646.1	18.90	1625	365	2.85	0.18_5	0.68_2
5b.	1650est	18.90	1625	365	2.85	0.18_0	0.67_1
6.	1975.0	20.90	1902	419	3.10	0.21_0	0.69_9
7.	2054.6	21.05	1923	423	3.11	0.22_2	0.78_4

Table 4.2: Summary of Trials. The first two digits in λ_f and λ_s are considered significant.

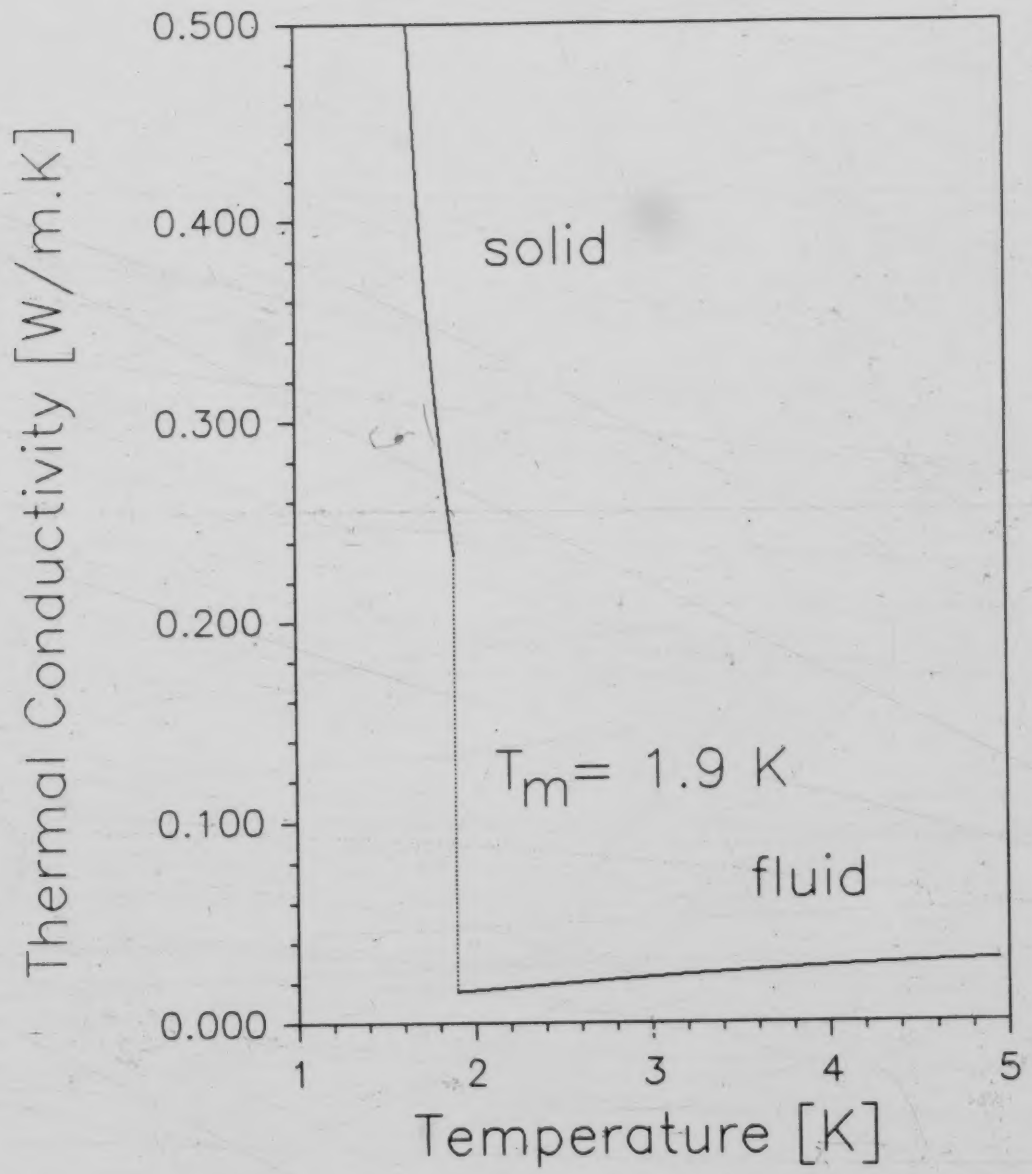

Figure 4.4: Thermal Conductivity of solid and fluid helium at low pressure

regime were obtained from an empirical relation (equation (4.3)) derived by Kerrisk [64] for the thermal conductivity along the P = 26 atm isobar. By contrast, this experiment constitutes the first critical examination of the thermal conductivity behaviour of both phases in the *same* apparatus.

For the solid, where $A = 1.9 \times 10^{-3} W m^{-1} K^{-1}$, b = 2.9 (related to phonon dispersion), $n \sim 0$, and $\Theta_D = 26.5K$, the Debye temperature for this density:

$$\lambda_s = AT^n exp\left[\frac{\Theta_D}{bT}\right]. \tag{4.2}$$

For the fluid:

$$\lambda_f(T, P) = F_0 + F_1 T + F_2 P + F_3 T^2 + F_4 P^2 + F_5 PT, \tag{4.3}$$

where:

$F_0 = -1.4642 \times 10^{-5}$,

$F_1 = 8.8025 \times 10^{-5}$,

$F_2 = 9.1386 \times 10^{-13}$,

$F_3 = -8.700 \times 10^{-6}$,

$F_4 = -4.1701 \times 10^{-20}$,

$F_5 = 8.3023 \times 10^{-13}$,

P in units of $dyne/cm^2$.

Having indicated in Section 3.4.2 that the trials were conducted under nearly isobaric conditions (pressure change only ~3% during the fluid phase trials), it may appear contradictory to state that the freezing transition occured under isochoric conditions. The explanation lies in the following peculiar feature of the apparatus: freezing always occured *first* in the capillary which connected the cell to the Heise pressure gauge, and then later in the cell. This is because the stainless steel capillary could not, for safety reasons, be subjected to sharp (i.e., small diameter) bends, and so was wound along a circuitous route from the cell to the vacuum feedthrough and out of the cryostat. It is very likely that along this route, the capillary made contact with some part of the cryostat that was always colder than the cell ("cold touch"), and the helium froze at this location in the capillary while the helium inside the cell remained in the fluid state. The important feature is that when the frozen capillary became effectively blocked, the cell was isolated from the pressure gauge.

During the trials, the pressure gauge reading was observed to fall very slowly as the cell cooled, then to reach some plateau value (likely when the capillary blocked) while the cell temperature continued to drop. Below this temperature, the cell could be considered to be isolated, and hence further

cooling through the freezing transition was under isochoric conditions. This is borne out by the experimentally observed freezing point (i.e., T_{mf} or the liquidus) which was always lower than would be expected by reading the pressure gauge. Further evidence of the blocked capillary was obtained by simple experiments: with the helium sample in the cell frozen (and with the capillary therefore blocked), the pressure outside of the capillary was lowered 50 bar by venting some gas to atmosphere; the cell was then gradually warmed until clear evidence (i. e., thermocouple signal) was given of melting of the contained sample. However, it was not until the cell was warmed above the melting point by 5 to 10-degrees that the capillary became unblocked, as indicated by an abrupt increase on the gauge.

As far as the thermal conductivity measurements were concerned, the blocked capillary meant that values for solid helium were obtained at pressures lower than for fluid helium in the same trial. This is because an isochore in the P-T plane intersects the phase boundary line at two distinct points, as shown in Figure 4.5 (points 'mf' and 'ms'). The values of λ_f were obtained at pressures P_{mf} (liquidus point), while the λ_s were obtained at P_{ms} (solidus point). The isochores of helium have been sensitively analysed and tabulated in Driessen [60]. Liquidus and solidus for helium are shown in Figure 4.6;

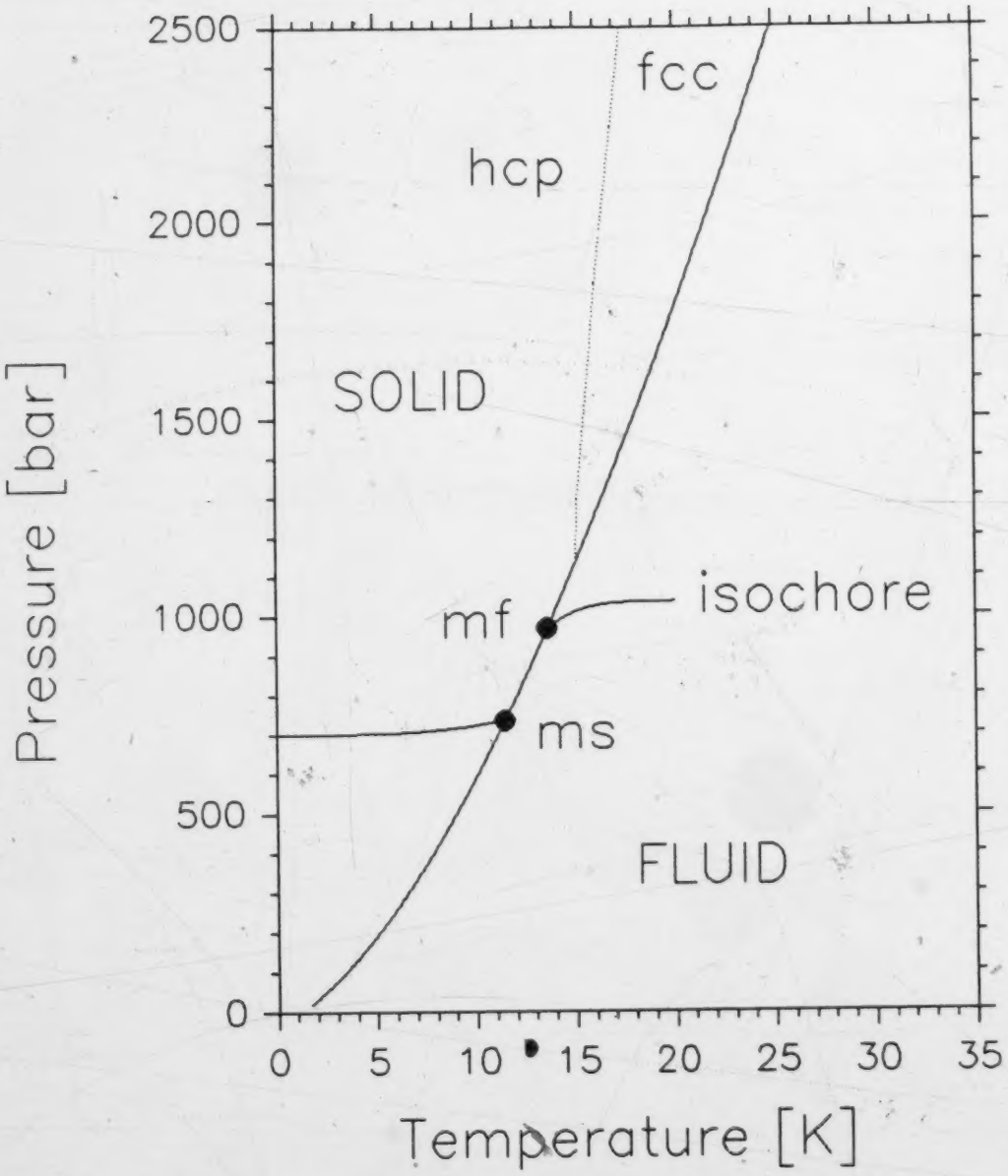

Figure 4.5: Phase Diagram and the $13.00 \frac{cm^3}{mole}$ isochore

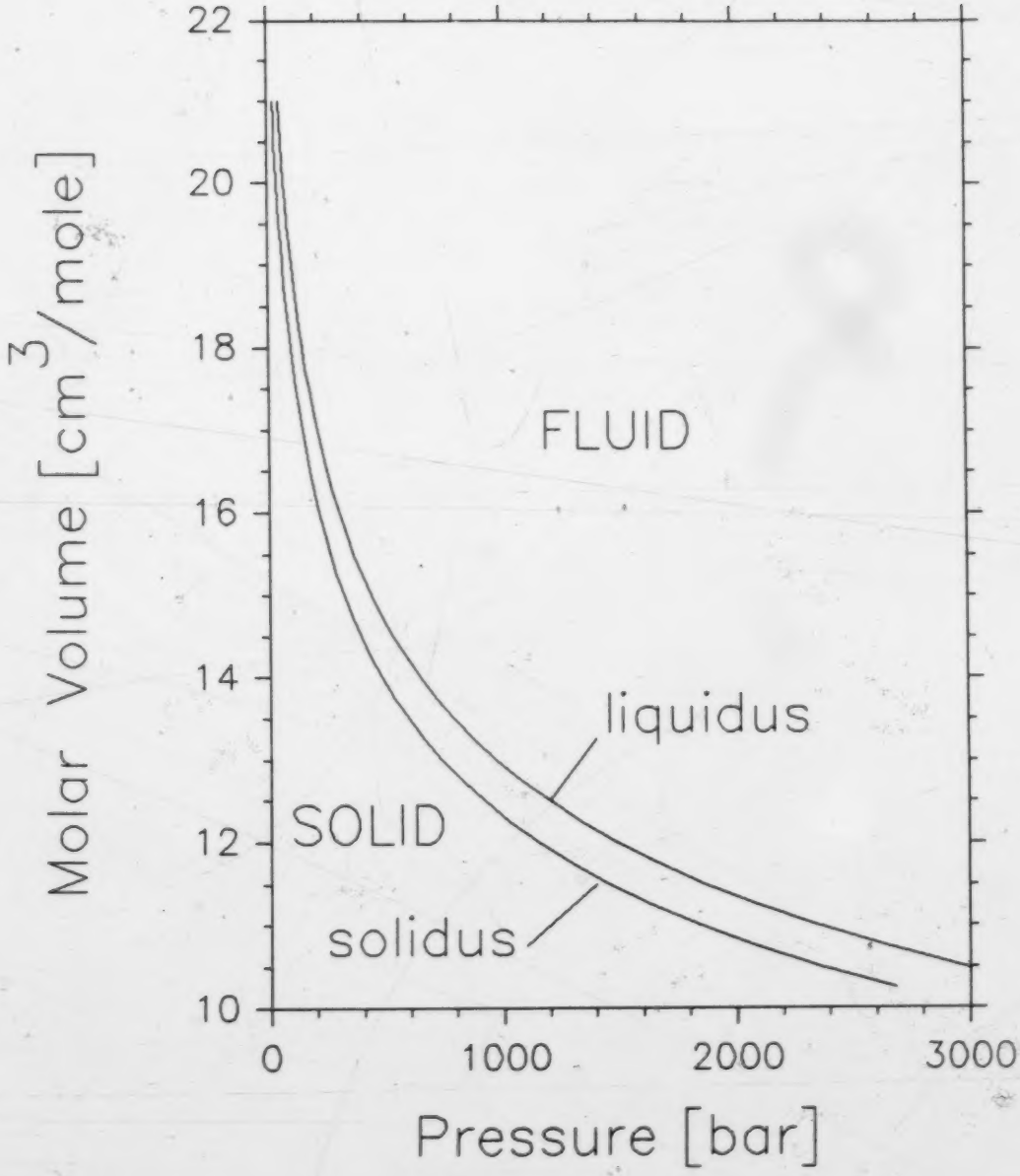

Figure 4.6: Liquidus and Solidus lines in Helium

the region between the lines corresponds to a mixed phase of fluid and solid. In preparation of the final graph of thermal conductivity vs. pressure, the values for solid helium had to be shifted *down* by amount ΔP_{calc} from P_{mf} for each trial in Table 4.2.

The difficult interpretive task was the attempt to identify T_{ms} from the thermal conductivity curves. It has already been mentioned that the onset of solidification, as indicated by the abrupt "jump" in thermal conductivity, was rather unambiguously marked in all cases. By constrast, there did not appear to be any similarly clear signal for T_{ms} . Therefore, it was assumed as a first approximation that the intermediate phase of combined fluid and solid existed over the entire thermal width of the transition, i.e., between T_{mf} and T_{ms} , and the cell was completely filled with solid only at T_{ms} . The value of T_{ms} was obtained from T_{mf} by reference to Driessen [60], who has provided tables of P-V-T data for the solid up to T_{ms} and the fluid at T_{mf} .

The derived data were plotted as a function of melting pressure, and shown in Figure 4.7. Since there were initial uncertainties in determining the longitudinal heat flux from the inner cylinder, and there were further uncertainties in graphically reading the thermal conductivity values, a sim-

ple average line (best-fit, or least squares analysis) was used to represent the results; any other fitting procedure is probably not justified. Low pressure values are shown in the figure as a filled triangle [63] for the solid ($\lambda_s \sim 0.233 Wm^{-1}K^{-1}$), and an open triangle for the fluid ($\lambda_f \sim 0.017 Wm^{-1}K^{-1}$ [64], $\sim 0.024 Wm^{-1}K^{-1}$ [50], $\sim 0.036 Wm^{-1}K^{-1}$ [52]). The former values for the fluid are experimental, while the latter is quantum-mechanically calculated.

The ratio of thermal conductivities *at the same pressure* corresponds to the experimental conditions during dendritic solidification, to which reference has previously been made. This ratio was determined by simply calculating and plotting the ratio of the two straight lines representing solid and fluid, and is shown in Figure 4.9 as line 'A'. The ratio is relatively constant at the higher pressures ($\beta \rightarrow 4.3$), but gradually rises at the lower pressures, and rises steeply to an apparent limiting value of $\beta \sim 9$ as $P \rightarrow 0$. Of course, not much confidence can be attached to the numeric values of the ratio owing to the uncertainties associated with the various levels of this simple analysis. As can be easily appreciated, the value of the ratio is a strong function of the ratio of the slopes of the straight lines in the limit of high pressure. It can be concluded with certainty, however, that the ratio is anomalously high at

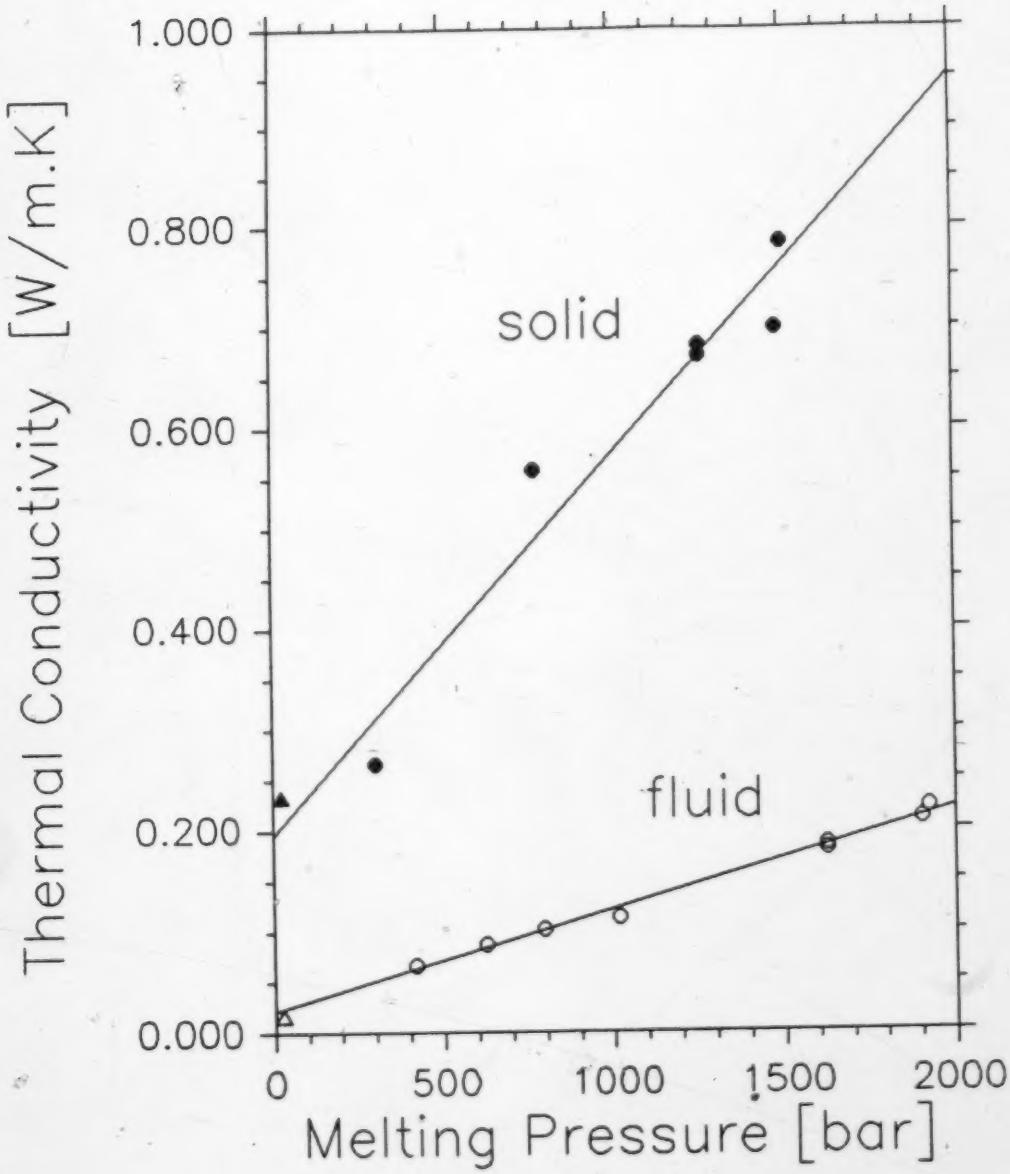

Figure 4.7: Thermal Conductivity versus Pressure (isochoric freezing)

pressures above 1 kbar and reaches even higher values as the melting pressure is reduced.

The foregoing constitutes a conservative assesment reflecting the inherent difficulty in finding T_{ms} in the thermal conductivity curves. The raw data curves show an additional feature which might be interpreted as an enhancement of the thermal conductivity in the mixed solid-fluid phase. This can be seen in the graphs as a small "bump" situated below T_{mf} in the anticipated mixed phase region. It may be speculated that the bump itself represents the entire transition region, and that its' low temperature side is at T_{ms}. However, the width of the bump in all of the trials is substantially smaller than the known thermal width of the isochoric freezing process, ΔT_{calc}, as shown in Table 4.3.

How could this small enhancement region be understood to represent a compressed transition region? Perhaps the assumption of an isochoric freezing transition should be amended. Since there was a large excess volume of helium gas in the 2-meter length of Harwood 3M pressure conduit which connected the cell to the feedthrough block (Figure 3.2, (K)), once the capillary (E) had blocked, it was possible that helium freezing inside the cell could continue to draw on this volume of gas until the conduit also blocked.

Trial no.	ΔT_{calc} (K)	ΔT_{spec} (K)	λ_s $Wm^{-1}K^{-1}$
1.	1.40	0.55	0.25_3
2.	1.70	1.30	0.53_4 (?)
3.	1.94	1.15	0.48_1 (?)
4.	2.20	1.45	0.48_3
5a.	2.85	1.85	0.63_7
5b.	2.85	2.15	0.61_6
6.	3.10	2.15	0.60_1
7.	3.11	1.80	0.68_8

Table 4.3: Speculated Transition Widths and Thermal Conductivity

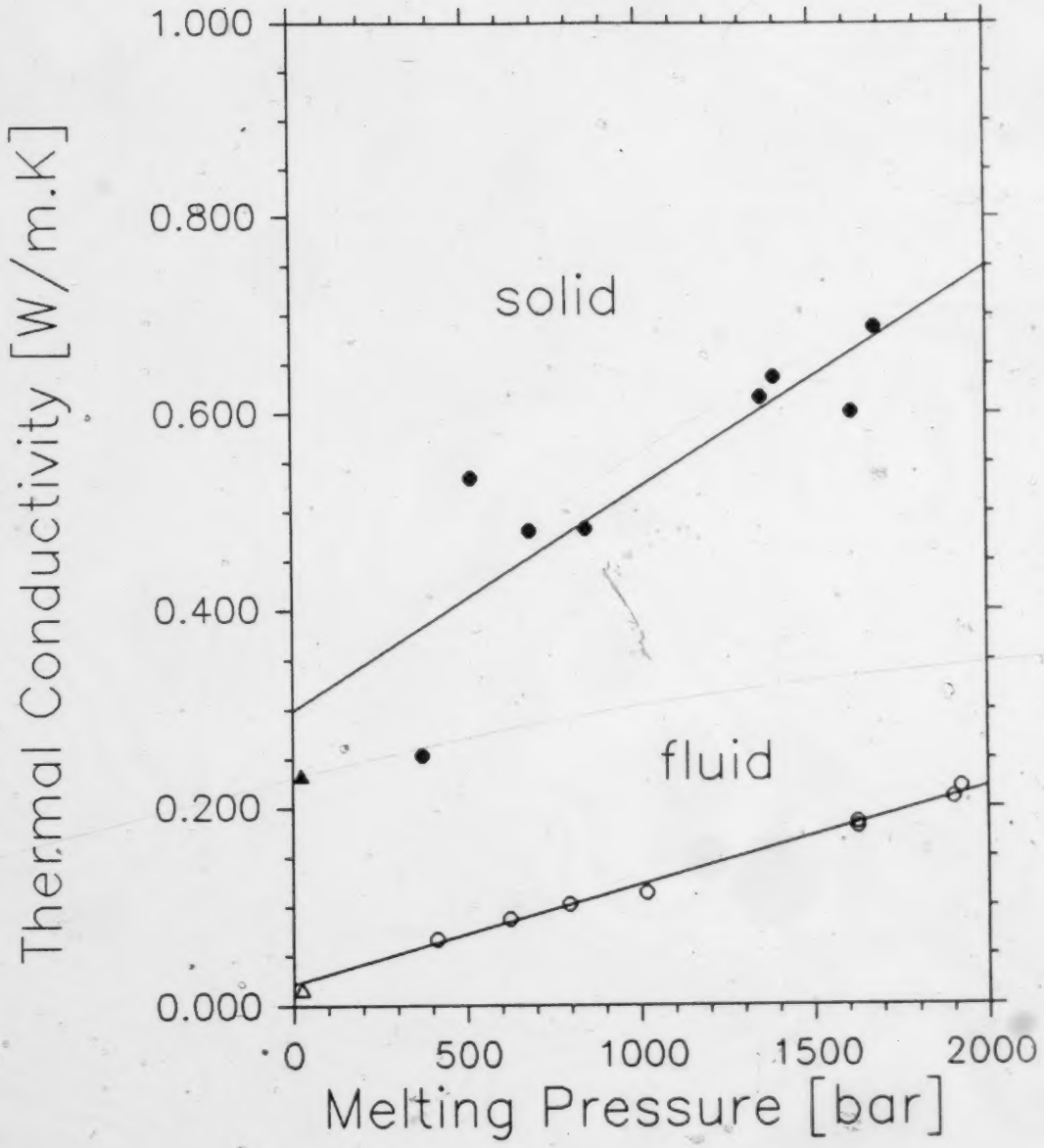

Figure 4.8: Thermal Conductivity versus Pressure

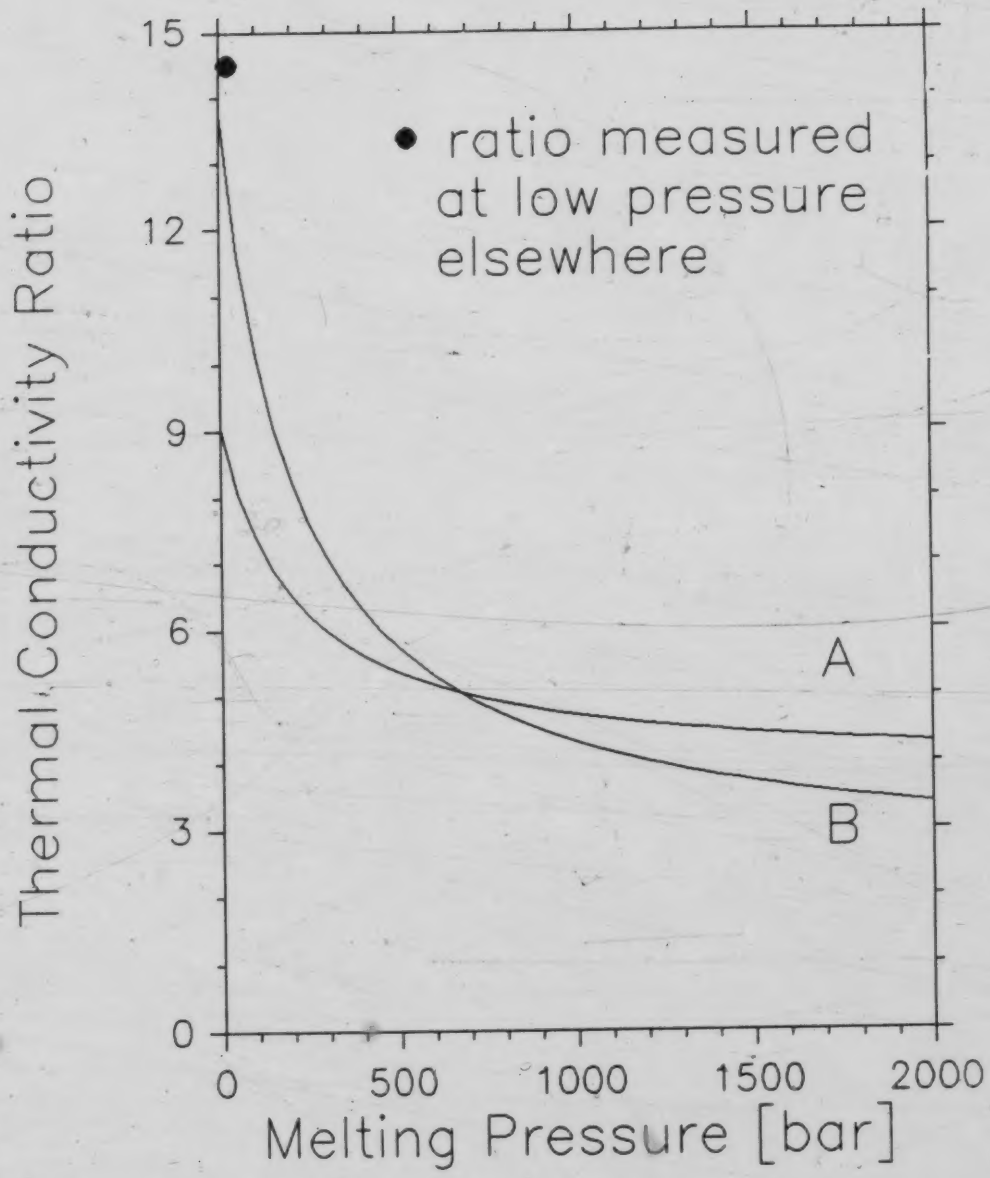

Figure 4.9: Thermal Conductivity Ratio versus Melting Pressure

After all, the cell was connected to the Swenson cooler at one end and to room temperature at the other via the pressure conduit, rendering a thermal gradient along the length of the cell. Therefore, one would expect the high pressure capillary to freeze first, then the cell, and finally the conduit. If this were true, the pressure drop in the cell would not be as large as in the case of the truly isochoric case; the transition would in fact be neither isochoric or isobaric.

To estimate this secondary correction, it could be assumed to a first approximation that the melting curve is linear in the transition region, and therefore that the ratio of the 'actual' to the calculated thermal width of the transition was equal to the ratio of the 'actual' to calculated pressure width of the transition:

$$\Delta P_{obs} = \left[\frac{\Delta T_{obs}}{\Delta T_{calc}}\right] \Delta P_{calc}. \tag{4.4}$$

As an example of these corrections, that for Trial No. 1 will be given explicitly. The thermal conductivity for the fluid near the transition, 0.0665 $Wm^{-1}K^{-1}$ is at 414.7 bar (unchanged). But the observed width of the bump in this case is only 39.3% of the expected value for an isochoric process, and so the pressure shift is assumed to be only 39.3% of 112.6 bar, or 44.2 bar,

which puts the value at $414.7 - 44.2 = 370.5$ bar. The thermal conductivity of the solid, 0.2534 $Wm^{-1}K^{-1}$, is then plotted at 370.5 bar. Note that this value is somewhat different from λ_s taken from the same graph but with the assumption of isochoric freezing. The graph of these values for solid and fluid is shown in Figure 4.8. The ratio of thermal conductivities *at the same pressure* is shown in Figure 4.9 as line 'B'. The ratio is almost constant (~ 3.7) at the higher pressures but rises sharply for $P < 500$ bar and probably exceeds 14 as $P \to 0$, if the above assumptions are correct.

Slack [66] has prepared an extensive list of the thermal conductivities of substances at the melting point (including the rare gases, organic and inorganic liquids, and some metals). For a wide range of different materials, the thermal conductivity ratio is ~ 1, except in the notable case of water where it is ~ 4. The ratios for many materials are shown as a function of the normal melting temperature [66, pg. 55] in Figure 4.10, and the unique and divergent behaviour of the "quantum solids" becomes apparent. Elements shown are: open circle, ^4He; filled circle, ^3He; open triangle, H_2; filled triangle, Ne; open square, N_2; filled square, Ar; open inverted triangle, Kr; filled inverted triangle, Xe; open diamond, H_2O.

As a simple definition, the term "quantum solid" is taken to mean that

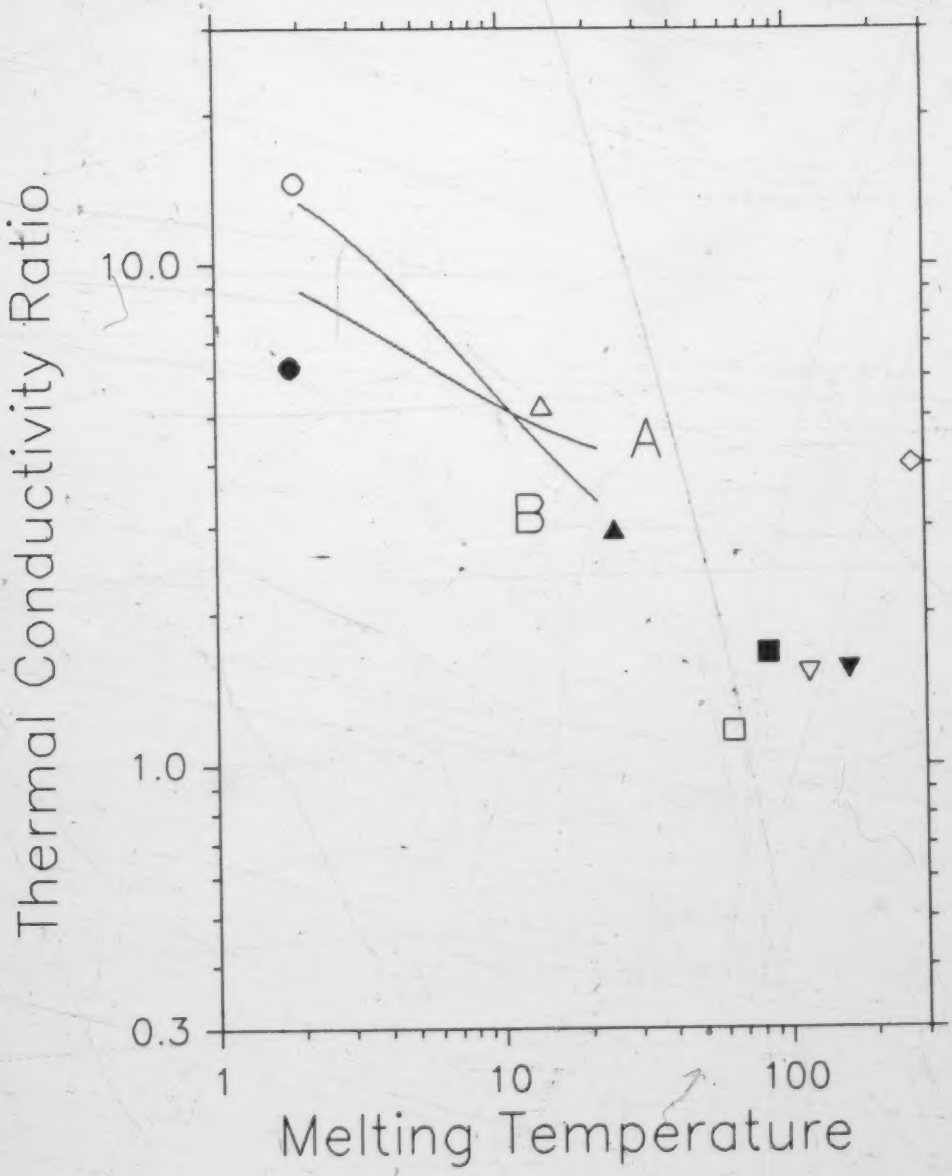

Figure 4.10: β for: ○ ^{4}He; ● ^{3}He; △ H_2; ▲ Ne; □ N_2; ■ Ar; ▽ Kr; ▼ Xe; ◇ H_2O.

small collection of elements whose relatively light atom leads to a dominant kinetic energy term in the Schrödinger Equation. According to the Principle of Corresponding States, all members of a class of substances have the same functional EOS where state parameters such as pressure are expressed in a reduced form. For quantum solids, the EOS is dependent not only on critical point values of pressure, temperature and volume, but the quantum correction factor Λ^* (deBoer [67, 68, 69]) given by:

$$\Lambda^* = \frac{h}{\sigma\sqrt{m\epsilon}} \tag{4.5}$$

where h is Plank's constant, m is the atomic mass, and σ, ϵ are the constants in the two particle interaction potential (see, for example, equation 2.30,- the Lennard-Jones-Devonshire potential). For large values of m ('classical' substances), $\Lambda^* \sim 0$, but for light atomic weight elements Λ^* is large.

There seems to be a relationship between elements with large quantum parameter and the thermal conductivity ratio at melting. This was shown in the article by Slack [66, pg. 53] and may be stated as follows: for elements listed in order of increasing quantum parameter, the *thermal conductivity ratio at the normal melting point increases* (^{3}He is, apparently, an exception). For classical substances, $\Lambda^* \sim 0$ and $\beta \sim 1$. Table 4 lists a series of ele-

Element	Λ^*	β	m.p. (K)	Pressure (bar)
^3He	3.08	6.25	1.82	67.5
^4He	2.67	14.56	1.90	32.6
H_2	1.729	5.24	13.8	0.07
Ne	0.591	2.95	24.5	0.42
N_2	0.225	1.17	63.25	0.12
A	0.187	1.67	83.8	0.67
Kr	0.102	1.52	116.0	0.71
Xe	0.064	1.54	161.3	0.80

Table 4.4: Quantum Parameter and β for various Elements

ments showing their Λ^* value and β for pressures near 1 atmosphere. This data, as well as curves taken from Figure 4.9 and recast for the corresponding range of melting temperatures in the experiment, are shown in Figure 4.10. Clearly, even at elevated pressures, the results for helium adhere to the general trend shown by the other elements. It seems that the speculative assumption leading to the line 'B' (see above) perhaps better reflect this trend, but no definitive conclusion can be drawn.

Referring to the graphs of thermal conductivity of helium (Appendix A), it appears that the curve λ_s for the solid phase could be extrapolated to intersect the curve for the fluid phase at a temperature much higher than the actual melting point. It is as if the trend in λ_s is abruptly cut off at T_{m_s}. It is anticipated for most solids (including helium) that the thermal conductivity decreases with temperature exponentially right up to T_m. At this point, the monotonically increasing phonon-phonon interaction has reached the ultimate value in the solid phase. For most substances, the conductivity of the melt then is not significantly different from the solid, perhaps because the structure of the melt is not itself radically different from the pretransition solid. But this experiment has shown that helium cannot so be described. Slack [66, pg. 54] has pointed out that the melting temperature of 1.9 K for

solid helium at 20.40 $\frac{cm^3}{mole}$ is only 55.6% of the temperature of the intersection between the extrapolated curve for solid and the curve for the fluid, assuming an exponential conductivity dependence (refer to Figure 4.4). Conversely, it may be said that the solid helium has melted *prematurely*,-i. e., before the maximum thermally resistive phonon-phonon interaction was reached.

Perhaps premature melting of helium can be understood on the grounds of the abnormally high value of zero-point energy. It has been pointed out that the zero-point energy in helium is much larger than the latent heat of melting; for example, at a density of 18 $\frac{cm^3}{mole}$, the zero-point energy is about 70 cal/mole, whereas the addition of only 0.49 cal/mole is sufficient to melt the solid [71]. Premature melting might be understood on the grounds that the solid phase contains a remarkably high energy content at zero Kelvin, and melts with a comparatively modest rise in temperature.

Chapter 5

Discussion

5.1 Uncertainties

The overall accuracy of these results is difficult to assess. Other thermal conductivity experiments using the concentric cylinder arrangement have reported quite high accuracy; while these are quite numerous and perhaps too lengthy to report, the modern trend is towards a level on the order of 1% accuracy. In this experiment, the expediency of using a guarded inner cylinder but without recording or controlling the guard cylinder temperatures (as was done, for example, in Ziebland [23]) has limited the degree of precision to which the radial flow of heat could be estimated. This concerns the modified

factor K' (Section 3.5.3) which expresses the degree to which the inner cylinder receives heat from the guard cylinders. The author believes this factor to be accurate to only about 6% since an insufficient number of trials were obtained for its assessment. Indeed, as pointed out in Section 3.5.3, there was some indication that the thermal conductivity values might be low by about 6%. The results for the linearity trials (Section 4.1) are self consistent to within 1.4% (i. e., the st. dev. for a set of 40 separate trials at constant pressure and temperature was 1.4%). The initial data was recorded by the digital instruments and computer system to a high degree of precision, as reported in Section 3.4.1. The uncertainties in the raw data and calculation of the temperature difference between the inner and outer cylinders contribute approximately 2% to the overall results; this rather large value is due to typical temperature differences less than 100 mK. In conclusion, the final values probably have an accuracy not better than 8%.

It is clear that the behaviour of the thermal conductivity of helium at melting is anomalous. For a range of substances spanning diverse categories, the common finding is $1.0 < \beta < 1.5$, as has been mentioned previously. The ratio in helium at 2000 bar is ~ 4.3, and moreover rises dramatically at lower pressures. Although there are uncertainties in the initial readings due

to a lack of knowledge of the longitudinal heat flux in or out of the inner cylinder, they are small when compared with the problem of interpreting the melting point and thermal width from the graphs. Nevertheless, the trend in the thermal conductivities seems above speculation; furthermore the ratio (Figure 4.9), which is derived from these results, would in any case rise steeply at the lower pressures since it is just the ratio of two straight lines with different slopes. Refinement in the shape and functional form of the fitting curves would not contradict the basic finding of this experiment.

5.2 Theory of Dendritic Solidification

With respect to predictions of dendrite theory and the measured parameters in helium[1], the value of β could not, in itself, account for the disparities. Disagreement remains, but the analysis including $\beta = 4$ shows some interesting developments.

The experiments on helium reveal a definitive underlying connection [1] between the undercooling, u, and the growth velocity; in fact, this constitutes one of the clearest points to be shown in the experimental evidence. The

velocity term can be expressed in this form:

$$v = v_o u^{2.7}, \tag{5.1}$$

and the tip radius term is:

$$r_t = r_o u^{-1.35}. \tag{5.2}$$

By elimination of the u dependence, these two equations show that the product of growth velocity and tip radius should be a constant, which for helium has been found by experiment to have the value 2.5 $\times 10^{-8}$cm^3/sec (v_o and r_o are empirical constants):

$$vr_t^2 = const. \tag{5.3}$$

At this point, the experimental evidence for helium and other substances is in general agreement with theoretical predictions in respect of the above relationship. It is also known from many observations of dendritic solidification that, for a given undercooling, the growth velocity and tip radius are fixed. However, the theory only provides a value for the *product* of v and r_t,–i.e., a family of values. This is accomplished through calculation of the Peclet number:

$$Pe = \frac{r_t}{l} = \frac{vr_t}{2D} = p, \tag{5.4}$$

where, in the model due to Langer, the following definition is given:

$$u = pe^{p}E_i(p). \tag{5.5}$$

The $E_i(p)$ term is the exponential integral:

$$E_i(p) = \int_p^{\infty} \frac{e^{-y}\,dy}{y}. \tag{5.6}$$

All theories and experimental evidence on various systems seem to confirm the value of the Peclet number [1].

Clearly, an additional expression involving v and r_t is required in order to distinguish one of the infinite products vr_t. Langer has proposed the "marginal stability hypothesis" to establish the operating point of the dendrite, which states that the dendrite grows at a rate such that the tip is marginally stable against splitting. This concept is expressed quantitatively by σ, the stability criterion, given by the following expression:

$$\sigma = \frac{2Dd_o}{vr_t^2}. \tag{5.7}$$

For values of $\sigma < \sigma^* = 0.025$ (obtained from computer simulations of dendritic solidification), the tip is unstable and tends to break up into a cluster of separate, smaller dendrites, while for $\sigma = \sigma^*$ the dendrite is *marginally*

stable. Langer argues that this defines the operating point of the growth velocity-tip radius combination, and the evidence for succinonitrile and ice seem to support this hypothesis (see [9]). It is interesting to note that if the stability parameter λ_{stab} previously introduced in Chapter 2 is identified with the tip radius r_t in the expression for σ, virtually the same value for σ^* is reached, assuming $\beta = 1$:

$$\sigma = \frac{2Dd_o}{vr_t^2} = \frac{ld_o}{r_t^2}; \tag{5.8}$$

let $\lambda_{stab} = 2\pi\alpha\sqrt{ld_o} = r_t$; then:

$$\sigma = \frac{1}{4\pi^2\alpha^2} = 0.0253 \sim \sigma^*, \tag{5.9}$$

where it is assumed that $\alpha = \sqrt{\frac{1+\beta}{2}} = 1$. Note, in particular, that as β increases, the value of σ decreases.

According to the analysis, σ^* depends on β, but is independent of dynamic quantities r_t or v. Inspired by the Mullins and Sekerka analysis of a directional solidification front, the examination of growth of a sphere deformed by a perturbation proportional to the spherical harmonics $Y(j,m)$ of

order (j, m), gives the following expression for the critical stability criterion:

$$\frac{1}{\sigma^*} = \frac{1}{2} j(j+2)(1+\beta+j^{-1}). \tag{5.10}$$

Here, for $j = 5$ (consistent with the m = 4 modes which are permitted by cubic anisotropy) and $\beta = 1$ we arrive at a value of 0.026 for the critical stability criterion, but as β increases, the value of σ^* decreases.

Dendritic growth in helium was observed for pressures in the range 200 bar to 6500 bar, but the majority of the experiments were conducted above 1100 bar. This implies that the thermal conductivity ratio probably was about 4 for most of these observations. It is significant that σ according to equation (5.9) is material dependent only through β, and for helium with β = 4 assumes the value 0.0101. This is remarkably similiar to the value of σ^* when $\beta = 4$ is substituted in equation (5.10), i.e., $\sigma^*(\beta = 4, j = 6) = 0.0081$. But substitution for the appropriate terms in equation (5.7) for helium leads to a value of 0.0013, which is much smaller than any theoretical figure here. It is not clear whether this observation lends support to equation (5.9). While Langer has set $\beta = 1$ ('symmetric model'), the above observations suggest that σ^* is not a universal constant, but is material dependent for substances having $\beta > 1$ (e.g., ^4He, H_2O).

The results in the case of succinonitrile (SCN)[9] are consistent with the value $\sigma = 0.0195$, which is favourable to the theory; a graph of v_n versus u for both SCN and ice [9] shows excellent agreement with a theoretical curve calculated on the basis of $\sigma = 0.025$.

Figure 5.1 is a graphical representation of equation (5.10), showing the stability criterion σ^* as a function of β and assuming j = 6. Theoretical values for σ near 0.025 are confirmed only at *lower* values of β, even suggesting $\beta < 1$! It was pointed out earlier in Section 2.2 that the most probable side-arm spacing parameter λ_{stab}, according to theoretical predictions (including the assumption that $\beta = 7.25$ [1]), was in fact about 25 times smaller than that found experimentally. The spacing parameter, λ_{stab}, is proportional to $\sqrt{1+\beta}$, so improvement can only be realised if β is much larger. However, as just indicated, agreement in terms of σ^* is achieved at *lower* values. Perhaps part of the problem here is that the model is concerned with a *free* dendritic crystal, whereas all of the qualitative data were obtained for helium dendrites attached and growing outwards from the cell wall (i.e., as an example of directional solidification).

Substitution of the appropriate values for helium in the expression for σ gives a value of 0.0013,- much smaller than predicted,- which may be due in

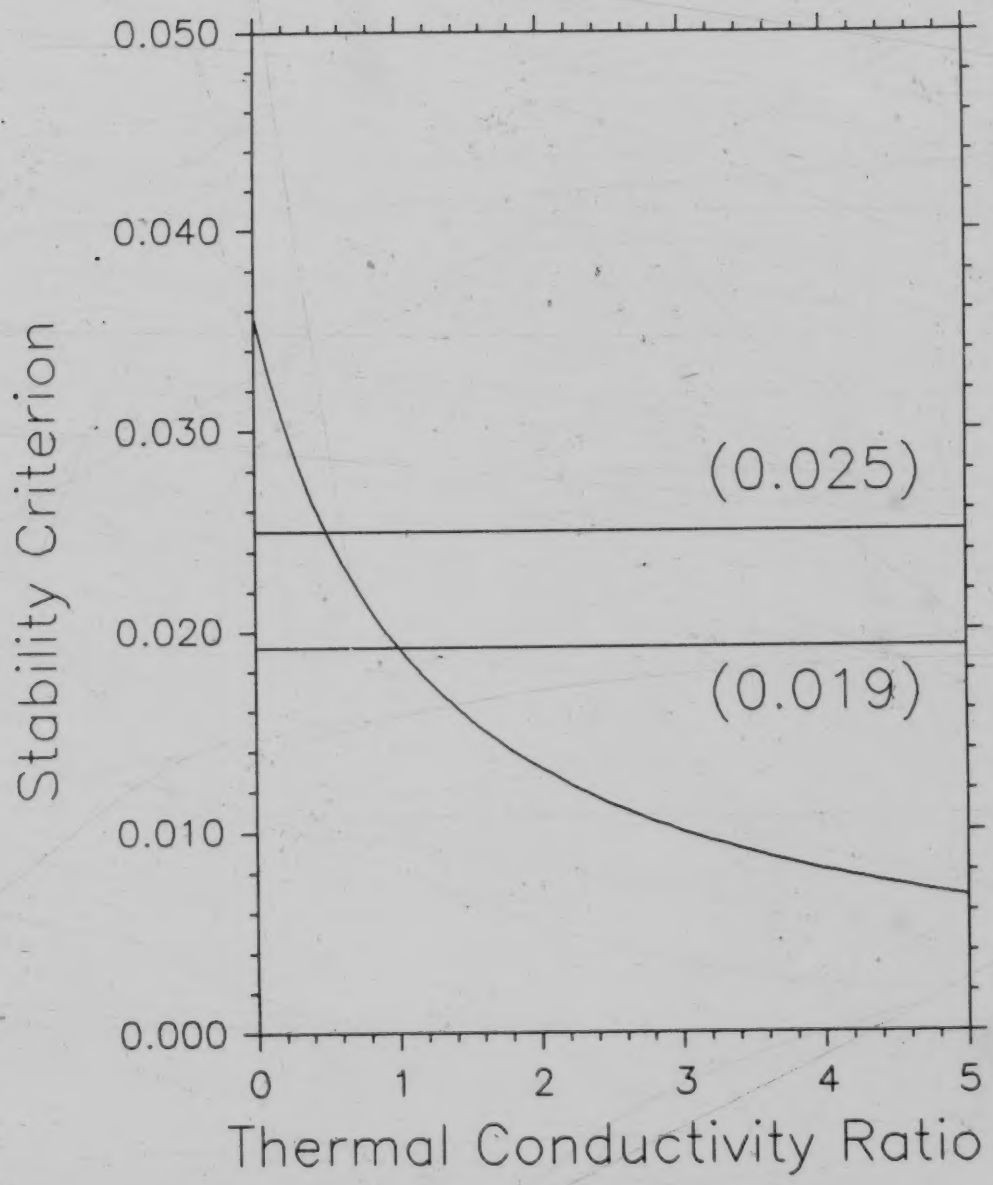

Figure 5.1: σ^* as a function of β according to equation (5.10)

part to the anomalously high value of β. With regard to the dendrite spacing parameter, λ_{stab}, the experimental values for helium are much larger (by a factor of 25) than those predicted by equation (2.20). The growth velocities, however are about 40 times smaller than predicted, but the dependence on undercooling appears to adhere to the anticipated functional form, i. e., $v \propto u^n$, where $n = 2.21$ in the "modified Ivantsov" theory [43], $n = 2.65$ in the theories of Trivedi [44] and Nash and Glicksman [45].

In conclusion, it seems that dendritic solidification in pure helium qualitatively obeys some of the principle relationships derived in the model due to Langer and others, but numerical agreement is not good. In this thesis, it has been shown that $\beta > 4$ for the range of pressures and temperatures in which dendrites have been observed, and that β increases as the pressure decreases. Nevertheless, values in this range are insufficiently large to account for the large discrepancy between observed and predicted side-arm spacing. It seems much more experimental and theoretical work needs to be done on this subject.

5.3 Thermal Conductivity Peak in Transition Phase

An unexpected feature of the graphs is the sharp peak in thermal conductivity within the transition region (mixed phase). This can be most clearly seen in Figures A.8 (trial 4.), A.10 (trial 5a.), A.12 (trial 5b.), A.14 (trial 6.), and A.16 (trial 7.). In trials that were able to scan the transition completely the curve shows first a gradual flattening below the transition region, then the sharp peak and an abrupt drop to the upper melting point (T_{mf},-liquidus point), then the slowly rising values in the fluid phase. The trials were most often obtained as the sample cooled through the transition; therefore, it is impossible to speculate about hysteresis. It may be that the peak is due at least in part to the latent heat of fusion given up at solidification. A formal analysis would begin by assuming that the annular gap between concentric cylinders was filled with coexisting layers of solid and fluid; the thermal conductivity and thermal gradient across each layer, the latent heat of solidification of helium at given density and pressure, and possibly Kapitza thermal resistance across the boundary would have to be included. At the moment, no satisfactory explanation can be given for the effects noted in

various trials.

5.4 Comparison with Theories of the Dense Gas and Fluids

The thermal conductivity of a dense gas of hard spheres has been calculated on the basis of the Modified Enskog Theory (MET) (see section 2.3.1). These values are shown in comparison with the results of this experiment in Appendix B, where the data have been recast in the form of λ_f as a function of molar volume (in $\frac{cm^3}{mole}$) for each trial, except No. 5b due to an error in recording pressure for that trial. As well, theoretical values of thermal conductivity on the basis of the MET using a Lennard-Jones interaction potential (equation (2.25)) have been calculated, based on the Hanson and Ree equation of state (HREOS)[53]:

$$\frac{p}{\rho k_B T} = \frac{p_{rep}}{\rho k_B T} - \left[\frac{1}{T^*}\right]^{\frac{1}{2}} \sum_{i=1}^{5} iC_i x^i + \left[\frac{1}{T^*}\right] \sum_{i=1}^{5} D_i x^i, \tag{5.11}$$

where:

$$\frac{p_{rep}}{\rho k_B T} = 1 + B_1 x + B_2 x^2 + B_3 x^3 + B_4 x^4 + B_{10} x^{10}, \tag{5.12}$$

and $x = \rho^*/T^{*\frac{1}{4}}$, $\rho^* = \rho\sigma^3$, and $T^* = k_B T/\epsilon$. ρ is the particle number density. The first term on the R.H.S. of equation (5.11) corresponds to the repulsive part only of the interaction, while the other two terms handle the attractive part. It is possible to calculate the thermal conductivity of an L-J fluid using the same dilute gas value as defined in Chapter 2:

$$\lambda = \lambda^0 b_o \rho \left[y^{-1} + 1.2 + 0.755y \right], \tag{5.13}$$

where:

$$\frac{p}{\rho k_B T} = 1 + y. \tag{5.14}$$

y is a measure of the deviation from ideal gas behaviour, and is more accurately expressed by replacing the pressure term p with the 'thermal pressure' $T(\partial p/\partial T)_V$:

$$y = \frac{1}{\rho k_B} \left[\frac{\partial p}{\partial T} \right]_V - 1. \tag{5.15}$$

Constants B_i, C_i, D_i appearing in the above equations are provided by Ree [53].

From the graphs of these calculations and the experimental values (Appendix B), it can be seen that the hard-sphere model appears to reflect the

shape of the thermal conductivity curves but the theoretical values are everywhere higher by a factor ranging from about 30% at the lowest pressure to about 75% in the 2 kbar trial (No. 7). Agreement both in shape and in numerical value becomes worse at the higher pressures.

The theoretical curves based on the HREOS, which has been shown to agree extremely well for ^{4}He at pressures between 1 kbar and 8 kbar at 298 K [48], do not seem to reflect the data of this experiment very well.

The thermal conductivity in the existence range of fluid alone is shown in Appendix C for the trials. Calculated values of the thermal conductivity of fluid due to McCarty [15] are shown along with experimental results for trials at comparable pressures in Figures C.1 and C.3. The theoretical data was extracted from the published table for the isobars at 500 bar and 1000 bar; these are shown along with trials at P_{init} of 486.1 bar and 954.9 bar. The theoretical data was calculated with an empirical relation (equation (5.21)) using the results of Golubev [36] and Kerrisk [64] in order to determine fitting constants:

$$\lambda_f = \lambda_o(T)\lambda_v(\rho, T) + \lambda_c(\rho, T), \qquad (5.16)$$

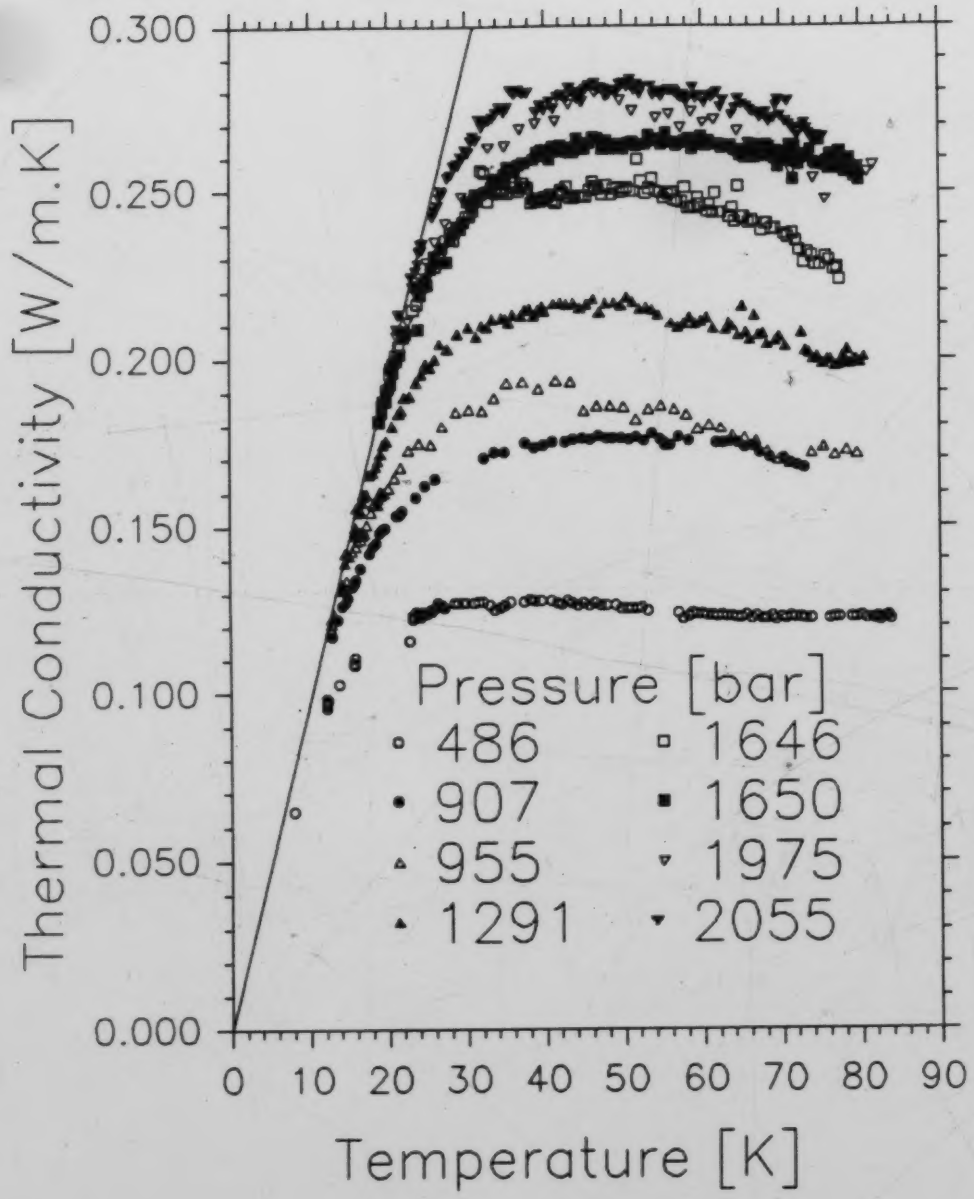

Figure 5.2: Thermal Conductivity of Fluid ^{4}He along isobars

where $\lambda_o(T)$ is the dilute gas limit, $\lambda_y(\rho, T)$ corrects the dilute gas values for increasing density and $\lambda_c(\rho, T)$ is the enhancement in the vicinity of the critical point. In general, it seems that while the values at intermediate temperatures are reasonable, agreement with the experimental values at the lower temperatures is poor, and becomes much worse in the vicinity of the melting line.

The graphs of thermal conductivity of the fluid are also reproduced on a single graph in Figure 5.2. Each curve has the same overall shape: a steep rise in values immediately above the melting point which achieves a broad plateau that then gradually falls. This behaviour is reminiscent of the shape of the specific heat curve for fluid helium reported in the NBS publication of 1972 [15]; shown in Figure 5.4 are the 507 bar and 1013 bar isobars of C_v per unit mass of the fluid over the appropriate temperature range. Since these curves lie very close together, an expanded view is provided in Figure 5.5 (same data). Included in these figures are two curves of recast experimental data derived from Dugdale and Franck [72] (open triangles, 500 bar isobar; filled triangles, 1000 bar isobar). The original experimental curves were in the form of isochores as functions of temperature; from this data, an intermediate graph of the isochores as functions of pressure was prepared,

shown in Figure 5.3; extraction of values for the 500 bar and 1000 bar isobars was accomplished by graphical interpolation between two isochores that fortuitously straddled vertical isobar lines at 500 and 1000 bar. The values obtained in this manner cannot be very accurate (especially near the maximum specific heat values for the 500 bar isobar), but give a suggestion or impression of the behaviour.

The comparison of thermal conductivity curves with these specific heat curves is motivated by the theory of Horrocks and McLaughlin [54], who have provided an expression for the thermal conductivity of a fluid that is dependent on the specific heat per molecule at constant volume:

$$\lambda_l = \frac{\sqrt{2}\nu C_v}{a} \tag{5.17}$$

where C_v is the specific heat at constant volume per molecule, ν is the vibrational frequency of an atom confined within the cell formed by its nearest neighbours, and a is the nearest neighbour distance. The model assumes C_v=3$\mathbf{k}_B$ as a constant for the liquid, and interest has been focussed on the problem of determining ν on the basis of assumptions about the interaction potential (e. g., the harmonic oscillator approximation, expressed in equa-

tion (2.39)). However, as shown by Figures 5.4 and 5.5, the specific heat of the liquid is *not* constant in the temperature regime relevant to this experiment. It may therefore be concluded that the experimental data presented here lend strong support to the liquid models of Horrocks and McLaughlin at intermediate temperatures, i. e., for 20 K < T < 80 K.

From Figure 5.2 it is evident that the fluid thermal conductivity values immediately above melting lie along a common curve, shown in the figure as the solid line which extrapolates to 0 K. The slope of the line as shown is given by $\alpha = 0.0097\ Wm^{-1}K^{-2}$, so we may speculate:

$$\lambda_f = \alpha \times T, \tag{5.18}$$

valid for each isobar in the vicinity of the melting point. It is as if there were a 'universal' thermal conductivity curve of nearly constant shape which was shifted along the common line by some pressure-dependent factor. Along the common line the thermal conductivity is dependent only on temperature; a specific trial departs from this common line at some pressure-dependent point. A speculative means by which the 'universal' curve is shifted along the common curve will be introduced in a subsequent paragraph.

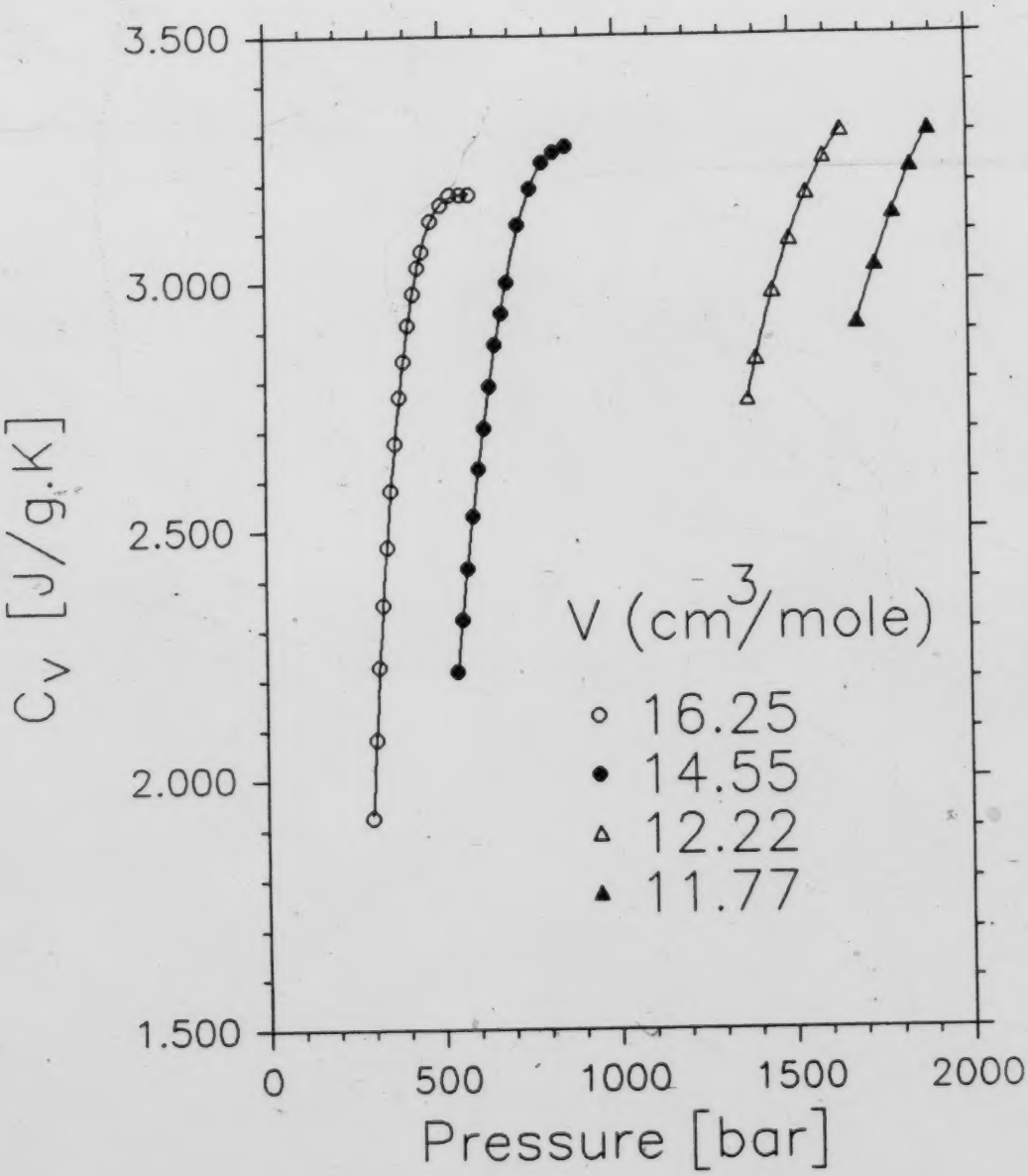

Figure 5.3: Specific Heat of ^{4}He along isochores

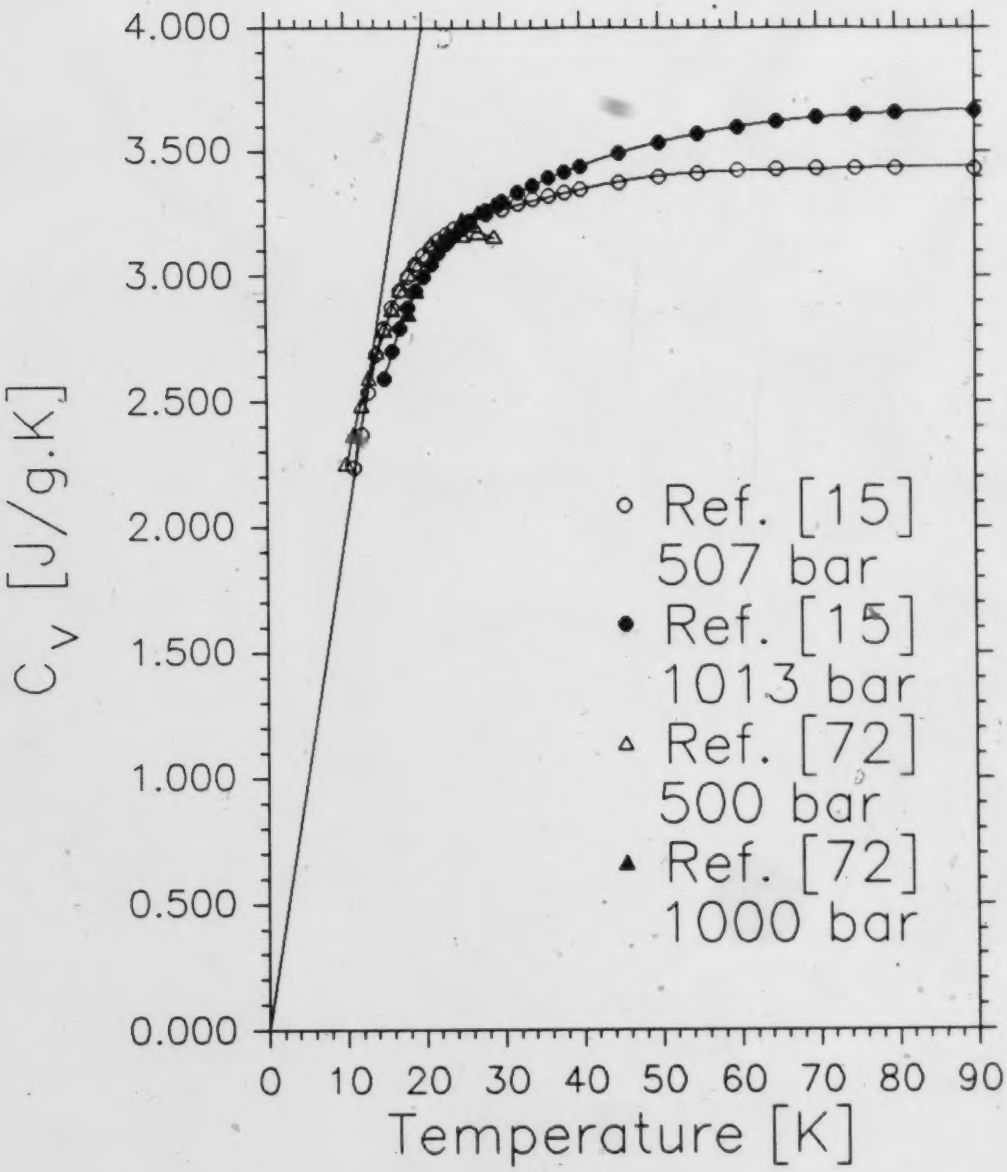

Figure 5.4: Specific Heat of ^{4}He along specified isobars (the straight line passes through T = 0 K and C_V = 0 $Jg^{-1}K^{-1}$)

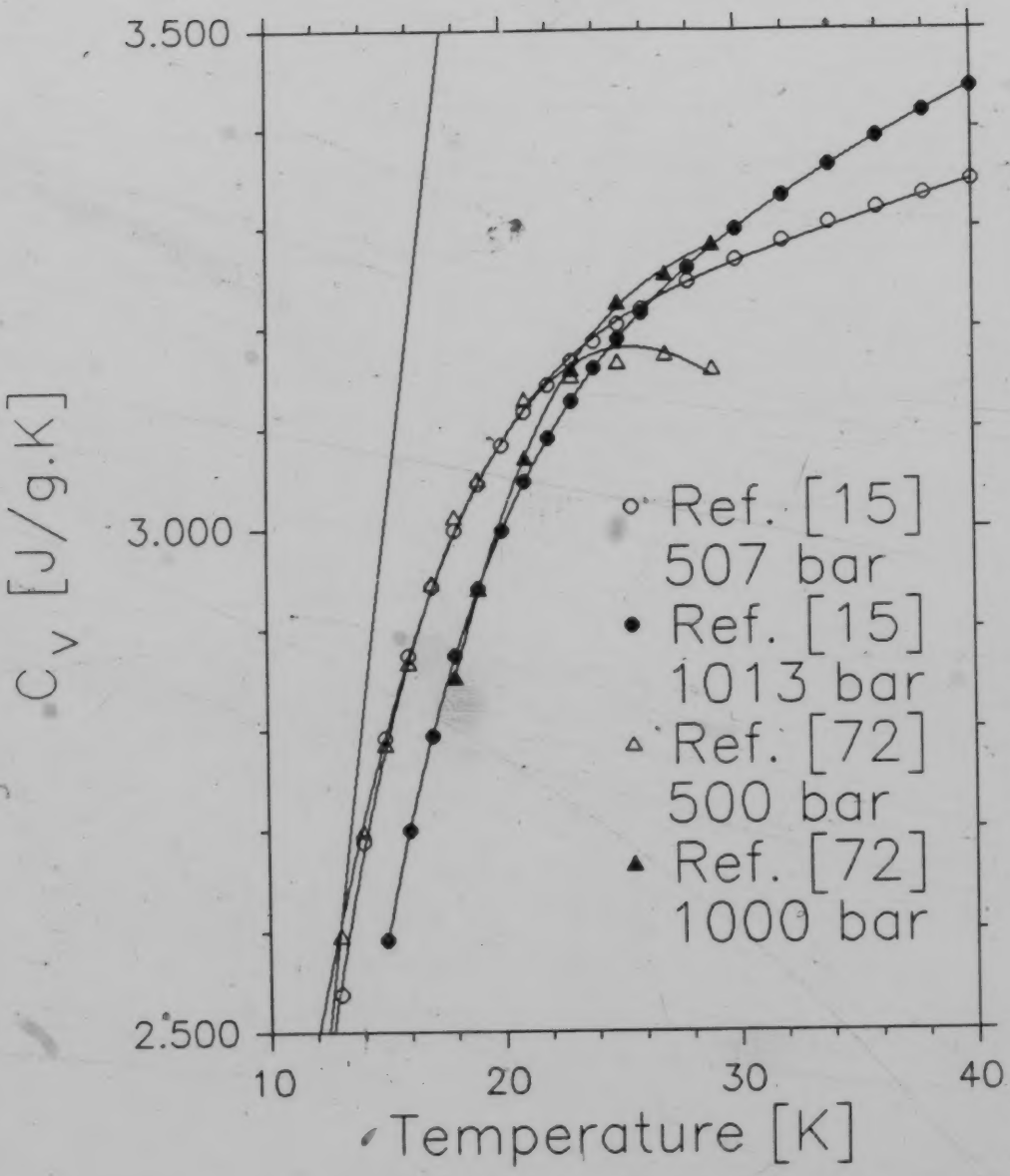

Figure 5.5: Specific Heat of ^{4}He along specified isobars (expanded view of Figure 5.4)

A similiar interpretation may be applied to the specific heat for fluid, shown in Figure 5.4. It seems that a straight line passing through 0 K would also reasonably represent the *low temperature* data and theoretical curve, since near the melting point, the curves for both the 500 bar and 1000 bar isobars lie very close together. Again, we may speculate:

$$C_V = \gamma \times T, \tag{5.19}$$

where $\gamma = 0.2\ (W \cdot s)g^{-1}K^{-2}$. A typical molar volume of 12.50 cm^3/mole corresponds to a nearest-neighbour distance 'a' of approximately 3.1 Å. If this value is inserted in equation (5.11) along with the above expressions for λ_f and C_V, which together eliminate the temperature dependence, we are left with an estimate for the vibrational frequency ν:

$$\nu = \frac{\alpha a}{\gamma\sqrt{2}} = 1.59 \times 10^{12} Hz. \tag{5.20}$$

This will be recognised as a typical phonon vibrational frequency. Horrocks and McLaughlin have provided two means by which ν may be calculated, based on a hard-sphere model and a harmonic oscillator model. These are, respectively, given by:

$$\nu_{HS} = \sqrt{\frac{8k_BT}{\pi m}}\left[\frac{1}{4(a-\sigma)}\right], \tag{5.21}$$

and

$$\nu_{HO} = \frac{1}{2\pi\sqrt{m}}\left[\frac{2Z\epsilon}{a^2}(Lv^{*4} - Mv^{*2})\right]^{\frac{1}{2}}, \tag{5.22}$$

where the various terms have their usual definitions or have previously been defined in Section 2.3.2. Insertion of the appropriate values gives the following results: $\nu_{HS} = 1.60 \times 10^{12}$ Hz at 20 K, while $\nu_{HO} = 0.64 \times 10^{12}$ Hz. These values compare favourably with that obtained above from equation (5.11).

Another model, based on the kinetic theory of thermal conductivity of gases, also suggests a dependence on the specific heat, assuming that the heat current in the liquid is carried by phonons. The model assumes for convenience that phonon wave-packets in the fluid can be regarded just like the particles of a gas, with similiar equations for mean free path, dispersion, and thermal conductivity (see equation (2.38) in Chapter 2). This model has already shown wide applicability for dielectric solids. Phonon dispersion curves due to neutron scattering have been obtained for liquids [73], although only longitudinal modes are observable. Neglecting diffusive transport and including only the vibrational modes, the theoretical thermal conductivity is

given by:

$$\lambda_l = \frac{v l \rho C_v}{3M} \tag{5.23}$$

where v is the sound velocity, l is the mean free path of a phonon, C_v is the specific heat at constant volume per mole, and M is the molecular mass. It has been shown that the speed of sound is relatively constant as a function of temperature in the liquid at pressures up to 70 bar [74], and, if the assumption that l is also relatively constant is valid, the dependence on specific heat is clear. This seems to be strongly supported by the results of this experiment.

This equation may also provide a clue as to the means by which the 'universal' thermal conductivity curve is shifted along the common curve as a function of pressure. The *shape* of the thermal conductivity curve for each trial seems to be determined by that of the specific heat function, but the *placement* of the curve is determined by the pressure. In equation (5.17), the only terms which are pressure-dependent are v (speed of sound), l (mean free path between collisions), and ρ (density). As can be seen in Figure 5.4, the calculated specific heat apparently is not strongly dependent on the pressure, there being only a 7% difference between the 507 bar and 1013 bar curves at 90 K. It is known that v and ρ increase with increasing pressure at constant

temperature. Since the fluid state lacks long-range order, it is to be expected that the mean free path between collisions (phonons) would be quite small, and probably of the order of the nearest neighbour distance, $a = (\sqrt{2}\tilde{V}/N)^{\frac{1}{3}}$; the magnitude of this term, however, decreases as the pressure increases. Therefore, it would be of interest to examine the behaviour of the product $Z = v \cdot \rho \cdot a$ as a function of pressure at constant temperature.

The graph of Z for two isotherms at 20 K and 75 K over the pressure range 0 to 1000 bar is shown in Figure 5.6, from data extracted from the NBS report (1972) [15]. The response of this function is nearly linear in the pressure, especially at higher temperatures and pressures; hence: the thermal conductivity of fluid helium seems to be very well represented by this model, equation (5.17), derived from simple kinetic theory.

Nevertheless, it is possible to combine the results of the previous analysis concerning equation (5.11) with this model. It was noted above that both the thermal conductivity and the specific heat are linear functions of the temperature at the lower temperatures, and that these linear portions for various pressures overlap on common straight-line curves.

The validity of the kinetic model (equation (5.17)) can be checked by inserting the empirical relationships for λ_f and C_V and assuming, as before,

that $l = a$:

$$\lambda_f = \alpha \times T = \left[\frac{1}{3M}\right][v\rho l]C_V \tag{5.24}$$

$$\alpha \times T \approx \left[\frac{1}{3M}\right][v\rho a](\gamma \times T), \tag{5.25}$$

hence:

$$\frac{\alpha}{\gamma} \sim \left[\frac{1}{3M}\right] Z, \tag{5.26}$$

or:

$$\text{L.H.S.} = 4.84 \times 10^{-5}\,\frac{kg}{m \cdot s} \stackrel{?}{=} 2.77 \times 10^{-5}\,\frac{kg}{m \cdot s} = \text{R.H.S.},$$

where the value Z = 8.304 $\times 10^{-5}\,\frac{kg}{m \cdot s}$ has been chosen, corresponding to fluid at 20 K and 507 bar.

However, the foregoing included the assumption that the mean free path, l, was equal to the nearest neighbour distance, a. The L.H.S. = R.H.S. if l = 1.75 a, a reasonable possibility for the fluid state.

The question remains concerning the behaviour of the fluid specific heat, in particular, the steep decline at lower temperatures near the melting point. This has already been addressed by Franck [72]. The room temperature limit of the specific heat of the fluid has the value $C_v = \frac{3}{2}R$, which is just the specific heat of an ideal, monatomic gas (C_v = 3.116 $Jg^{-1}K^{-1}$ for ^4He), not

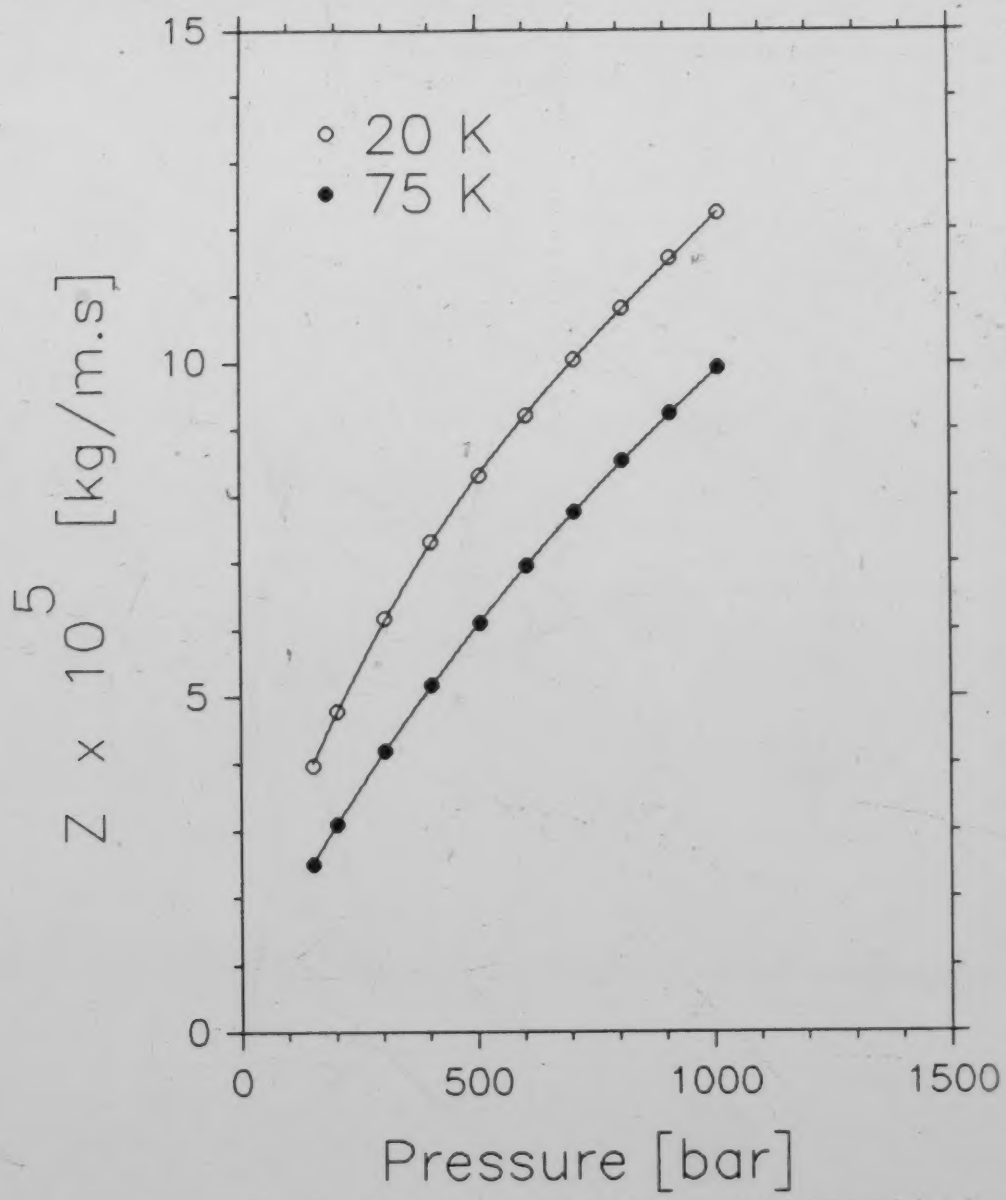

Figure 5.6: Graph of $Z = v \cdot \rho \cdot a$ as a function of pressure

to be confused with the law of Dulong-Petit ($C_v = 3R$) for the specific heat of solids. At lower temperatures, the decline is due to quantum effects which may be elucidated by the following simple explanation: each atom of the fluid is assumed to be confined by its nearest neighbours in a unit cell, which can be likened to the familiar 'particle in a box'. The quantised energy levels in this system are closely spaced at the higher energies (corresponding to higher temperatures), which results in the classical limit of the specific heat. At lower temperatures, the available energy levels are more widely spaced, and when $\hbar\omega \sim kT$, the specific heat will begin to diminish. It would be necessary to know the exact nature of the potential within the unit cell (e.g., free particle with hard-sphere boundary) in order to construct a theoretical model. However, quantum calculations of the specific heat of H_2, D_2 and Ar [75] based on this simple picture have shown a decline at lower temperatures.

5.5 Proposals

In retrospect, it is evident that changes to the experimental arrangement would facilitate more precise results and simplify the interpretation of data. If the high pressure capillary leading to the cell were to be maintained per-

manently *unblocked*, and if a comparatively large excess volume of supply gas were incorporated into the charging system, all trials could effectively be run at constant pressure which would more realistically mimic the experimental conditions during dendritic growth. This would also avoid the problem of interpretation of critical factors such as T_{ms} and T_{mf}, since an isobar intersects the melting line at a *single* temperature (T_m) and pressure (P_m); there would, however, be a molar volume change during such a process. To address the central difficulty in the present design, namely, the deficient understanding of longitudinal heat flux in or out of the inner cylinder, each guard cylinder ought to be monitored separately and as well have a separately controlled heater to fix the heat flux at zero. For the sake of simplicity, this feature was dropped from the original design of the measuring system.

5.6 Conclusions

The results of this experiment constitute the first record of: (1) the thermal conductivity of fluid ^{4}He in the regime 450 bar $< P <$ 2050 bar, and 20 K $<$ T $<$ 80 K; and (2) the thermal conductivity ratio of solid and fluid ^{4}He in the *same* apparatus for the melting curve between 8 K and 20 K.

The results of this experiment have shown:

1. liquid structure models based on the theory of Horrocks and McLaughlin [54] are confirmed and that the thermal conductivity is largely determined by the specific heat at constant volume

2. the pressure dependence of the thermal conductivity coefficient is also well represented by a model derived from simple kinetic theory (equation (5.17))

3. the Enskog theory for heat transport in a Lennard-Jones fluid, which agrees well with experimental thermal conductivity data for helium at high pressures at room temperature, is a poor model at intermediate temperatures (20 K < T < 80 K) for ^{4}He

4. tabulated values of the thermal conductivity coefficient in McCarty [15] are *not*, in general, reliable near the melting point

5. the thermal conductivity ratio ($\beta = \lambda_s/\lambda_f$) at melting is anomalously high ($\beta > 4$ at 2000 bar, and increases with decreasing melting pressure)

6. the value of β for ^{4}He agrees with the trend in β for the other quantum solids,–i. e., β increases with increasing quantum parameter Λ^*,-

-signifying that the premature melting of helium is due to quantum effects

Chapter 6

Bibliography

The format of bibliography items is as follows:

1. Name(s) of the Author(s)
2. Title of Journal or Book
3. Date of Publication (year)
4. Volume Number (boldface print)
5. Page Number (beginning of article)

Bibliography

[1] Franck, J. P., and J. Jung, J. Low Temp. Phys., 1986, **64**,165

[2] Franck, J. P., and J. Jung, J. Low Temp. Phys., 1987, **65**, 1

[3] Mullins, W. W., and R. F. Sekerka, J. Appl. Phys., 1963, **34**, 323

[4] Mullins, W. W., and R. F. Sekerka, J. Appl. Phys., 1964, **35**, 444

[5] Debye, P., Vorträge über die kinetische Theorie der Materie und der Electrizität (Berlin), 1914

[6] Peierls, P., Ann. Phys.(5), 1929, **3**, 1055

[7] Berman, R., F. E. Simon, and J. M. Ziman, Proc. Roy. Soc. A, 1953, **220**, 171

[8] Berman, R., E. L. Foster, and J. M. Ziman, Proc. Roy. Soc. A, 1955, **231**, 130

[9] Langer, J. S., Rev. Mod. Phys., 1980, **52**, 1

[10] Laxmanan, V., Acta. Metall., 1985, **33**, 1023

[11] Laxmanan, V., Acta. Metall., 1985, **33**, 1036

[12] Libchaber, A., in "Nonlinear Phenomena in Physics", ed. F. Claro, Springer-Verlag (Berlin), 1984

[13] Glicksman, M. E., R. J. Schaefer, and J. D. Ayers, Metall. Trans., 1976, **A 7**, 1747

[14] Fujioka, T., Ph. D. Thesis, 1978, Carnegie-Mellon University

[15] McCarty, R. D., NBS Tech. Note 631, 1972

[16] Ashcroft, N. W., and N. D. Mermin, "Solid State Physics", Holt, Reinhart and Winston, 1976, chpt. 25

[17] Herring, C., Phys. Rev., 1954, **95**, 954

[18] Kittel, C., and H. Kroemer, "Thermal Physics" (2nd. ed.), 1980, chpt. 14

[19] Ziman, J. M., "Electrons and Phonons", Oxford, 1960, chpt. VIII

[20] Thatcher, P. D., Phys. Rev., 1967, **156**, 975

[21] Tye, R. P. (ed.), "Thermal Conductivity" Vol. 2, Academic, 1969, chpt. 2

[22] Roder, H. M., J. Research (NBS), 1981, **86**, 457

[23] Ziebland, H. and J. T. A. Burton, Int. J. Heat Mass Transfer, 1960, **1**, 242

[24] Tufeu, R., D. Vital, et. al., High Temp. High Press., 1979, **11**, 587

[25] Liedenfrost, W., High Temp. High Press., 1979, **11**, 561

[26] Shrock, V. E., and E. S. Starkman, Rev. Sci. Instr., 1958, **29**, 625

[27] Poltz, H., Int. J. Heat Mass Transfer, 1965, **8**, 609

[28] Sengers, J. V., Ph. D. Thesis, Amsterdam, 1962

[29] Carslaw, H. S., J. C. Jaeger, "Conduction of Heat in Solids" (2nd. ed.), Oxford, 1959, pp. 510

[30] van Itterbeek, A. (ed.), "Physics of High Pressure and the Condensed Phase", Wiley, 1965

[31] Tsiklis, D., "Handbook of Techniques in High Pressure Research and Engineering", (Russian), Plenum Press, 1968, (Bobrowsky, A., trans.)

[32] Sparks, L. L., and R. L. Powell, J. Research A (NBS), 1972, **76A**, 263

[33] Weiss, J. D., and D. Lazarus, Phys. Rev. B., 1974, **10**,456

[34] Bartholin, H., D. Bloch, and F. Chaissé, C. R. Acad. Sc. Paris (Series B), 1969, **t. 269**, 467

[35] Locatelli, M., D. Arnaud, and M. Routin, Cryogenics, 1976, **16**, 374

[36] Golubev, I. F., and I. B. Shpagina, Gaz. Prom., 1966, **11**, 40

[37] Seward, W. D., D. Lazarus, and S. C. Fain, Phys. Rev., 1969, **178**, 345

[38] Bertman, B., H. A. Fairbank, C. W. White, and M. J. Crooks, Phys. Rev., 1966, **142**, 74

[39] Webb, F. J., K. R. Wilkinson, and J. Wilks, Proc. Roy. Soc., 1952, **A214**, 546

[40] Golubev. I. F., Teploenergetika, 1963, **10**, 78

[41] Itskevich, E. S., et. al., Instrum. Exp. Tech. (USSR), 1966, **6**, 1452

[42] Berman, R., E. L. Foster, and H. M. Rosenberg, Brit. J. Appl. Phys., 1955, Vol. 6(5), 181

[43] Ivantsov, G. P., Dokl. Akad. Nauk. (USSR), 1947, **58**, 567

[44] Trivedi, R., Acta. Metall., 1970, **18**, 287

[45] Nash, G. E., and M. E. Glicksman, Acta. Metall., 1974, **22**, 1283

[46] Chapman, S., and T. G. Cowling, "The Mathematical Theory of Non-Uniform Gases", 1939, Cambridge University Press

[47] Hirschfelder, J. O., C. F. Curtis, and R. B. Bird, "Molecular Theory of Gases and Liquids", Wiley, 1954

[48] Abdelazim, M. S., High Temp. High Press., 1990, **20**, 193

[49] LeNeindre, B., Y. Garrabos, and R. Tufeu, Physica A, 1989, **156**, 512

[50] Acton, A. and K. Kellner, Physica B, 1977, **90**, 192

[51] Nelson, E. H., and J. P. Franck, Physica B, 1991, **169**, 553

[52] Kestin, J., K. Knierim, E. A. Mason, B. Najafi, S. T. Ro, and W. A. Wakeman, J. Phys. Chem. Ref. Data, 1984, **13**, 229

[53] Ree, F., J. Chem. Phys., 1980, **73**, 5401

[54] Horrocks, J. K., and E. McLaughlin, Trans. Faraday Soc., 1960, **56**,206

[55] Horrocks, J. K., and E. McLaughlin, Trans. Faraday Soc., 1963b, **59**, 1709

[56] Grilly, E. R., and R. L. Mills, Ann. Phys., 1959, **8**, 1

[57] Mills, R. L., D. H. Liebenberg, and J. C. Bronson, Phys. Rev. B, 1980, **21**, 5137

[58] Metcalf, G. P. and R. P. Behringer, J. Low Temp. Phys., 1990, **78**, 231

[59] Benedict, M., J. Am. Chem. Soc., 1937, **59**, 2233

[60] Driessen, A., E. van der Poll, and I. F. Silvera, Phys. Rev. B, 1986, **33**, 3269

[61] Krause, J. K., and C. A. Swenson, Cryogenics, 1976, **16**, 413

[62] Crawford, R. K., and W. B. Daniels, J. Chem. Phys., 1971, **55**, 5651

[63] Bertman, B., H. A. Fairbank, C. W. White, and M. J. Crooks, Phys. Rev., 1966, **142**, 74

[64] Kerrisk, J. F., and W. E. Keller, Phys. Rev., 1968, **177**, 341

[65] Berman, R., C. R. Day, D. P. Goulder, and J. E. Vos, J. Phys. C, 1973, **6**, 2119

[66] Slack, G. E., "Thermal Conductivity of Nonmetallic Crystals", in: "Solid State Physics" Vol. 34, 1979, H. Ehrenreich, F. Seitz, and D. Turnbull (ed.)

[67] DeBoer, J., Physica, 1948, **14**, 139

[68] DeBoer, J., and B. S. Blaisse, Physica, 1948, **14**, 149

[69] DeBoer, J., and R. J. Lunbeck, Physica, 1948, **14**, 520

[70] Wilks, J., "The Properties of Liquid and Solid Helium", 1967, Oxford University Press

[71] Domb, C., and J. S. Dugdale, Prog. Low Temp. Phys, 1957, **2**, 338

[72] Dugdale, J. S., and J. P. Franck, Phil. Trans. Roy. Soc. (London), 1964, **A275**, 1

[73] Henshaw, D. G., and A. D. B. Woods, Phys. Rev., 1961, **121**, 1266

[74] Atkins, K. R., and R. A. Stasior, Can. J. Phys., 1953, **31**, 1156

[75] Levelt, J. M. H., and R. P. Hurst, J. Chem. Phys., 1960, **32**, 96

Appendix A

Graphs of the Raw Data

Trial No.	T_{mf} (K)	Whole Data	Transition Region	MET comparison	Fluid only
1.	8.0	A.1	A.2	B.1	C.1
2.	10.3	A.3	A.4	B.2	C.2
3.	12.00	A.5	A.6	B.3	C.3
4.	14.00	A.7	A.8	B.4	C.4
5a.	18.90	A.9	A.10	B.5	C.5
5b.	18.90	A.11	A.12	N/A	C.6
6.	20.90	A.13	A.14	B.6	C.7
7.	21.05	A.15	A.16	B.7	C.8

Table A.1: Raw data graph Locator

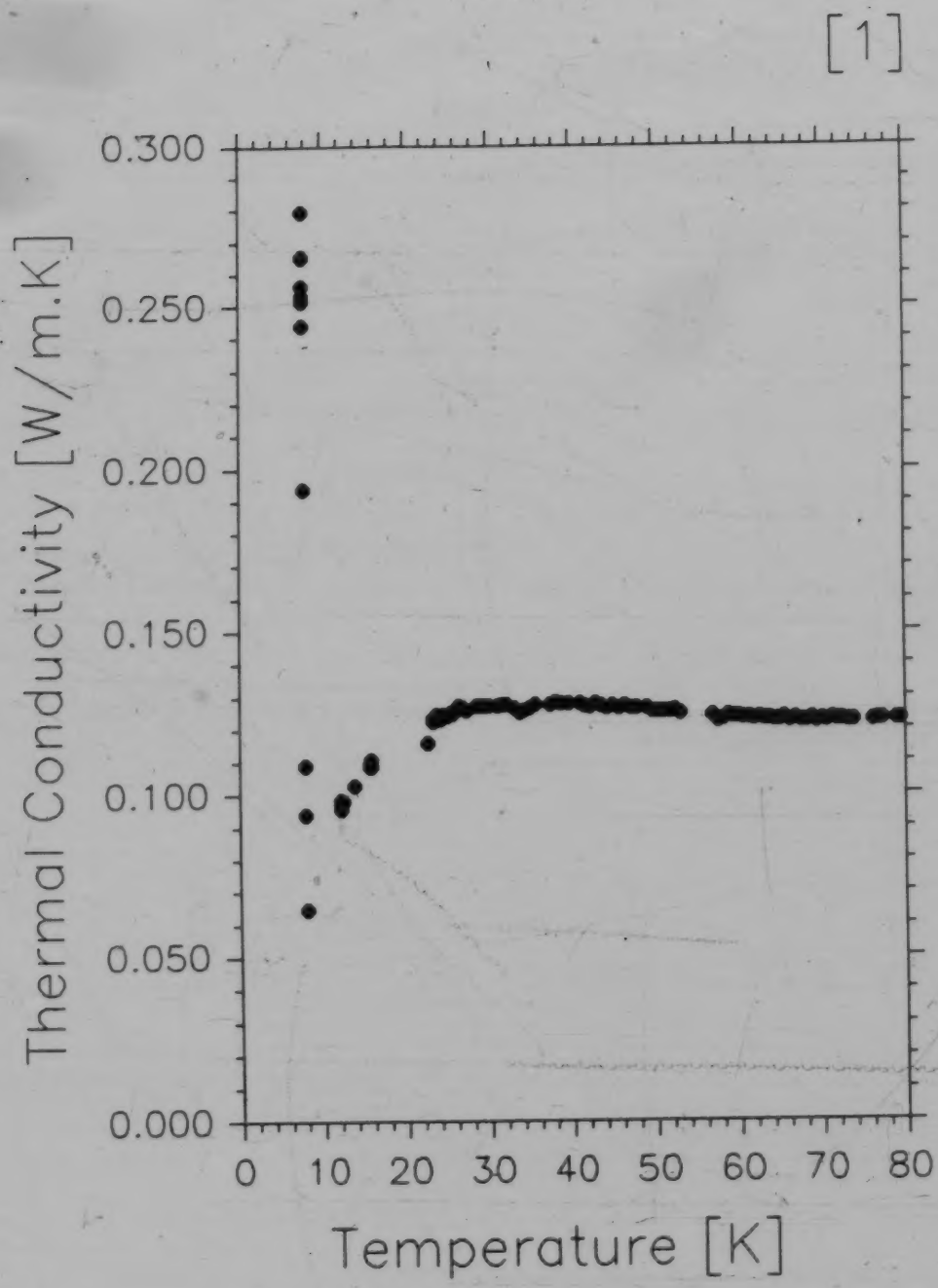

Figure A.1: Trial No. 1

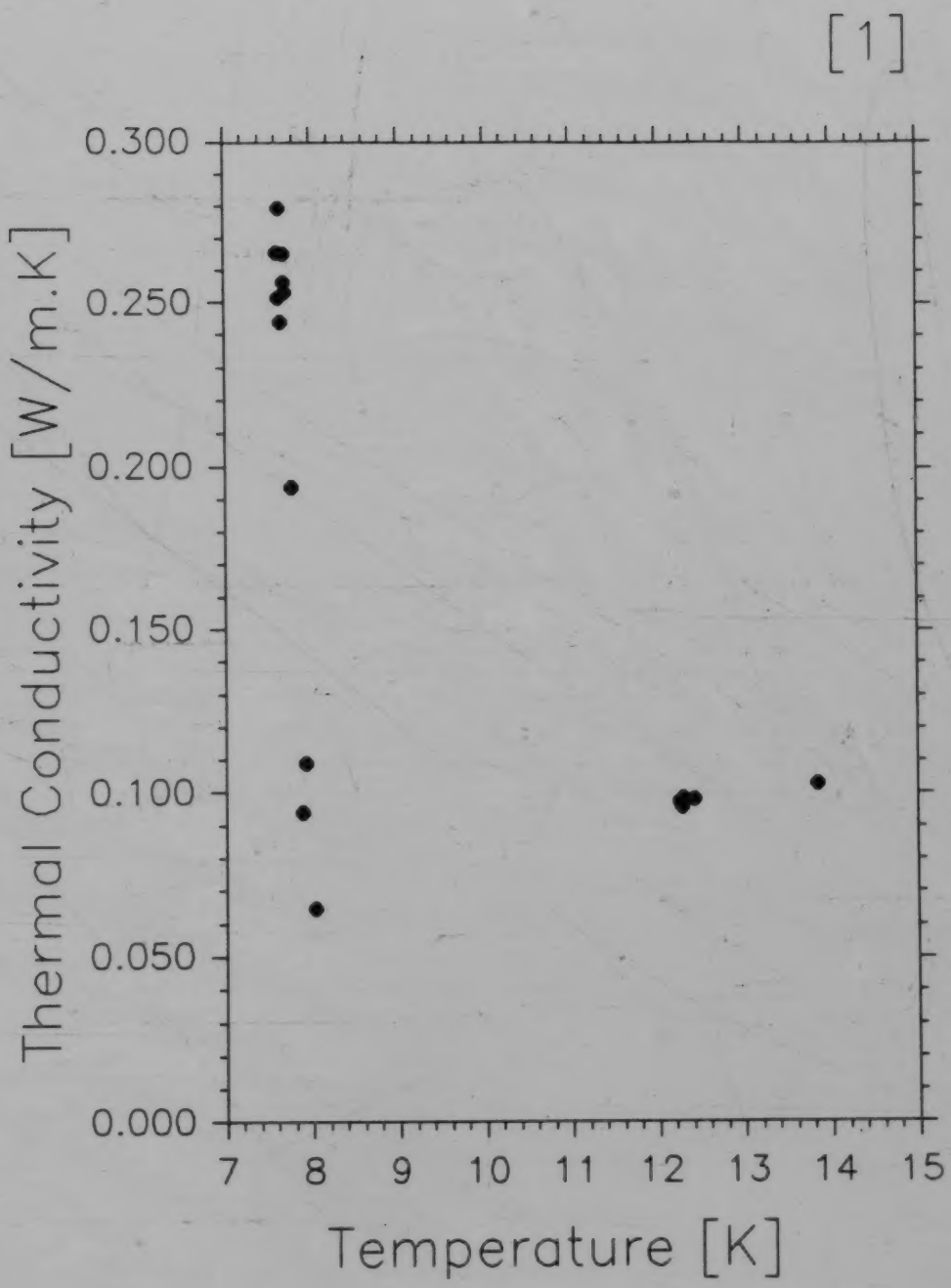

Figure A.2: Trial No. 1

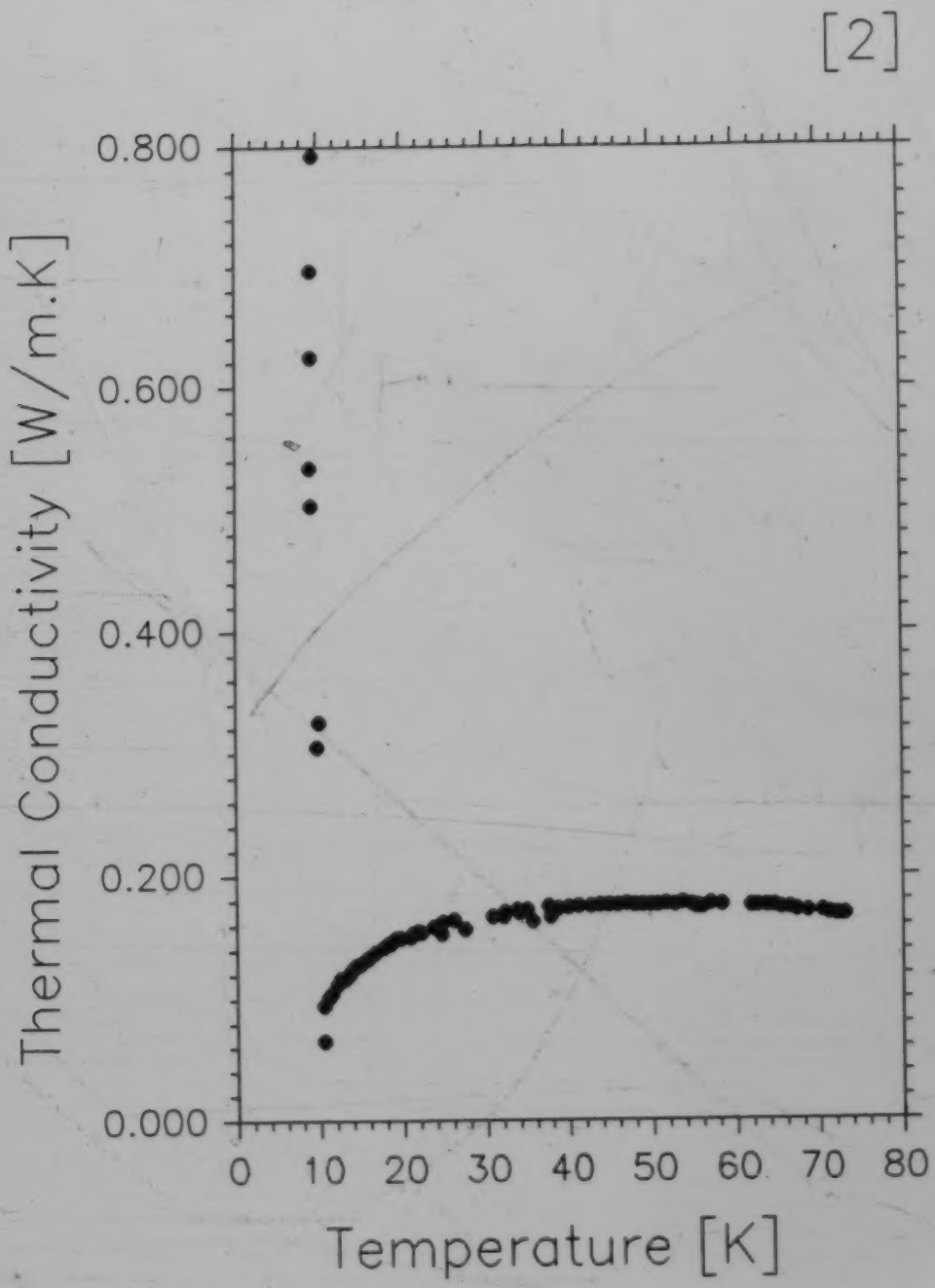

Figure A.3: Trial No. 2

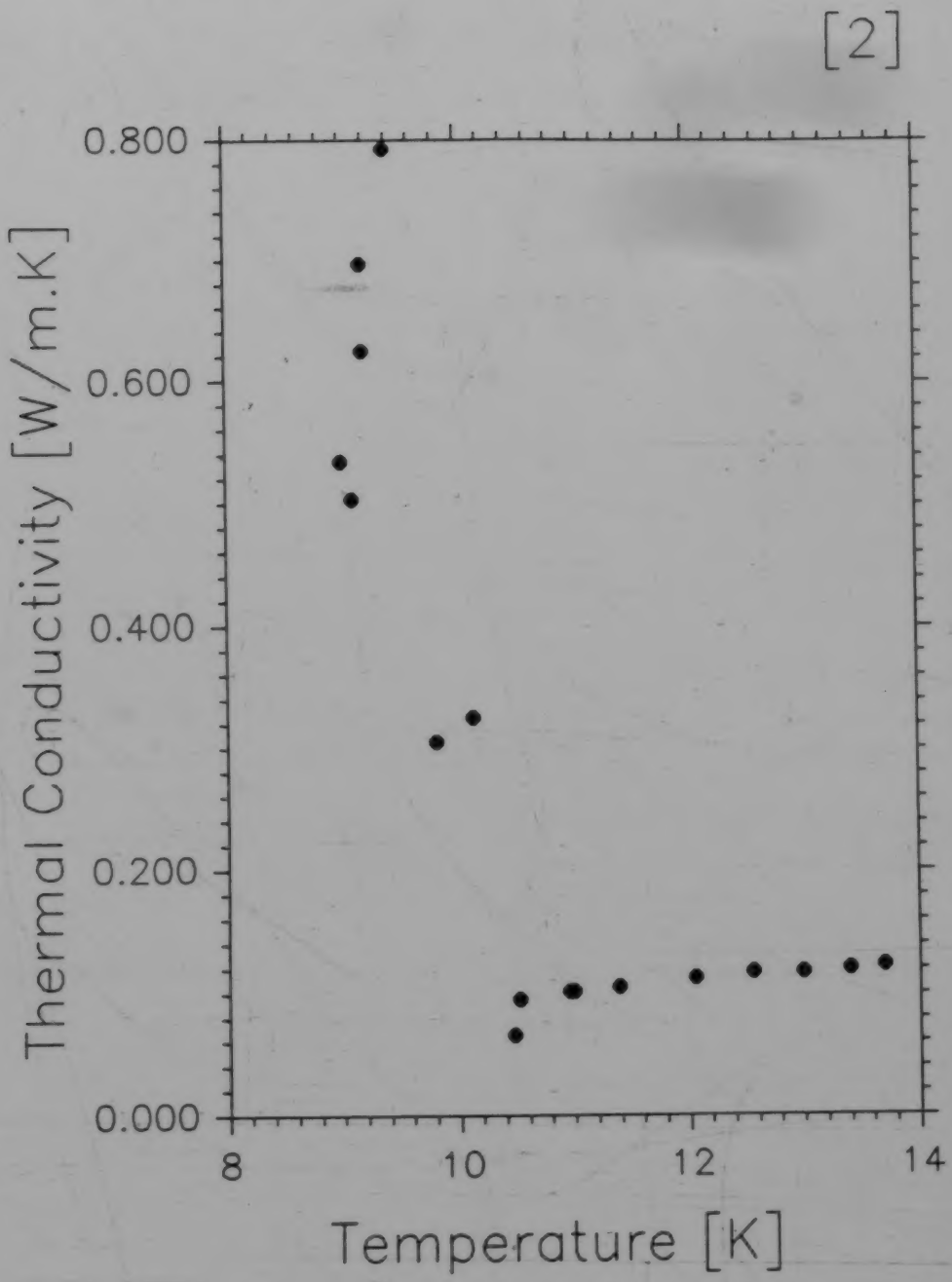

Figure A.4: Trial No. 2

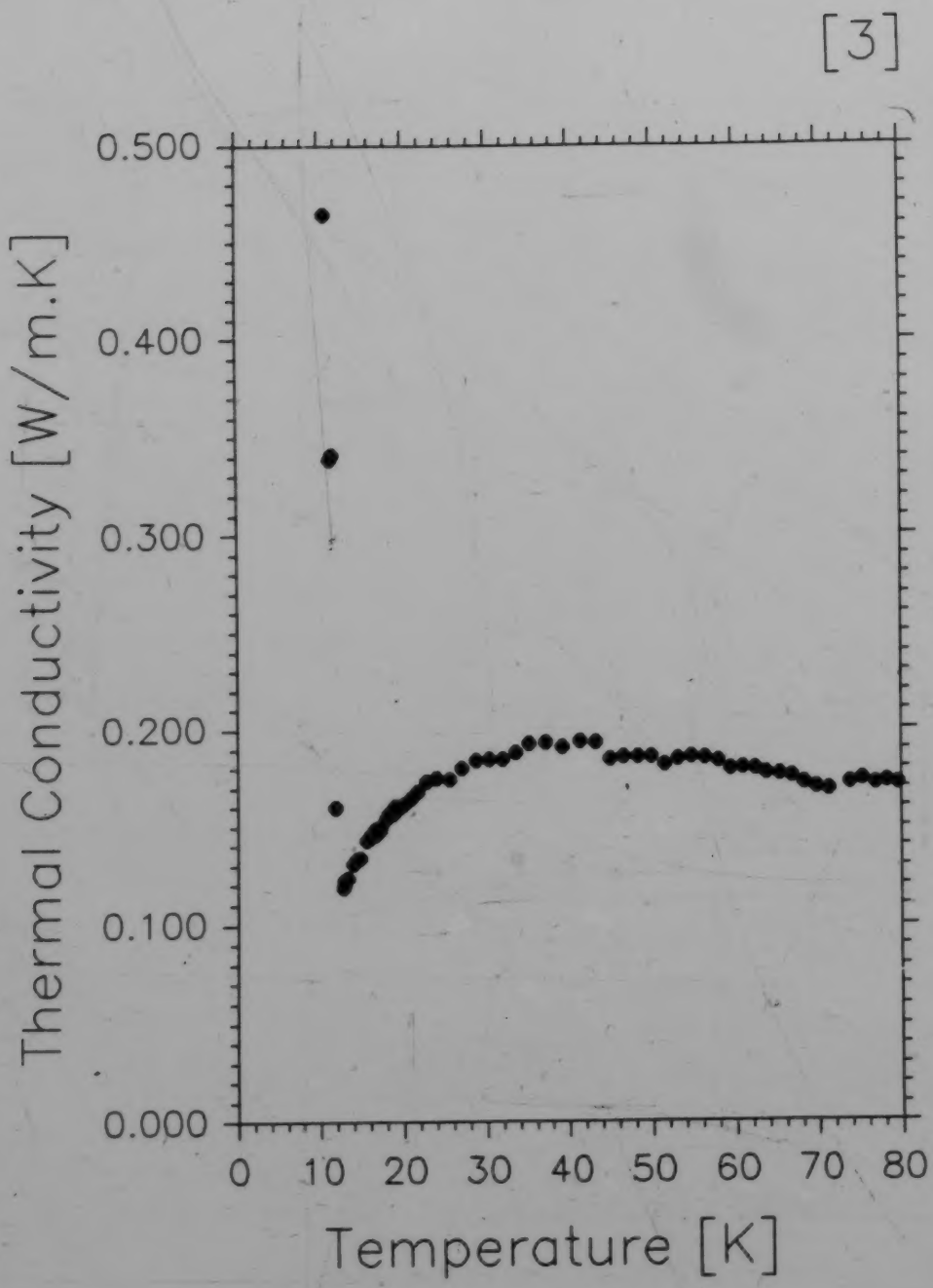

Figure A.5: Trial No. 3

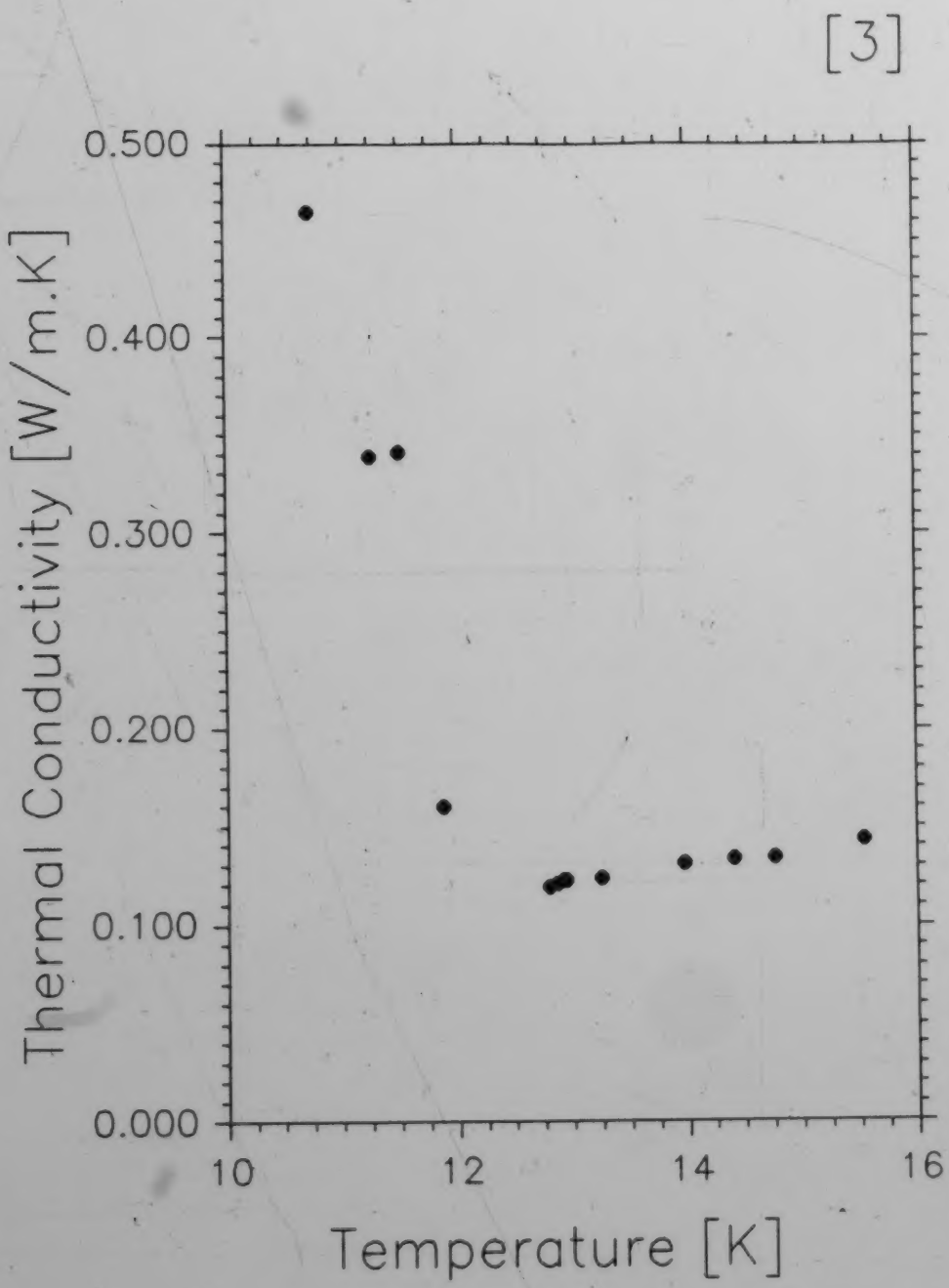

Figure A.6: Trial No. 3

3 of/de 3

PM-1 3½"x4" PHOTOGRAPHIC MICROCOPY TARGET
NBS 1010a ANSI/ISO #2 EQUIVALENT

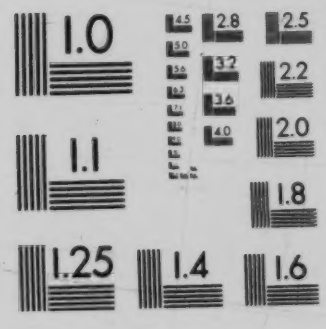

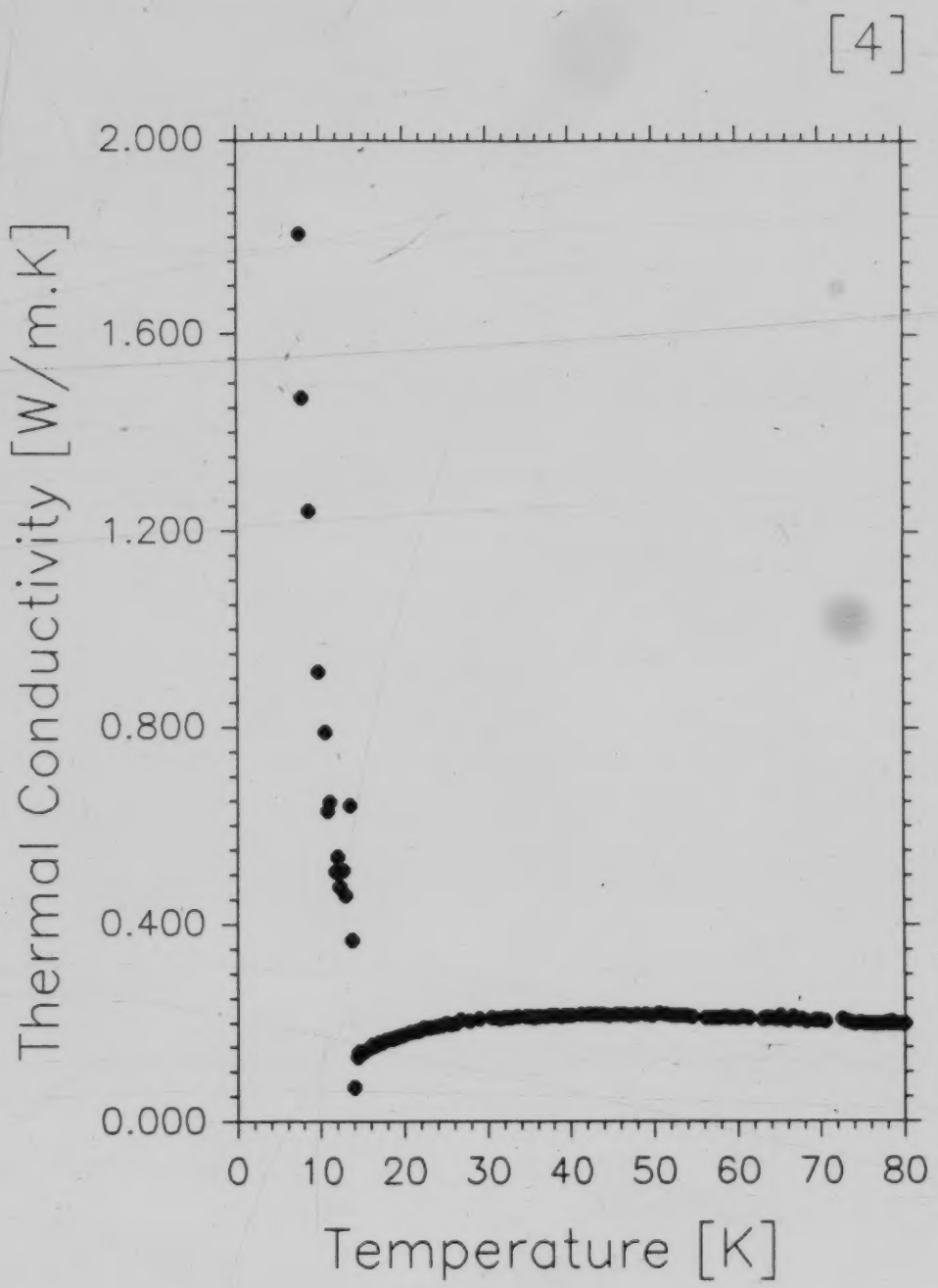

Figure A.7: Trial No. 4

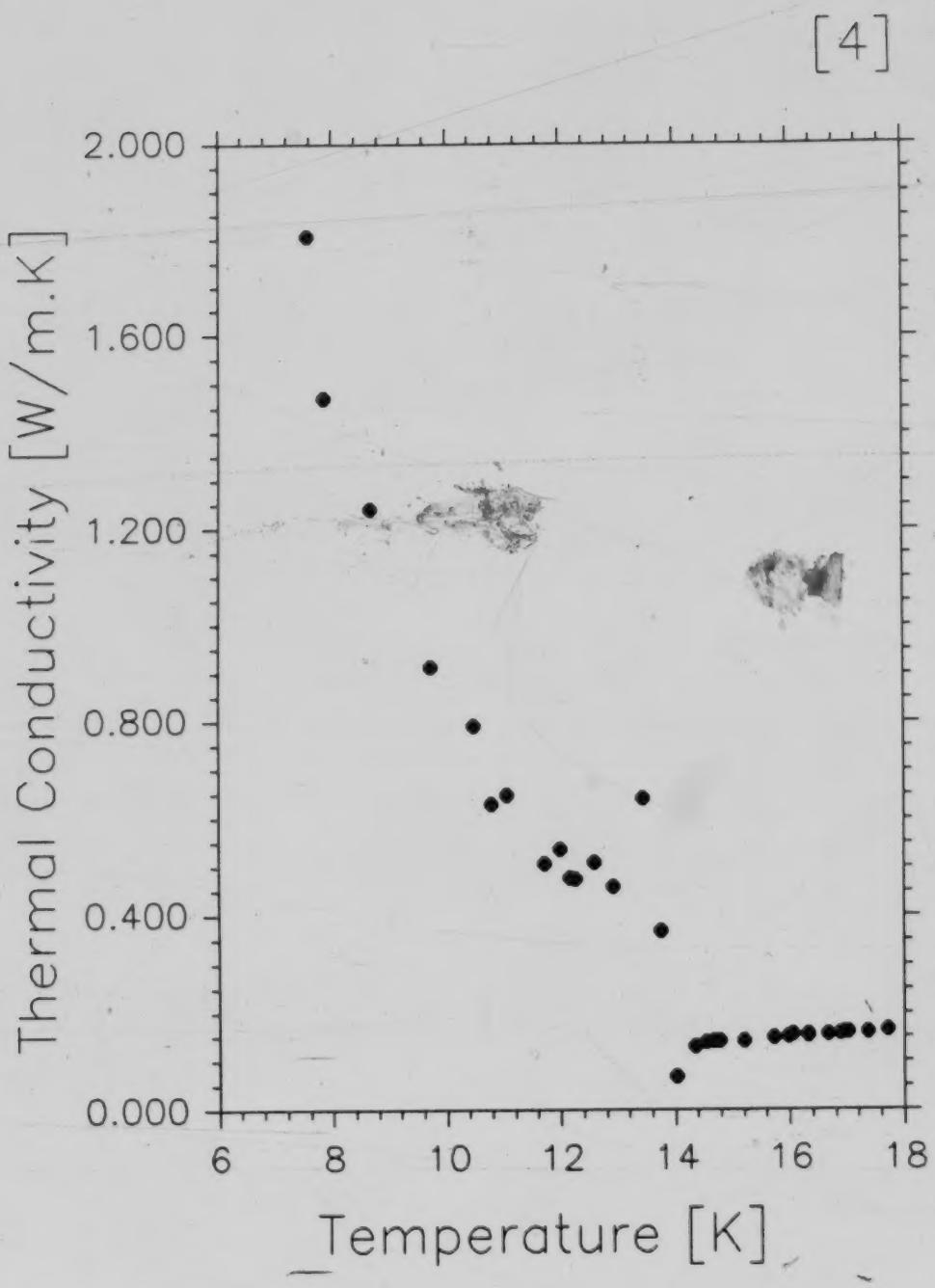

Figure A.8: Trial No. 4

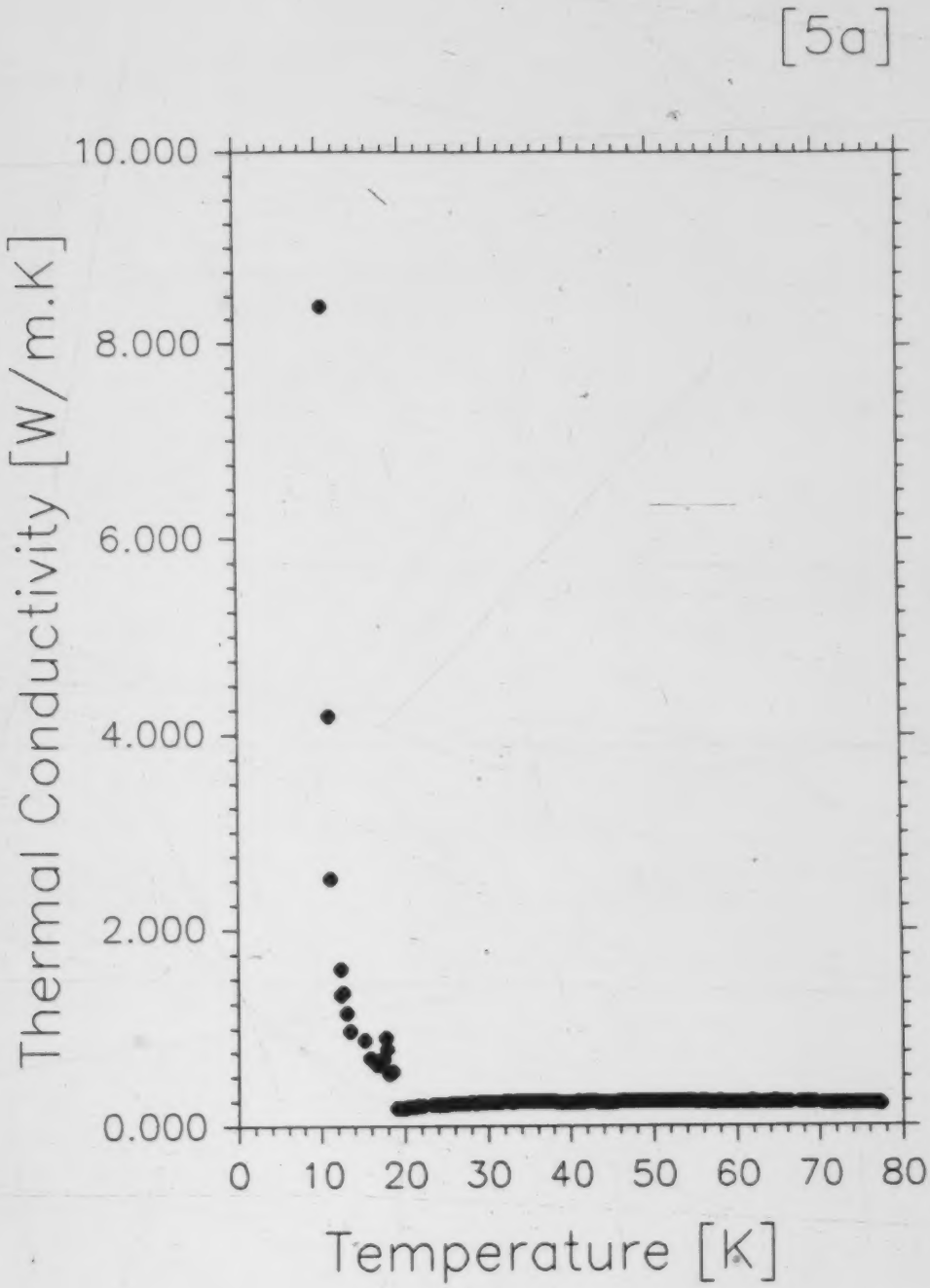

Figure A.9: Trial No. 5a

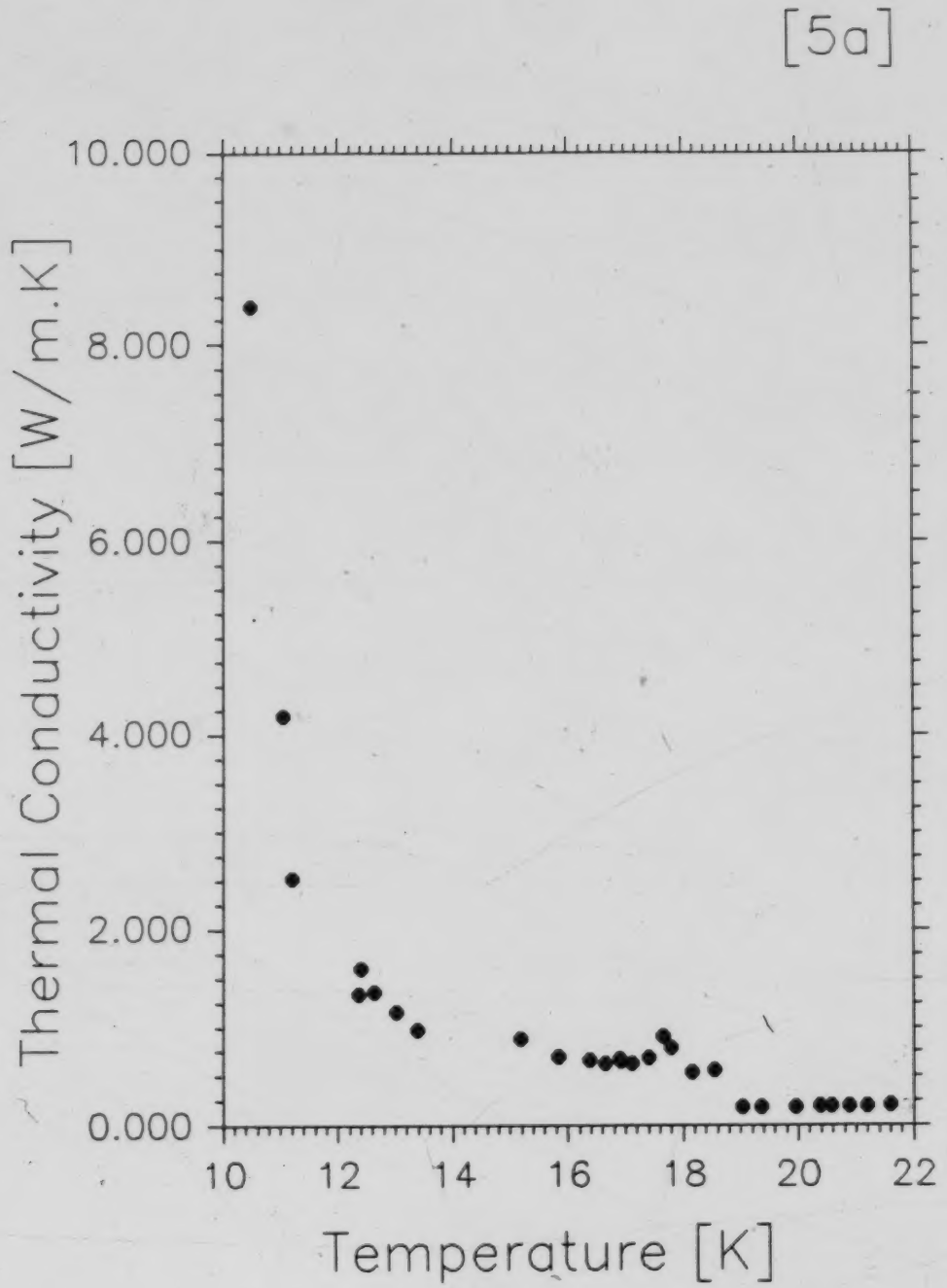

Figure A.10: Trial No. 5a

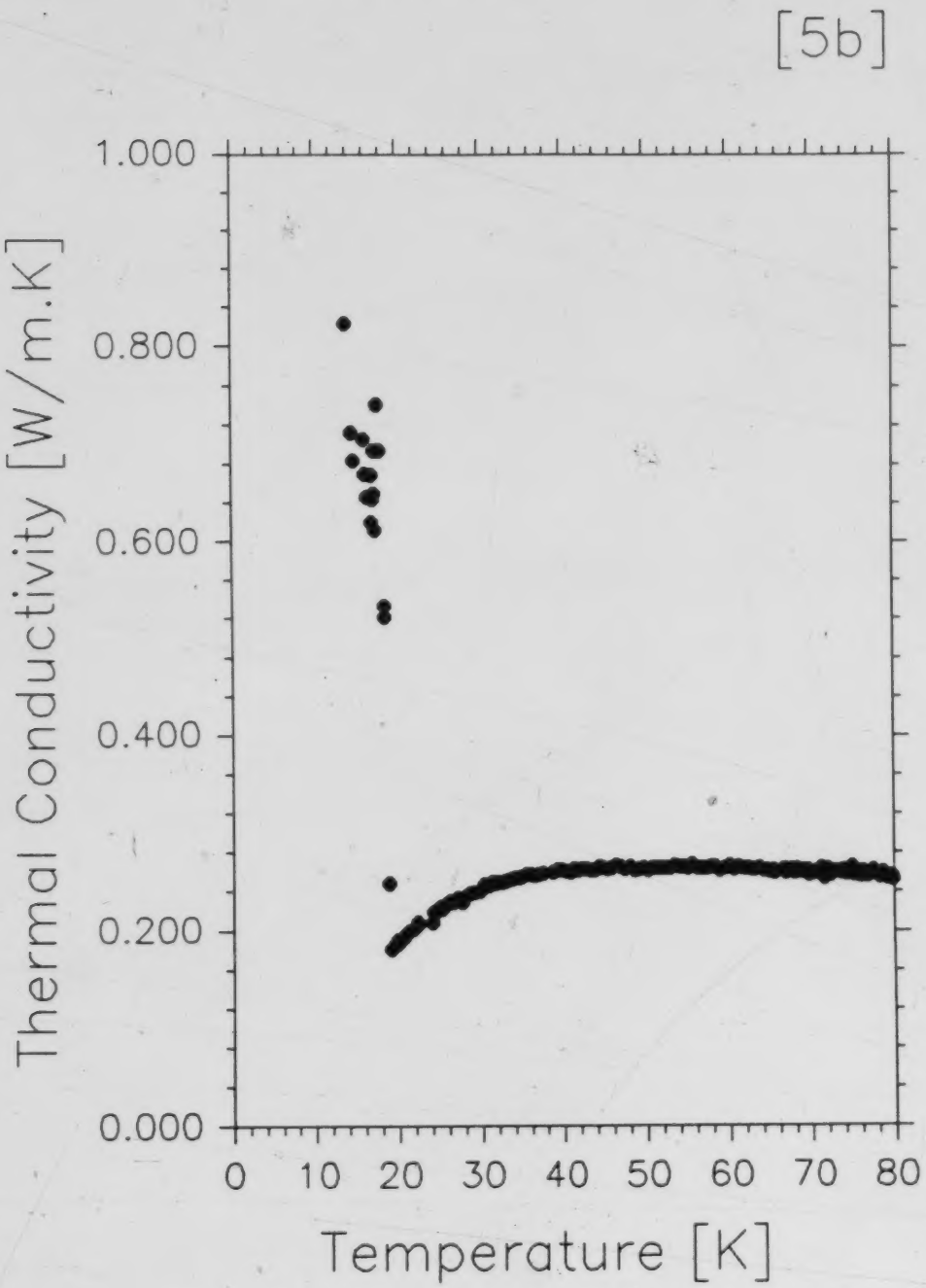

Figure A.11: Trial No. 5b

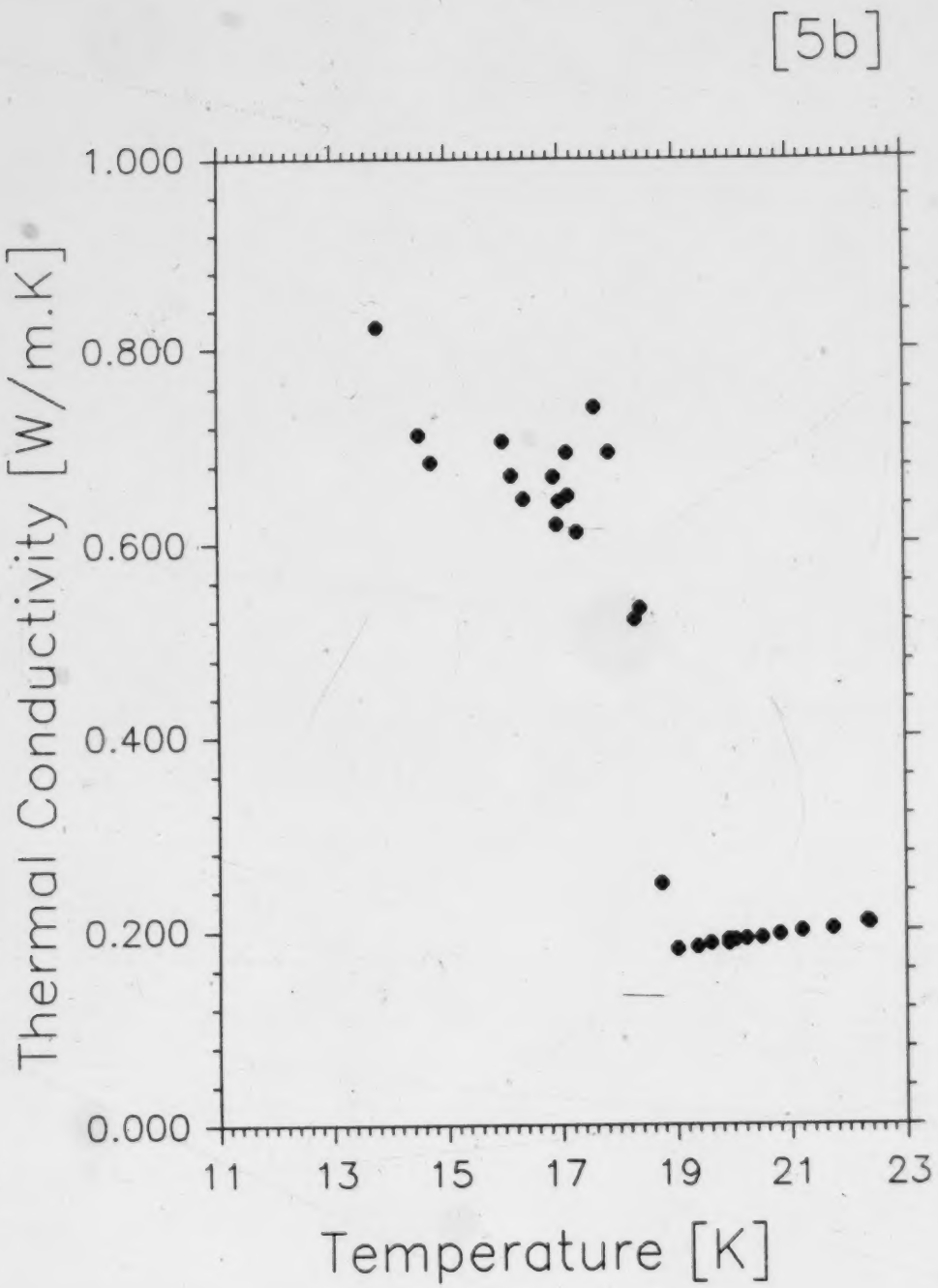

Figure A.12: Trial No. 5b

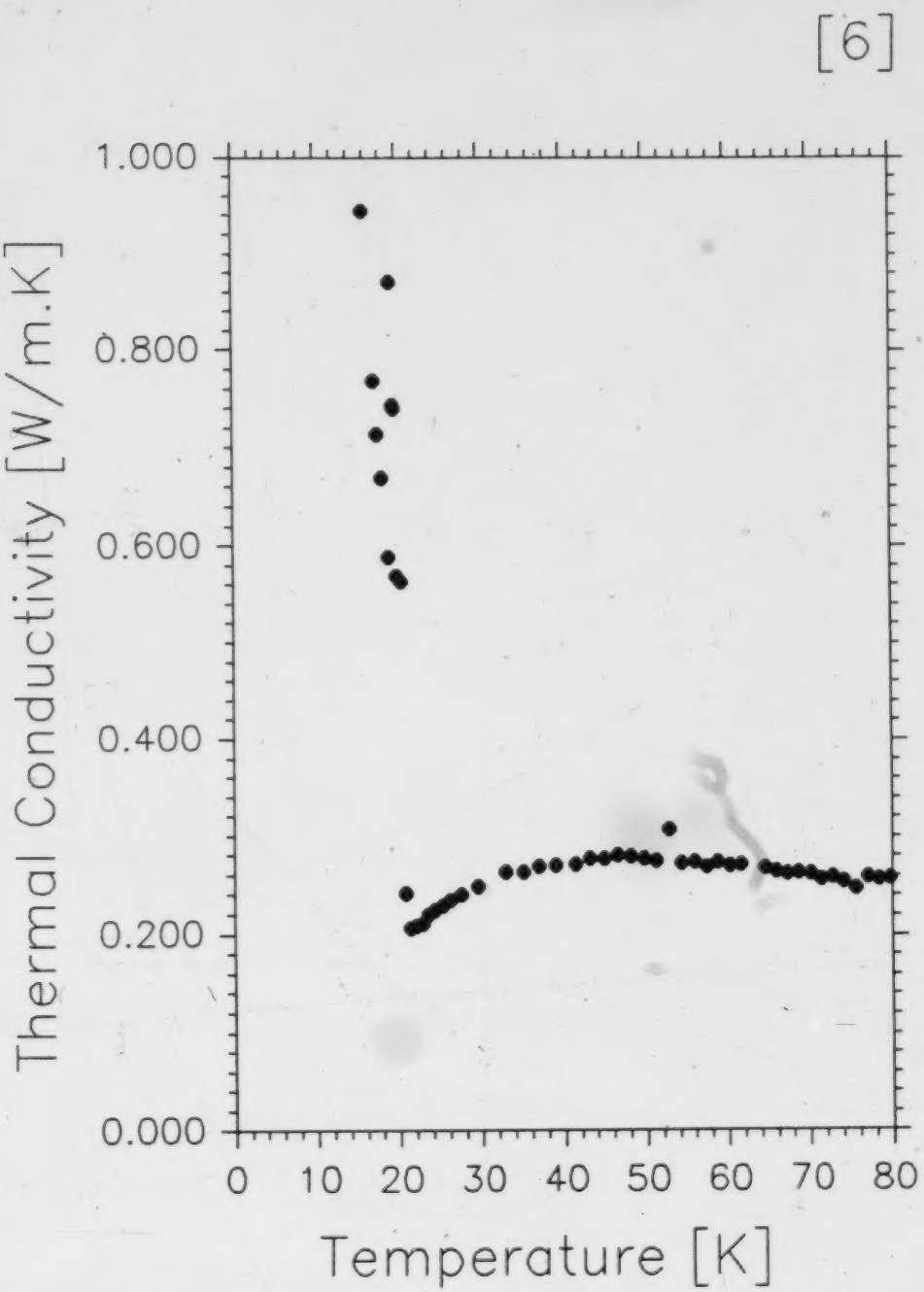

Figure A.13: Trial No. 6

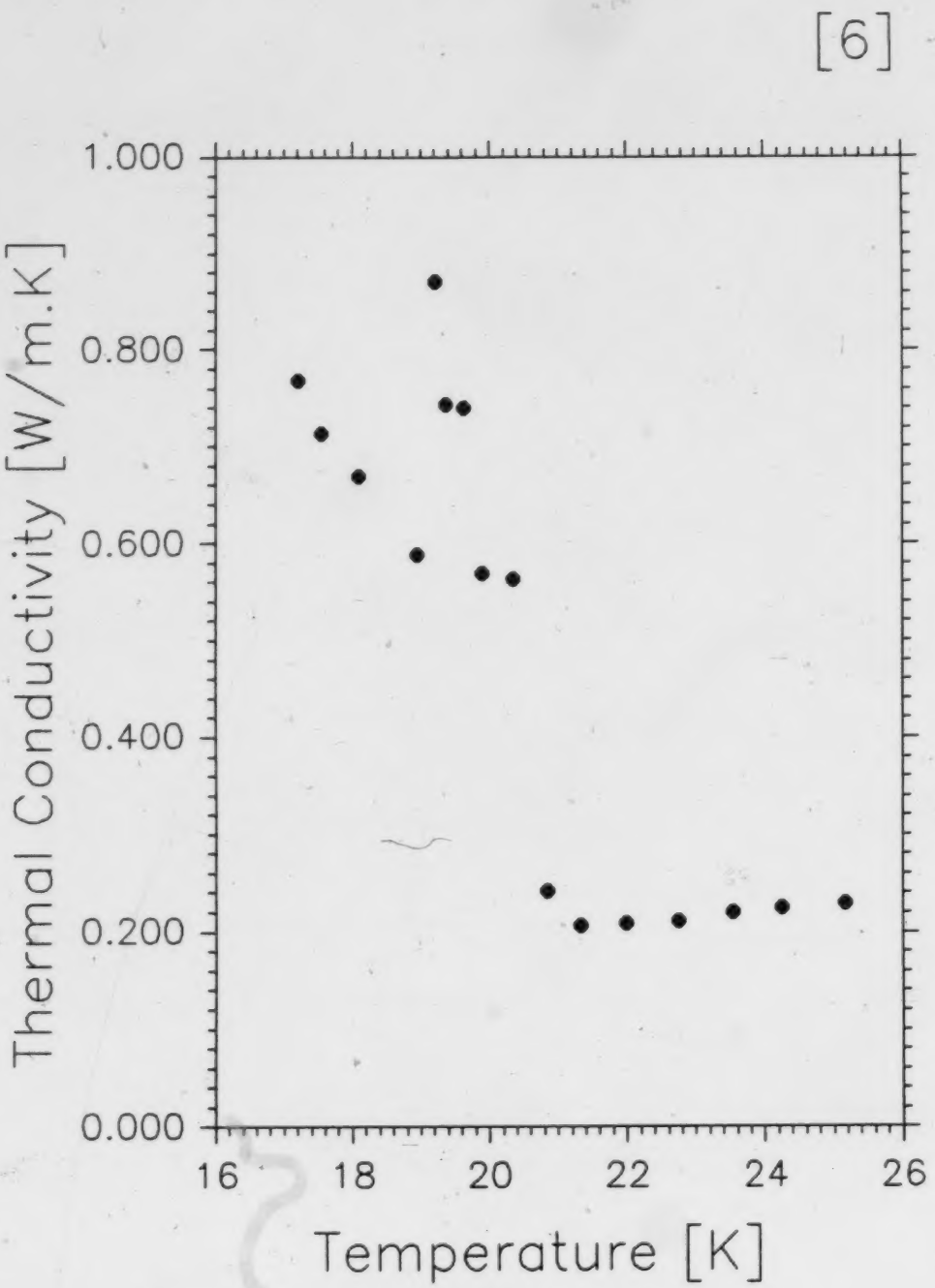

Figure A.14: Trial No. 6

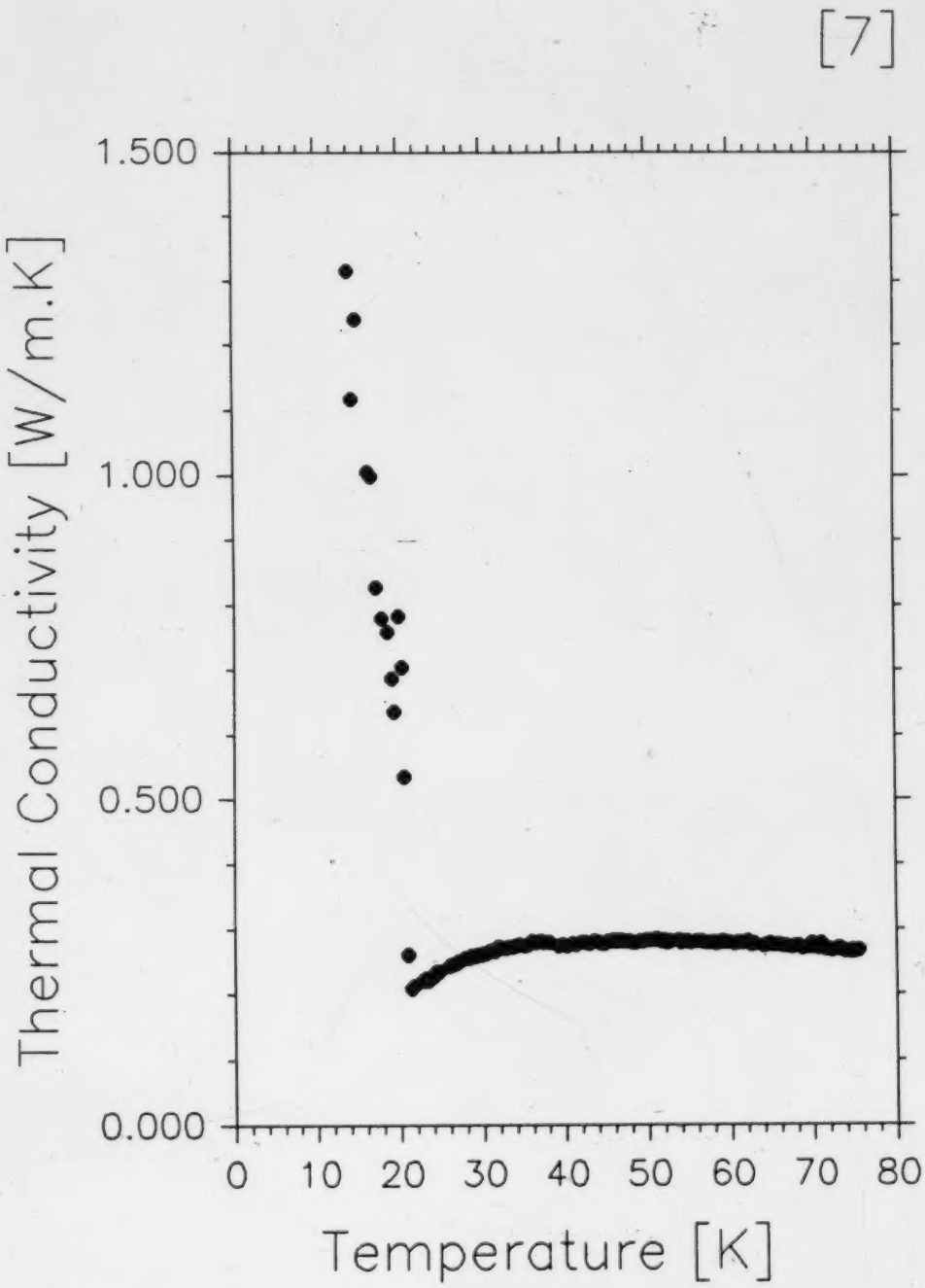

Figure A.15: Trial No. 7

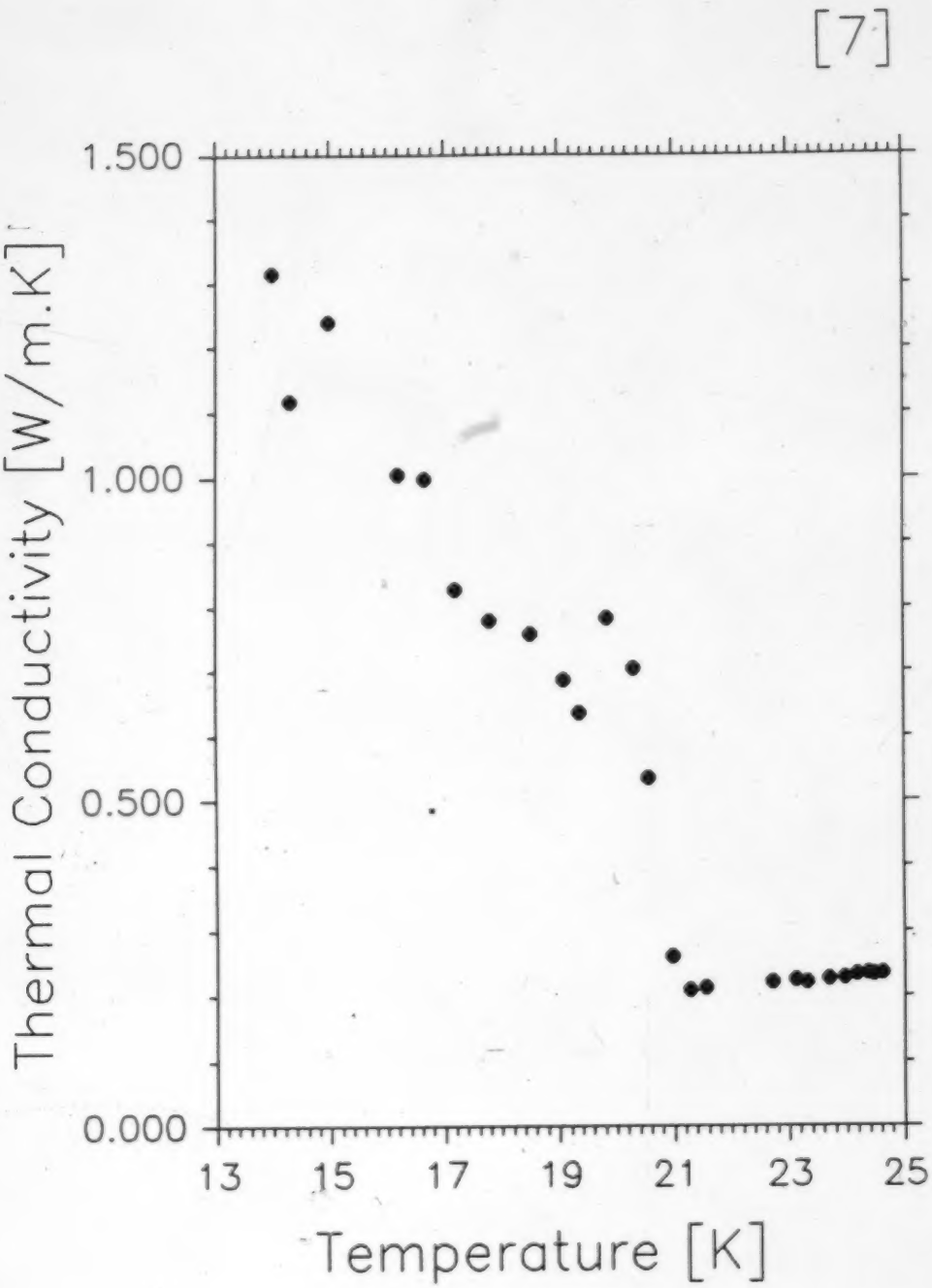

Figure A.16: Trial No. 7

Appendix B

Comparison with MET

The graphs in this chapter show experimental values of the thermal conductivity of helium along with values predicted by the Modified Enskog Theory (MET) for a dense gas of hard spheres (HS) and a Lennard-Jones fluid (LJ); the equations for these models are provided in Section 2.3.1 (hard spheres) and Section 5.4 (Lennard-Jones fluid). The values of molar volume were calculated on the basis of an equation of state (EOS) given either by McCarty [15] or Mills, Liebenberg and Bronson [57] for the appropriate region of applicability. As the molar volumes for the MET equation were obtained from raw data which in some cases contained small gaps, these gaps are also present in the predicted values.

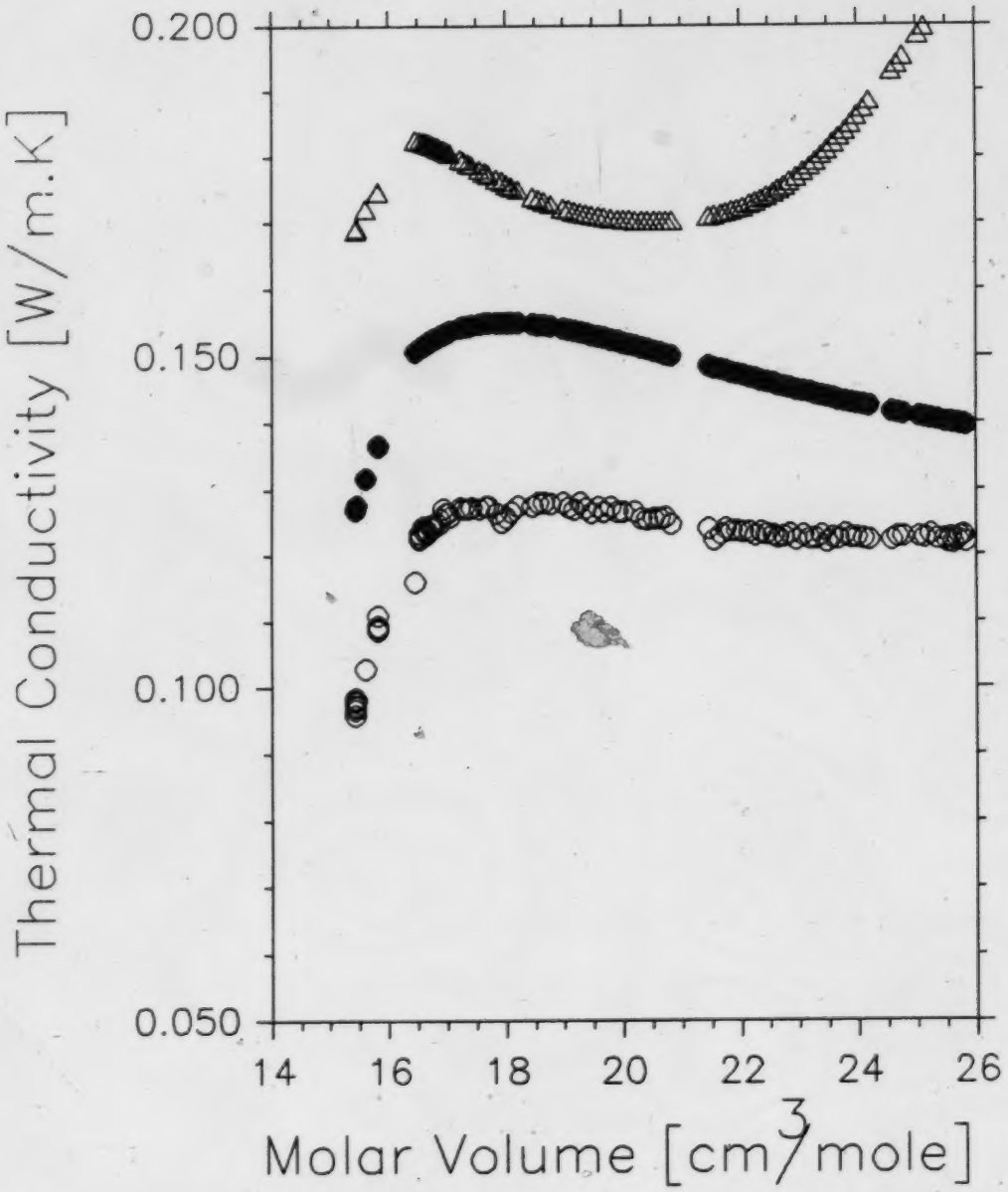

Figure B.1: Trial No. 1; o experimental values; • MET (dense hard sphere gas); △ MET (Lennard-Jones fluid)

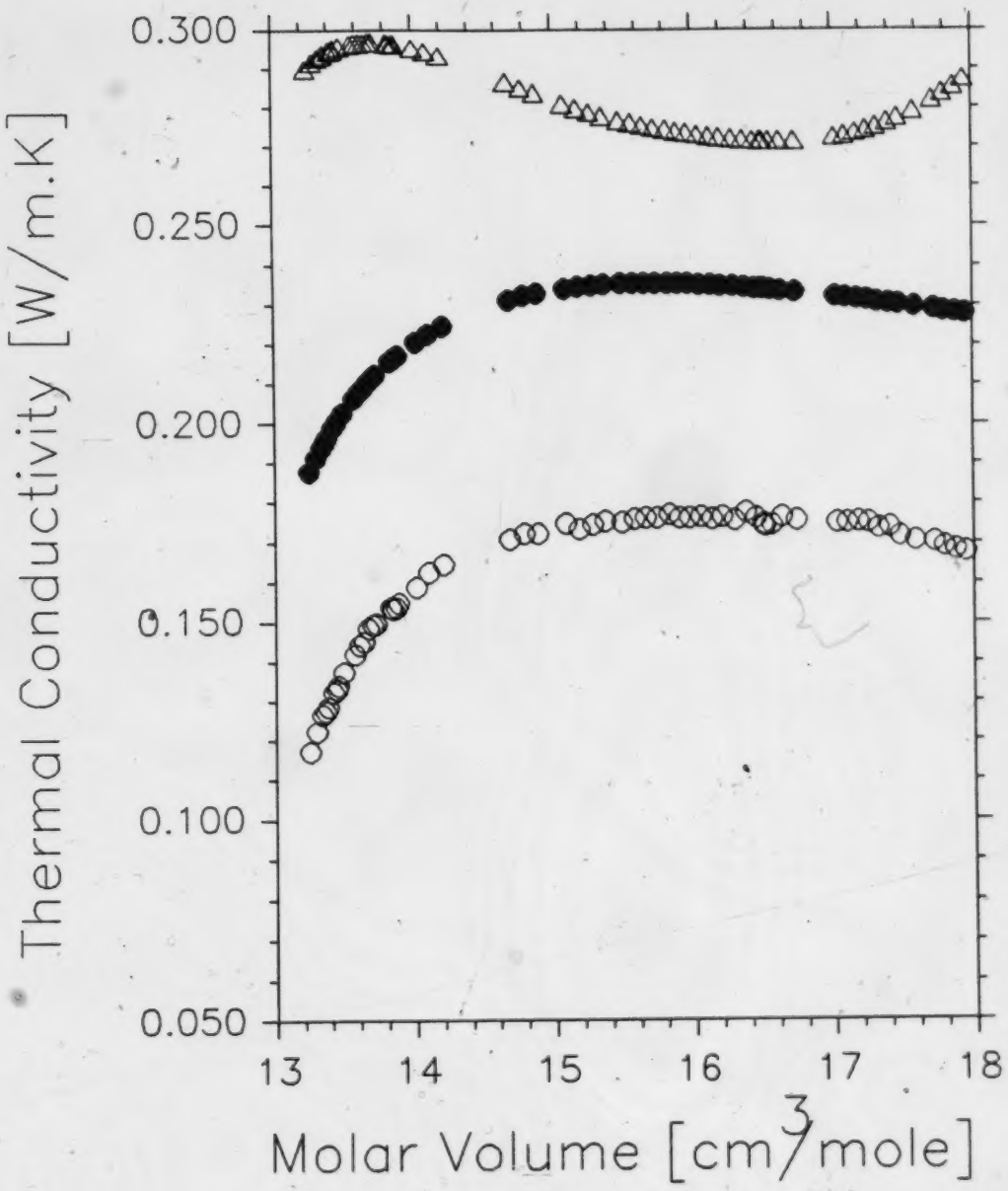

Figure B.2: Trial No. 2; ○ experimental values; • MET (dense hard sphere gas); △ MET (Lennard-Jones fluid)

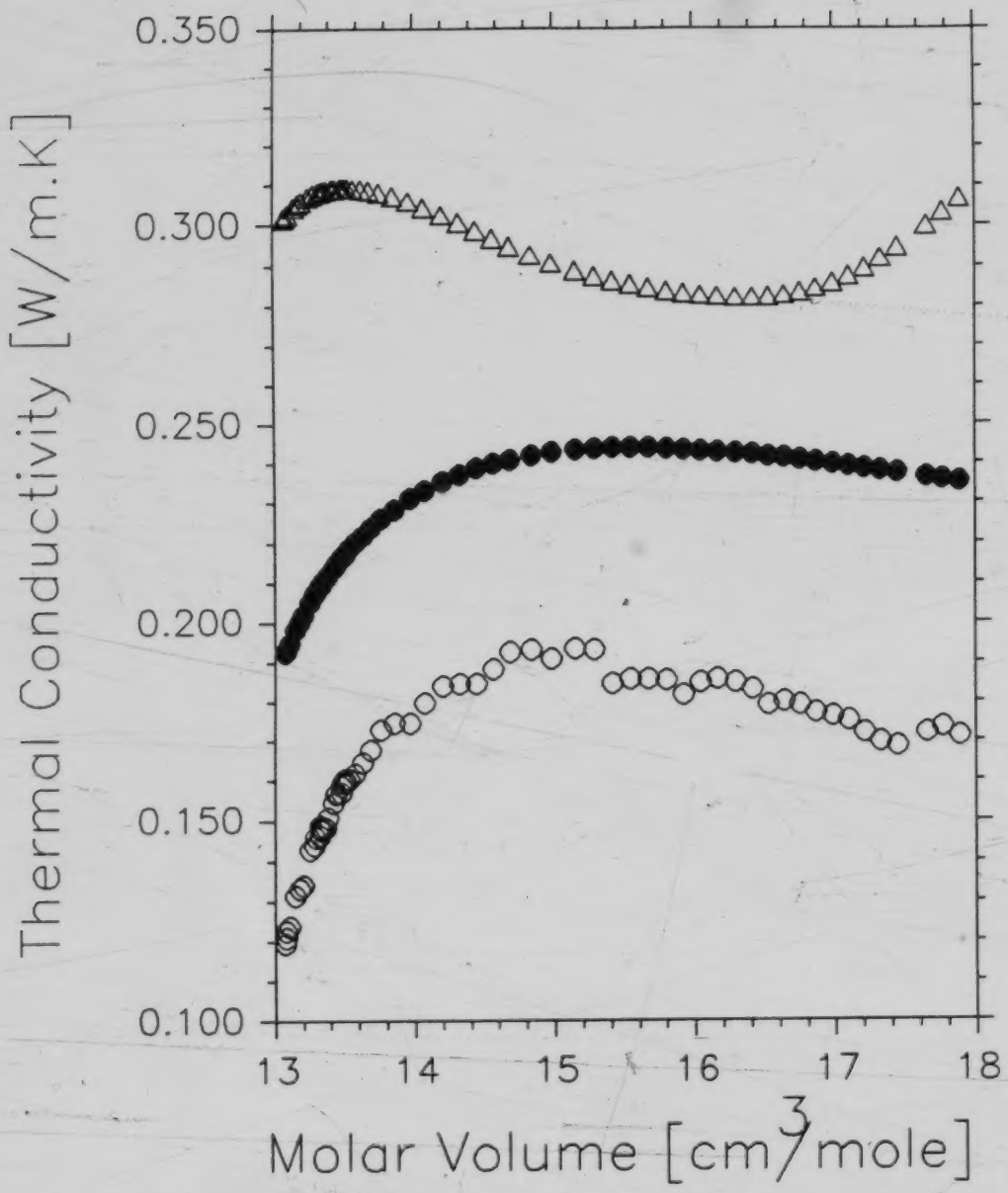

Figure B.3: Trial No. 3; ○ experimental values; • MET (dense hard sphere gas); △ MET (Lennard-Jones fluid)

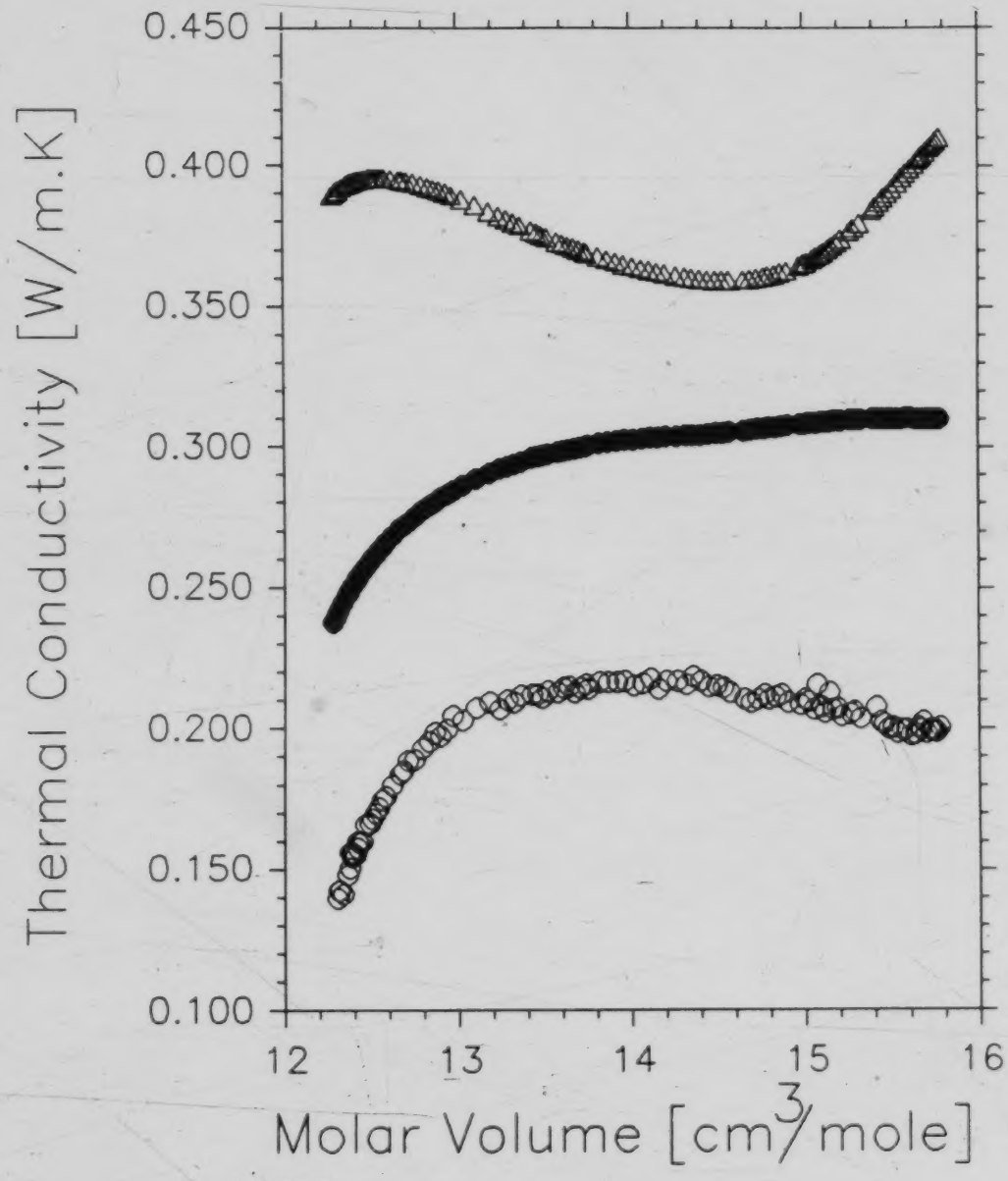

Figure B.4: Trial No. 4; ○ experimental values; • MET (dense hard sphere gas); △ MET (Lennard-Jones fluid)

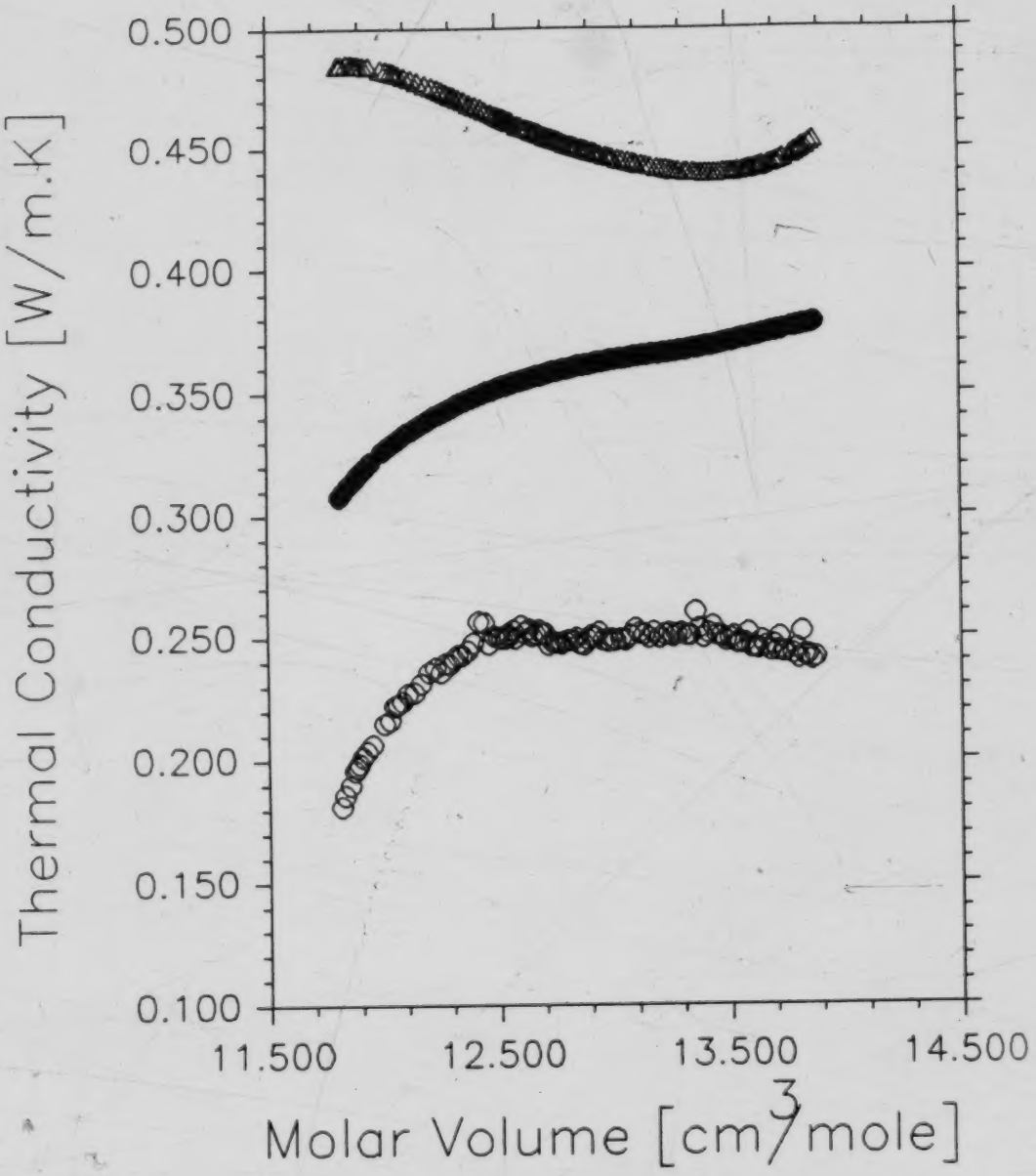

Figure B.5: Trial No. 5a; ○ experimental values; • MET (dense hard sphere gas); △ MET (Lennard-Jones fluid)

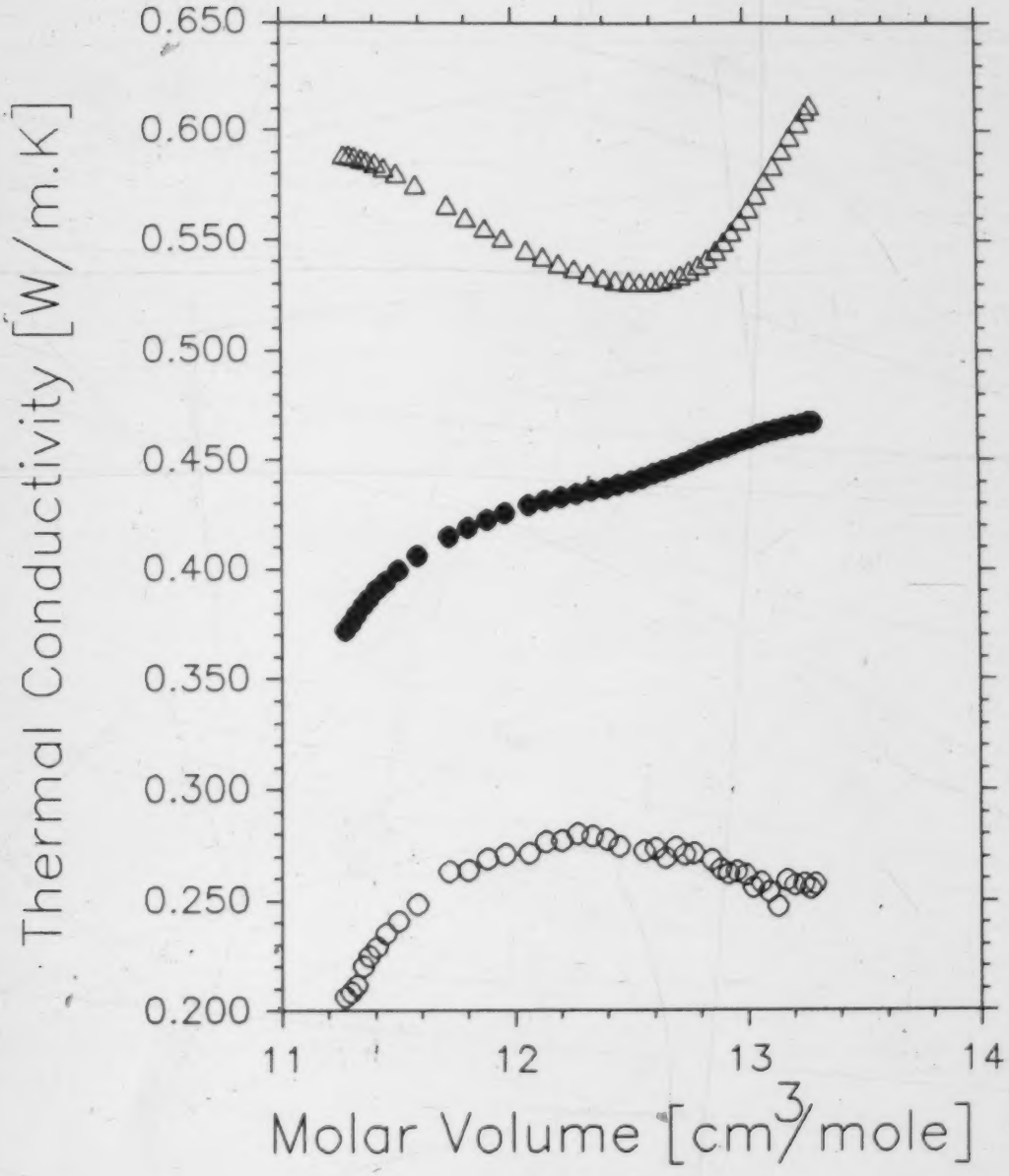

Figure B.6: Trial No. 6; ○ experimental values; • MET (dense hard sphere gas); △ MET (Lennard-Jones fluid)

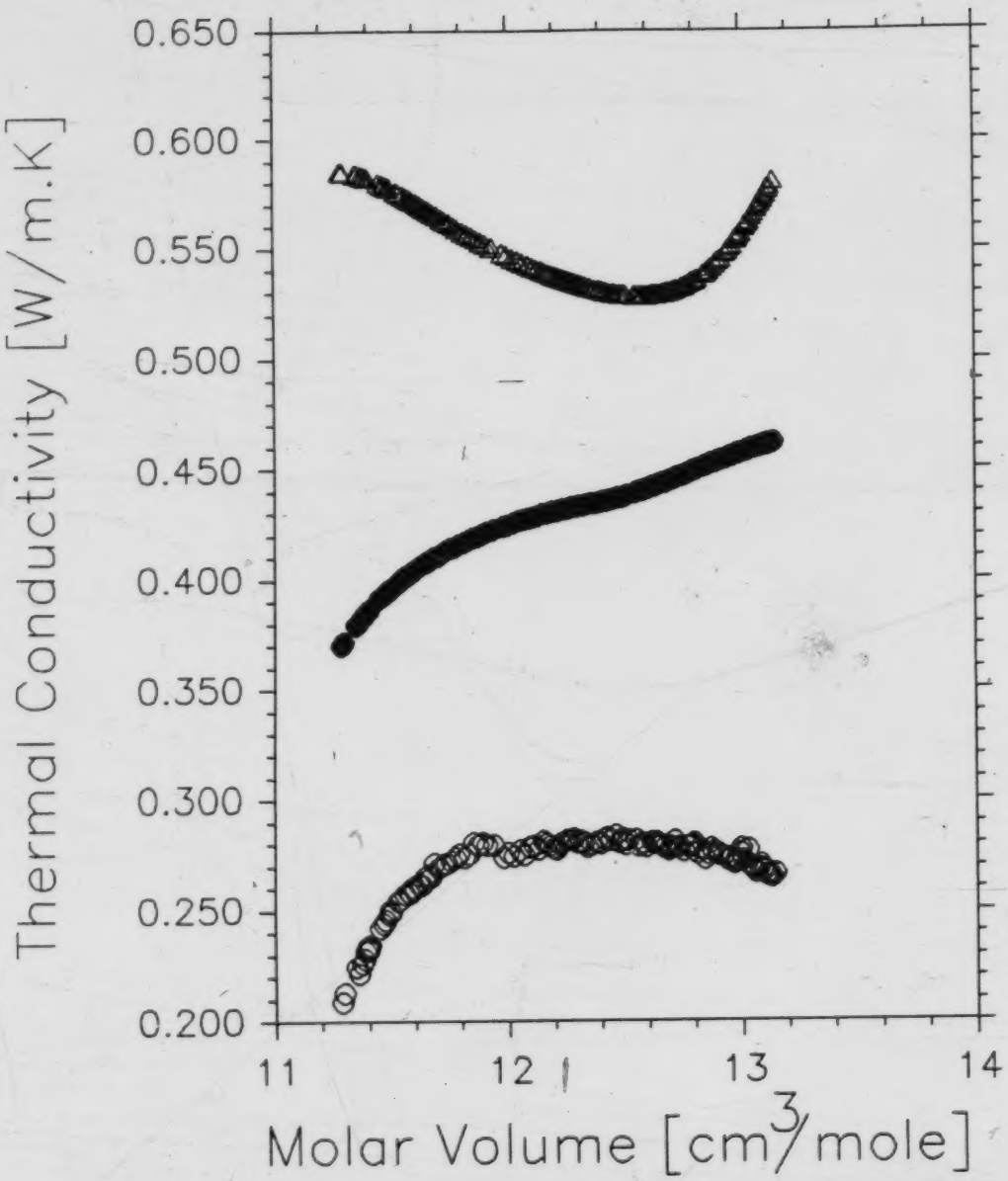

Figure B.7: Trial No. 7; ○ experimental values; • MET (dense hard sphere gas); △ MET (Lennard-Jones fluid)

Appendix C

Thermal Conductivity of the Fluid

This chapter contains figures showing the thermal conductivity values for the fluid range only in each trial. In figures C.1 and C.3 the curves are taken from McCarty [15] and represent theoretical thermal conductivity coefficients along isobars over the same temperature range (Figure C.1: 507 bar isobar; Figure C.3: 1013 bar isobar). The experimental data were obtained under nearly isobaric conditions at 486.1 bar (Figure C.1) and 954.9 bar (Figure C.3).

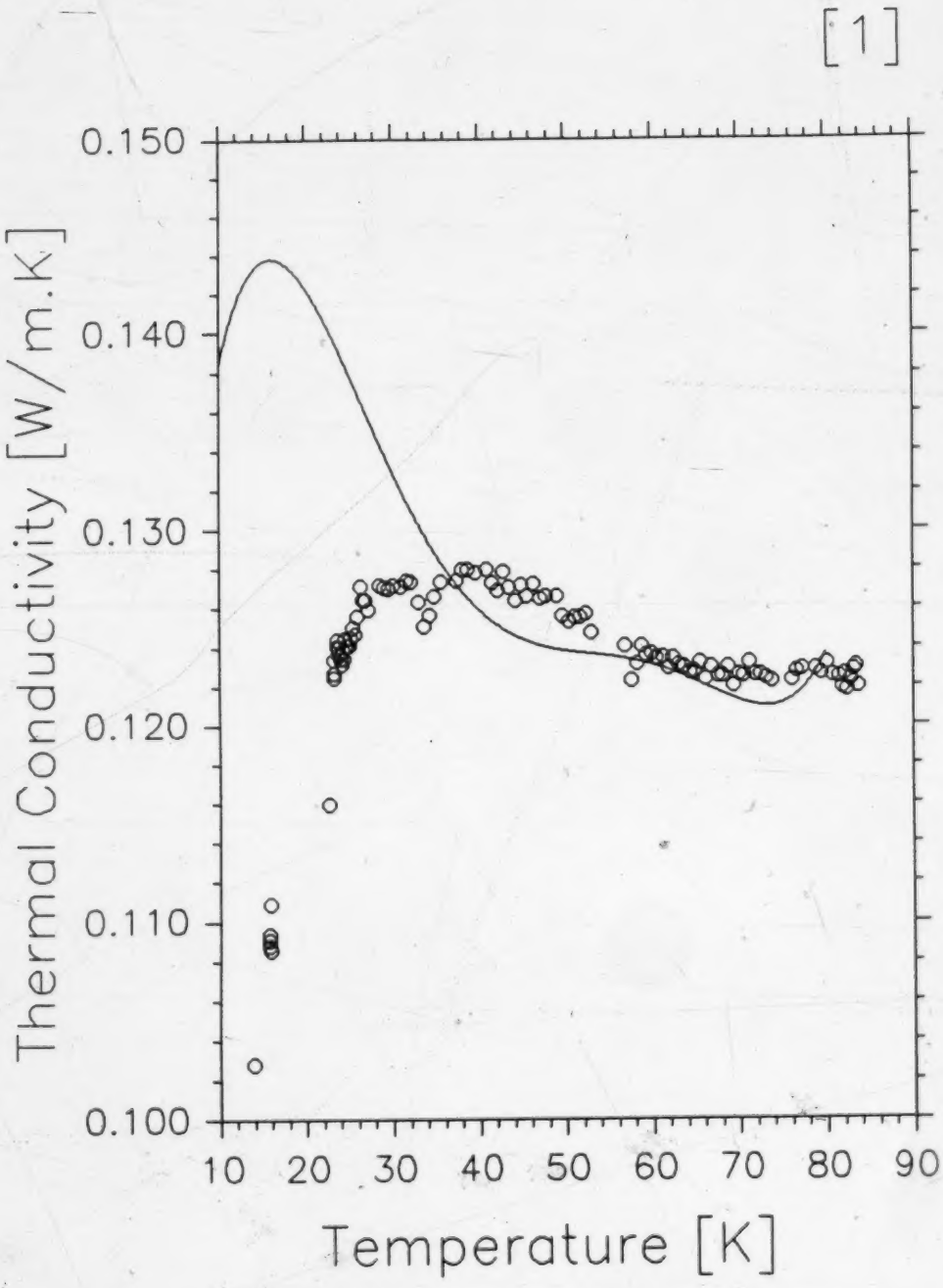

Figure C.1: Trial No. 1

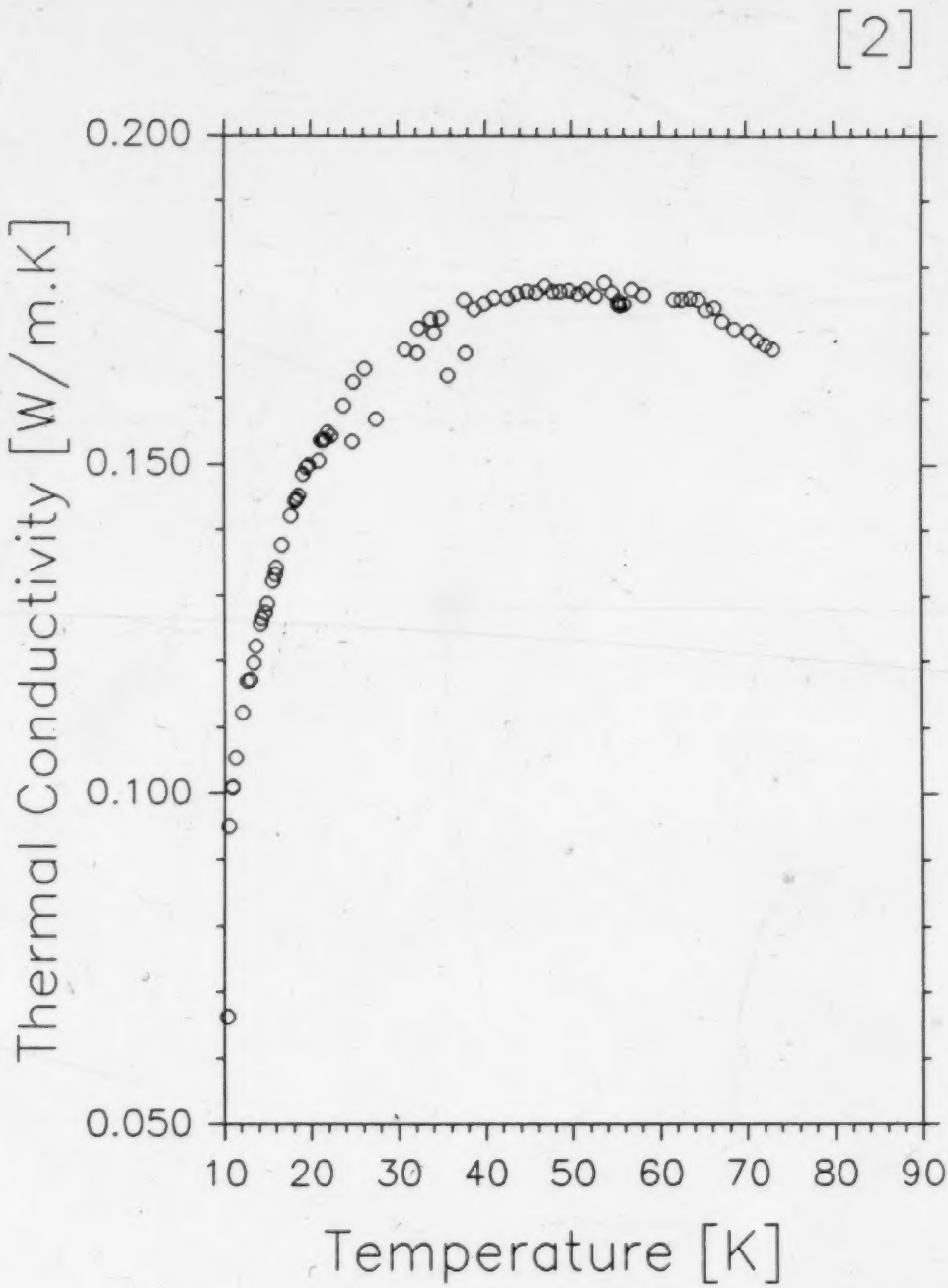

Figure C.2: Trial No. 2

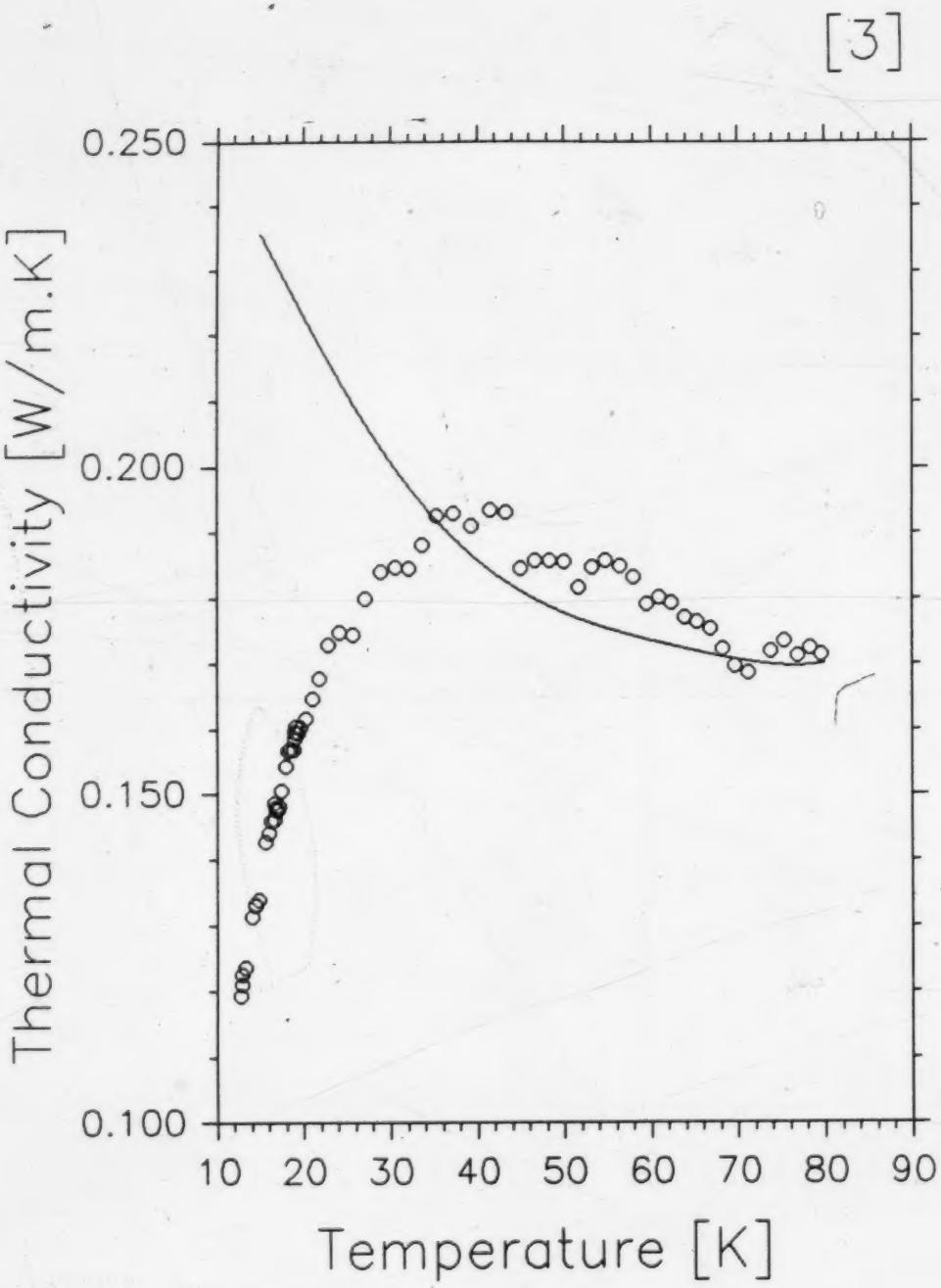

Figure C.3: Trial No. 3

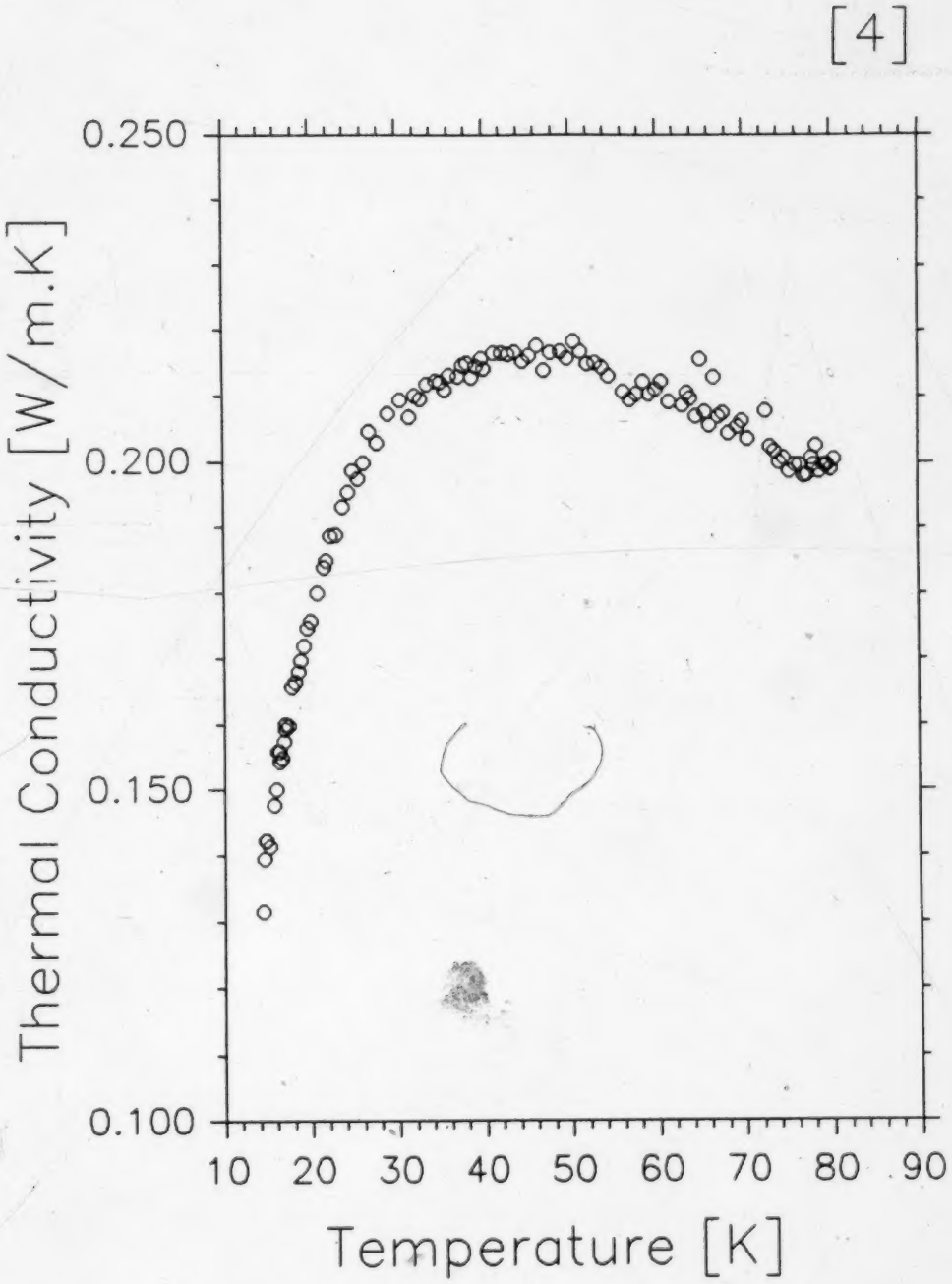

Figure C.4: Trial No. 4

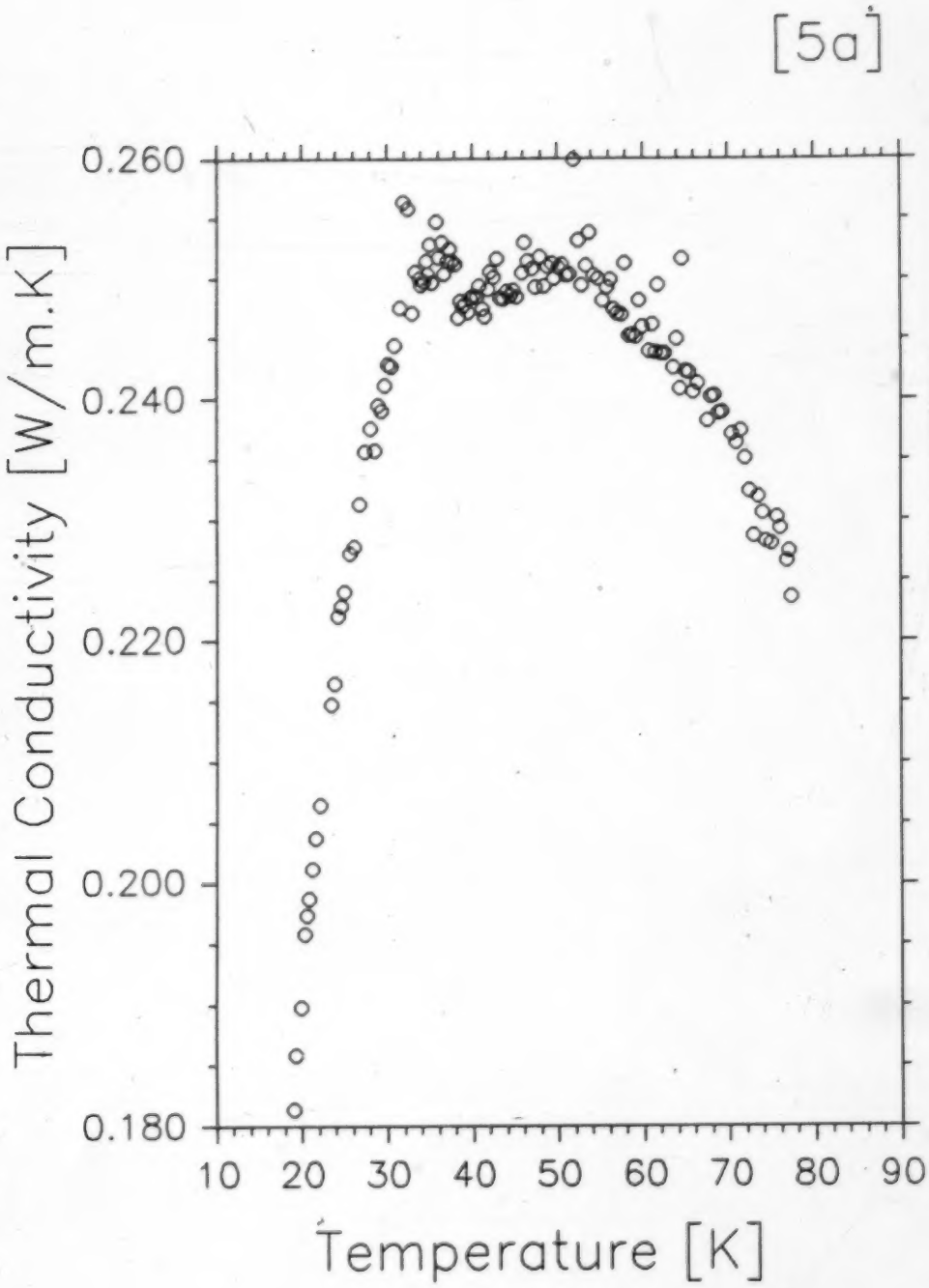

Figure C.5: Trial No. 5a

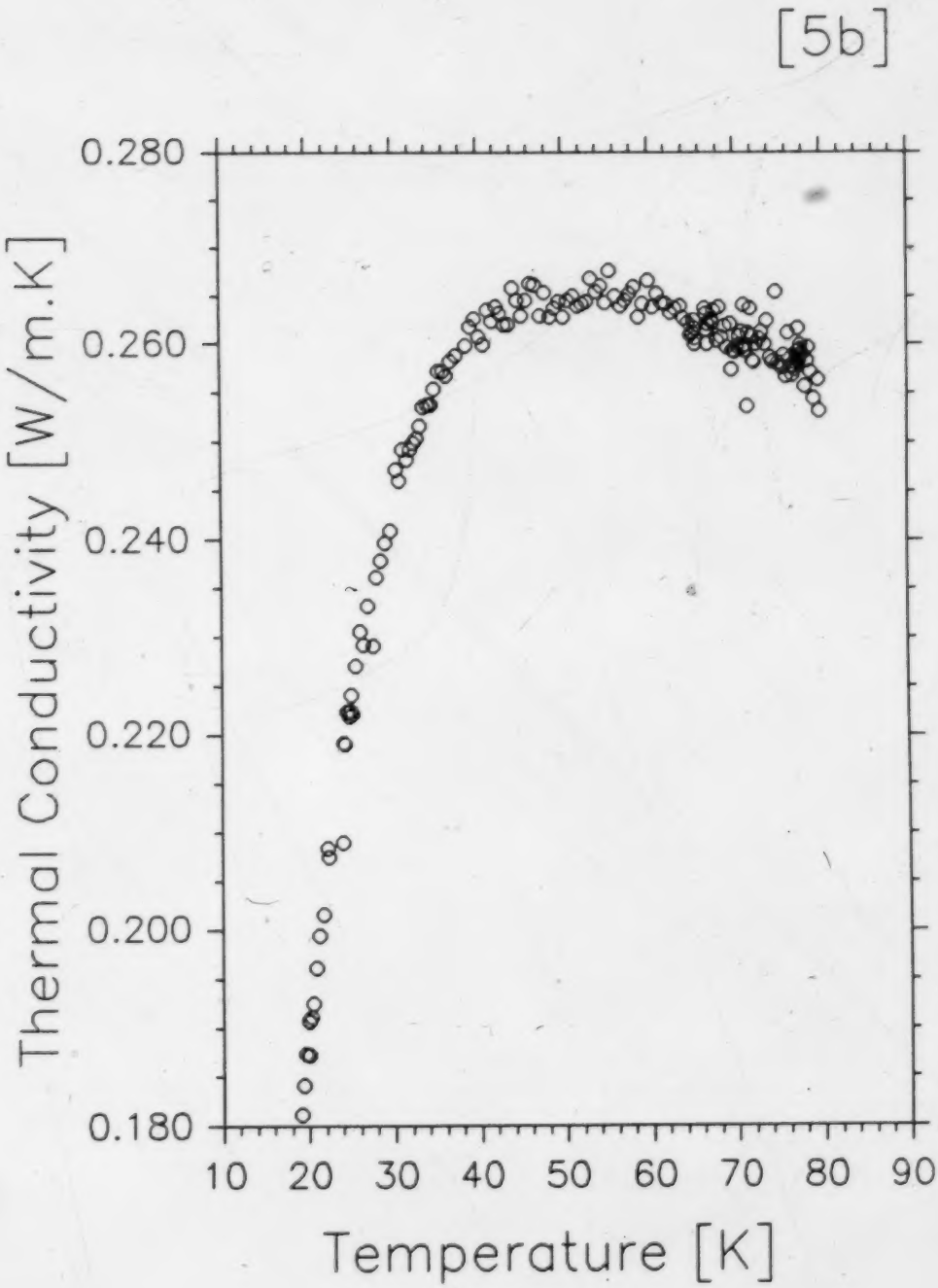

Figure C.6: Trial No. 5b

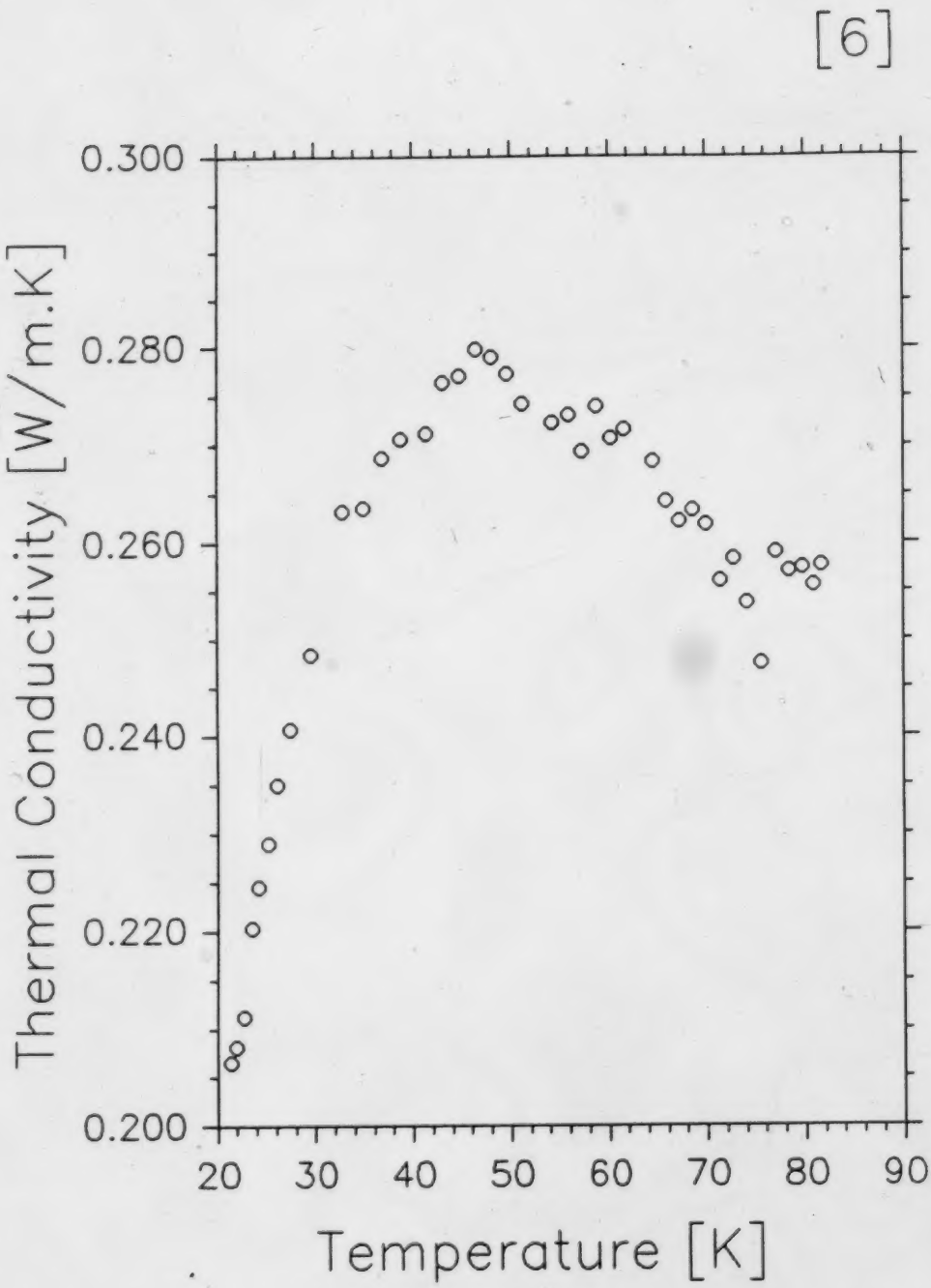

Figure C.7: Trial No. 6

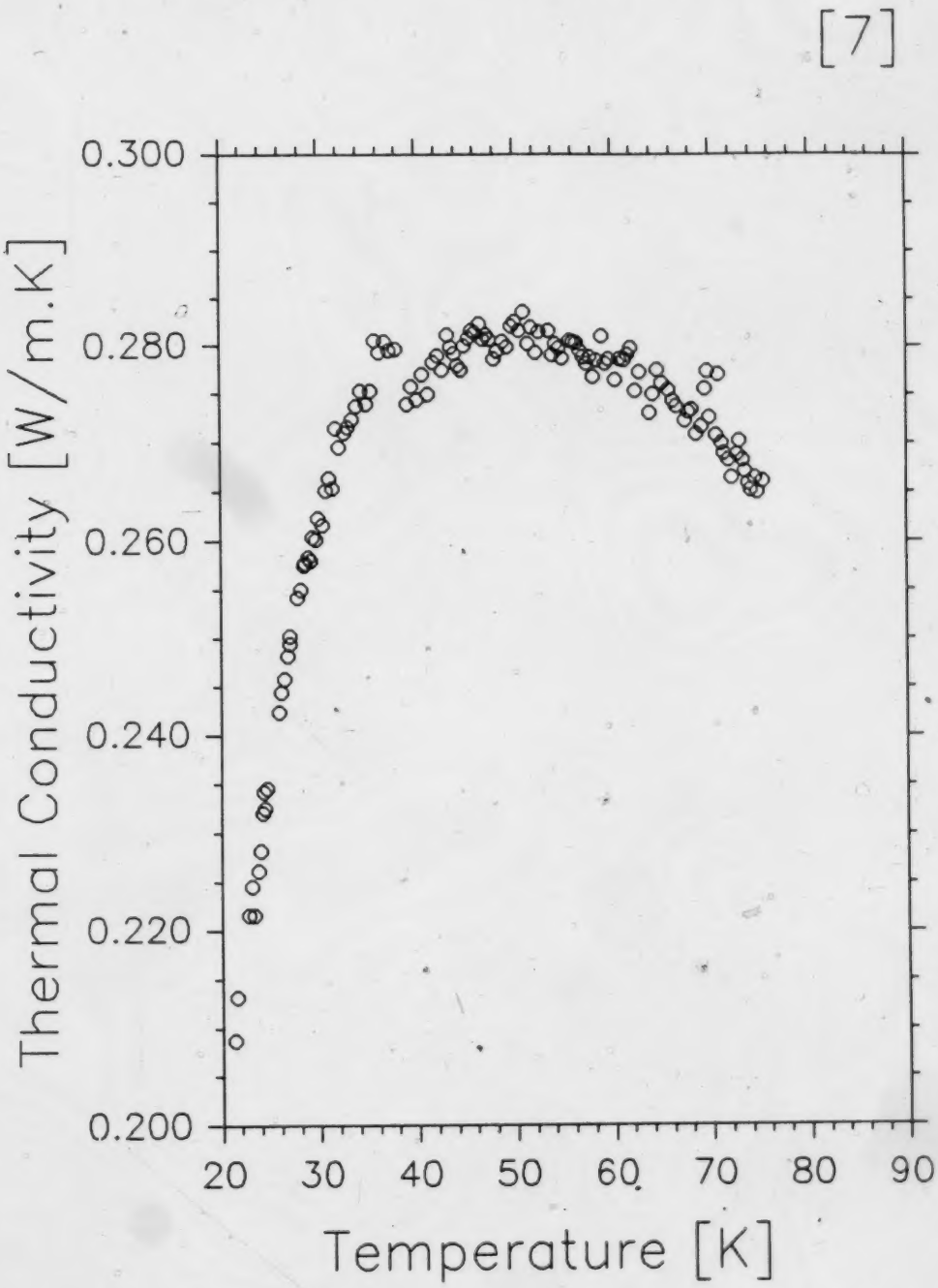

Figure C.8: Trial No. 7